

Linköping Studies in Science and Technology
Thesis No. 1104

A Specific Heat Ratio Model and Compression Ratio Estimation

Marcus Klein

Division of Vehicular Systems
Department of Electrical Engineering
Linköping University, SE-581 83 Linköping, Sweden
<http://www.vehicular.isy.liu.se/>
Email: klein@isy.liu.se

Linköping 2004

**A Specific Heat Ratio Model
and
Compression Ratio Estimation**

© 2004 Marcus Klein

*Department of Electrical Engineering,
Linköping University,
SE-581 83 Linköping,
Sweden.*

ISBN 91-7373-992-8 ISSN 0280-7971
LiU-TEK-LIC-2004:33

Printed by UniTryck, Linköping, Sweden 2004

To Sofia and Ebba

Abstract

Cylinder pressure modeling and heat release analysis are today important and standard tools for engineers and researchers, when developing and tuning new engines. An accurate specific heat ratio model is important for an accurate heat release analysis, since the specific heat ratio couples the systems energy to other thermodynamic quantities.

The objective of the first part is therefore to investigate models of the specific heat ratio for the single-zone heat release model, and find a model accurate enough to introduce a cylinder pressure modeling error less than or in the order of the cylinder pressure measurement noise, while keeping the computational complexity at a minimum. As reference, a specific heat ratio is calculated for burned and unburned gases, assuming that the unburned mixture is frozen and that the burned is at chemical equilibrium. Use of the reference model in heat release analysis is too time consuming and therefore a set of simpler models, both existing and newly developed, are compared to the reference model.

A two-zone mean temperature model and the Vibe function are used to parameterize the mass fraction burned. The mass fraction burned is used to interpolate the specific heats for the unburned and burned mixture, and then form the specific heat ratio, which renders a small enough modeling error in γ . The impact that this modeling error has on the cylinder pressure is less than that of the measurement noise, and fifteen times smaller than the model originally suggested in Gatowski et al. [1984]. The computational time is increased with 40 % compared to the original setting, but reduced by a factor 70 compared to precomputed tables from the full equilibrium program. The specific heats for the unburned mixture are captured within 0.2 % by linear functions, and the specific heats for the burned mixture are captured within 1 % by higher-order polynomials for the major operating range of a spark ignited (SI) engine.

The second part is on compression ratio estimation based on measured cylinder pressure traces. Four methods for compression ratio estimation based on both motored and fired cylinder pressure traces are described and evaluated for simulated and experimental data. The first three methods rely upon a model of polytropic compression for the cylinder pressure, and it is shown that they give a good estimate of the compression ratio for simulated cycles at low compression ratios, although the estimates are biased. The polytropic model lacks information about heat transfer and therefore, for high compression ratios, this model error causes the estimates to become more biased. The fourth method includes heat transfer, crevice effects, and a commonly used heat release model for firing cycles. This method is able to estimate the compression ratio more accurately at both low and high compression ratios. An investigation of how the methods perform when subjected to parameter deviations in crank angle phasing, cylinder pressure bias and heat transfer shows that the third and fourth method can deal with these parameter deviations.

Acknowledgments

This work has been carried out at the department of Electrical Engineering, division of Vehicular Systems at Linköpings Universitet, Sweden. It was financially funded by the Swedish Agency for Innovation Systems (VINNOVA), through the excellence center ISIS (Information Systems for Industrial control and Supervision). SAAB Automobile AB and Mecel AB are gratefully acknowledged for their support during the work.

There are a number of people I would like to express my gratitude to:

First of all I would like to thank professor Lars Nielsen for letting me join his group of excellent people, for the interesting research discussions we have had and for introducing me to the game of Texas hold'em poker. The staff at Vehicular Systems for a creative and enjoyable atmosphere.

This work would never have been accomplished without my supervisor Lars Eriksson, who has inspired me greatly through interesting discussions and through his indefatigable enthusiasm for engine research. Per Andersson and Erik Frisk for helping me out with numerous LaTeX-related questions and research problems. The members of the vehicle propulsion group, for creative discussions. Per Andersson, Anders Fröberg, Ylva Nilsson and Johan Wahlström for proof-reading earlier versions of the material, which undoubtedly improved the quality of the thesis immensely. Carolina Jansson for making administrative stuff work smoothly. Ingemar Andersson for inspiring me to finish my thesis.

To all the people who have hosted me during the last two years, among those Andrej and Maria, Dan and Tottis, Fredrik and Louise, Pontus and Emma, and especially Janne, I wish to direct my sincere gratitude for rooming me but also for making sure I had an enjoyable stay. When you come to Trollhättan, you know were to stay.

My family has always supported me, and the time during which this thesis was produced, was no exception.

Finally I would like to thank Sofia and Ebba, whom I love more than life itself, for all the joy you bring along.

Linköping, May 2004
Marcus Klein

CONTENTS

1	Introduction	1
1.1	Outline and reader's guide	3
1.2	Contributions	4
1.3	Publications	5
2	Heat-release models	7
2.1	Model basis and assumptions	9
2.2	Rassweiler-Withrow model	11
2.3	Apparent heat release model	14
2.4	Matekunas pressure ratio	15
2.5	Gatowski et al. model	16
2.6	Comparison of heat release traces	20
2.7	Summary	22
3	Heat-release model components	23
3.1	Pressure sensor model	23
3.1.1	Crank angle phasing	25
3.2	Cylinder volume model	26
3.3	Temperature models	28
3.3.1	Single-zone temperature model	28
3.4	Crevice model	30
3.5	Combustion model	32
3.5.1	Vibe function	32
3.6	Thermodynamic properties	34

3.7	Heat transfer	35
3.7.1	Engine Heat Transfer	35
3.8	Sensitivity in pressure to parameter initialization	40
3.9	Summary of single-zone heat-release models	41
4	A specific heat ratio model for single-zone heat release models	45
4.1	Introduction	46
4.1.1	Outline	46
4.2	Existing models of γ	47
4.2.1	Linear model in T	47
4.2.2	Segmented linear model in T	47
4.2.3	Polynomial model in p and T	48
4.2.4	Summary of existing γ -models	49
4.3	Chemical equilibrium	50
4.4	Unburned mixture	50
4.4.1	Modeling λ -dependence with fix slope, b	53
4.5	Burned mixture	55
4.6	Partially burned mixture	59
4.6.1	Reference model	60
4.6.2	Grouping of γ -models	61
4.6.3	Evaluation criteria	63
4.6.4	Evaluation covering one operating point	64
4.6.5	Evaluation covering all operating points	68
4.6.6	Influence of γ -models on heat release parameters	72
4.6.7	Influence of air-fuel ratio λ	73
4.6.8	Influence of residual gas	74
4.6.9	Summary for partially burned mixture	78
4.7	Conclusions	79
5	Compression ratio estimation	81
5.1	Introduction	81
5.2	The SVC engine	82
5.2.1	SVC volume function	83
5.3	Cylinder pressure modeling	83
5.3.1	Polytropic model	83
5.3.2	Standard model	84
5.4	Estimation methods	84
5.4.1	Cylinder pressure referencing	85
5.4.2	Method 1 – Sublinear approach	85
5.4.3	Method 2 – Variable projection	87
5.4.4	Method 3 – Levenberg-Marquardt	88
5.4.5	Method 4 – Levenberg-Marquardt and standard model	89
5.4.6	Summary of methods	89
5.5	Simulation results	90
5.5.1	Engine data	90

5.5.2	Method 1	92
5.5.3	Methods 2 and 3	92
5.5.4	Method 4	94
5.5.5	Summary of parameter estimations	95
5.5.6	A study of varying operating conditions	97
5.5.7	Parameter sensitivity analysis	100
5.5.8	Conclusions from simulations	100
5.6	Experimental results	102
5.6.1	Engine data	102
5.6.2	TDC-referencing	102
5.6.3	Cylinder pressure referencing	103
5.6.4	Methods 1, 2 and 3	105
5.6.5	Method 4	106
5.6.6	Summary of parameter estimations	108
5.6.7	Conclusions from experiments	109
5.7	Conclusions	110
6	Conclusions	111
	References	113
A	A specific heat ratio model – further details	119
A.1	Temperature models	119
A.1.1	Single-zone temperature model	119
A.1.2	Two-zone mean temperature model	120
A.2	Cylinder pressure model	122
A.3	Combustion model	122
A.3.1	Matekunas pressure ratio	122
A.3.2	Vibe function	123
A.4	Fuel composition sensitivity of γ	123
A.4.1	Hydrocarbons	124
A.4.2	Alcohols	124
A.4.3	Unburned mixtures	126
A.4.4	Partially burned mixture – influence on cylinder pressure	127
A.5	Altered crevice term	128
A.6	Thermodynamic properties for burned mixture	128
A.7	Thermodynamic properties for partially burned mixture	131
B	Compression ratio estimation – further details	141
B.1	Taylor expansions for sublinear approach	141
B.1.1	Compression ratio estimation	141
B.1.2	Pressure bias estimation	142
B.2	Variable Projection Algorithm	143
B.2.1	Compression ratio estimation	144
B.2.2	Pressure bias estimation	144

B.3	Levenberg-Marquardt method	144
B.3.1	Minimizing prediction errors using a local optimizer	145
B.4	SVC – Geometric data	149
B.5	Standard volume function: Effect of pin-off	149
B.6	Cylinder volume for SVC	151
B.7	Complementary figures for simulation results	152
B.8	Complementary figures for experimental results	152
C	Notation	159
C.1	Nomenclature	159
C.1.1	Heat transfer	159
C.1.2	Engine geometry	160
C.1.3	Engine cycle	160
C.1.4	Thermodynamics and combustion	161
C.1.5	Parameter estimation	162
C.1.6	Statistics	162
C.2	Abbreviations	163

INTRODUCTION

Internal combustion engines have been the primary machine for generating work in mobile applications for more than a century, they are also continuing to be of high interest due to the high energy density of the fuels and their possibility to give good total fuel consumption. Continuous improvements and refinements are made to meet the increasing performance demands from customers and legislators, where both emissions and total system economy are important.

Emission regulations from the legislators provide a hard limit on the design—they must be met. Today the state-of-the-art technology for achieving low emissions from combustion engines, is the gasoline engine equipped with a three-way catalyst (TWC). Regulations for diesel engines are also continuously being made stricter to reach those of the gasoline engine with a TWC.

Development and competition between manufacturers strives to meet the needs of customers to get products with better performance both with respect to power and fuel consumption. Emerging technologies like the gas turbine and now the fuel cell pose possibilities and give a healthy competition, which also drives the technology development of combustion engines forward.

Engineers have met the challenges posed by stricter emission regulations through for example fundamental research on combustion, adding new components to more complex systems, as well as optimization of total system performance. Engine systems are becoming increasingly complex as new technologies are developed, but systematic methods are also required to complete these technologies. Some examples of promising techniques for spark ignited (SI) engines are variable valve actuation and variable compression ratio. Both of these exemplify technologies that control the development of the in-cylinder process

directly and where it is of importance to get accurate knowledge about the combustion process. The combustion process and other in-cylinder processes are directly reflected in the measured cylinder pressure, and used as a standard tool for tuning and optimizing engine performance. This is of course also important for conventional engines.

In-cylinder pressure modeling

The in-cylinder pressure is important since it directly gives the work production in the combustion chamber and thus gives important insight into the control and tuning of the engine. To accurately model and extract information from the cylinder pressure is important for the interpretation and validity of the result. Researchers and engineers strive to extract as much information as possible from the combustion chamber through the in-cylinder pressure and models of different complexity exist for interpretation of the cylinder pressures. Here the focus is on single-zone models that treats the in-cylinder contents as a single zone and single fluid. These models can describe the cylinder pressure well and has a low computational complexity, which is also an important parameter when analyzing engine data.

Due to the short time scales of the process a sequence of measurements on an engine gives huge amounts of data. These large sets of data have to be analyzed efficiently, systematically, and with good accuracy. The focus here is on efficiency and accuracy. For the purpose of in-cylinder pressure analysis, efficient models is the same as single zone models, and the accuracy of these is the topic of the thesis. The foundation for the analysis of the model is the first law of thermodynamics where the relation between work, volume, pressure and temperature is described through the ratio of specific heats. Analyses that have been performed show that the specific heat ratio is of high importance for the model and therefore this model component is studied in great detail. Therefore, single-zone heat release models are the first topic of the thesis, where the specific heat ratio model constitutes a key part.

Compression ratio estimation

The theme in the thesis is cylinder pressure and the second topic is on compression ratio estimation based on measured cylinder pressure traces. This particular problem is directly motivated by the variable compression engine, where the compression ration can be changed continuously to eliminate an important design trade-off made in conventional engines. High compression ratios give good engine efficiency but at high loads a high compression ratio can result in engine destruction through engine knock. In that engine the compression ratio is changed continuously to get the best performance from the engine. When the engine is driven at low loads a high compression ratio is selected for good efficiency and at high loads a low compression ratio is used to reduce engine knock. Compression ratio estimation is studied for several reasons where the

most important is for diagnostic purposes. A too high compression ratio can lead to engine destruction while a too low compression ratio gives a too high fuel consumption.

Four different methods for compression ratio estimation are proposed and evaluated. The research was motivated by the variable compression engine, but the methods are generally applicable and can also be used on conventional engines to get a better value of the compression ratio from experimental data.

1.1 Outline and reader's guide

An outline of the thesis in terms of short summaries of each chapter is given and indicates the scope. The notation used is summarized in appendix C, where the parameters are given in appendix C.1 and the abbreviations are summarized in C.2.

Chapter 2: Heat-release models

This chapter serves as an introduction to single-zone heat release modeling. First the basis and assumptions made for single-zone heat release modeling are given. Based on these, four well-known heat release models are presented. These are compared with respect to their computed heat release trace given a cylinder pressure trace.

Chapter 3: Heat-release model components

The model components used in the most descriptive single-zone heat release model in chapter 2, the Gatowski et al. [1984] model, are described. The model components of the other three heat release models form a subset of these. For each model component, a method to initialize the model component parameters is given. The sensitivity in cylinder pressure for each of these parameters is then investigated. The chapter ends with a summary of the equations, parameters, inputs and outputs of the Gatowski et al. model.

Chapter 4: A specific heat ratio model for single-zone heat release models

The specific heat ratio (γ) model is an important component of a heat release model. This since the specific heat ratio couples the systems energy with the thermodynamic quantities. The objective of this chapter is therefore to find a γ -model that introduces a cylinder pressure modeling error less than or in the order of the cylinder pressure measurement noise, while keeping the computational complexity at a minimum. This is done by finding γ -models for an unburned air-fuel mixture and for a burned mixture. These models are then combined in a number of ways, to form γ -models valid for a partially burned mixture. These models are then compared to a reference model and to the model used

in Gatowski et al. [1984]. The evaluation is performed in terms of modeling error in γ and in cylinder pressure. The impact each γ -model has on the heat release, in terms of estimated heat release parameters in the Vibe function is illustrated. The influence of fuel composition, air-fuel ratio and residual gas content is also investigated. Further details and argumentation are given in appendix A.

Chapter 5: Compression ratio estimation

A newly developed engine that can alter the compression ratio continuously is used. The purpose of this chapter is to estimate the compression ratio given a cylinder pressure trace, in order to diagnose if the compression ratio gets stuck at a too high or too low ratio. Four methods for compression ratio estimation of an engine from both motored and fired cylinder pressure traces are described. These methods are evaluated for both simulated and experimental cylinder pressure data. An investigation of how the methods perform when subjected to parameter deviations in crank angle phasing, cylinder pressure bias and heat transfer is also made. Further details and argumentation for this chapter are given in appendix B.

Reader's guide

For those familiar with single-zone heat release modeling, chapter 2 and 3 can be skipped. Refer instead to section 3.9 for a summary of the Gatowski et al. [1984] model. In chapter 4 a specific heat ratio model is proposed, and the main results on this model are given in section 4.6. Chapter 5 investigates four methods for compression ratio estimation, where the main simulation results are given in section 5.5 and the main experimental results are given in section 5.6.

1.2 Contributions

The main contributions of this thesis are:

- An investigation that shows the importance of the specific heat ratio model in cylinder pressure modeling.
- A specific heat ratio model to be used primarily in single-zone heat release models. This model can easily be incorporated with the widely used heat release model described in Gatowski et al. [1984], and reduces the modeling error to be of the same order as the cylinder pressure measurement noise.
- Four methods for estimating the compression ratio index, given a cylinder pressure trace. The methods are investigated and compared in terms of accuracy, convergence speed and over-all convergence.

1.3 Publications

In the research work leading to this thesis, the author has published the following papers:

- M. Klein, L. Eriksson and Y. Nilsson [2002]. Compression estimation from simulated and measured cylinder pressure. *Electronic engine controls*, SP-1703, SAE Technical Paper 2002-01-0843. Also in SAE 2002 Transactions Journal of Engines, 111(3), September 2003.
- M. Klein and L. Eriksson [2002]. Models, methods and performance when estimating the compression ratio based on the cylinder pressure. Fourth conference on Computer Science and Systems Engineering in Linköping (CCSSE).
- M. Klein, L. Eriksson and J. Åslund [2004]. Compression ratio estimation based on cylinder pressure. In proceedings of IFAC symposium on Advances in Automotive Control, Salerno, Italy.
- M. Klein and L. Eriksson [2004]. A specific heat ratio model for single-zone heat release models. *Modeling of SI engines*, SP-1830, SAE Technical Paper 2004-01-1464.

Also published by the author, but not included in the thesis:

- M. Klein and L. Nielsen [2000]. Evaluating some Gain Scheduling Strategies in Diagnosis of a Tank System. In proceedings of IFAC symposium on Fault Detection, Supervision and Safety for Technical Processes, Budapest, Hungary.

HEAT-RELEASE MODELS

When analyzing the internal combustion engine, the in-cylinder pressure has always been an important experimental diagnostic in automotive research and development, due to its direct relation to the combustion and work producing processes [Chun and Heywood, 1987; Cheung and Heywood, 1993]. The in-cylinder pressure reflects the combustion process, the piston work produced on the gas (due to changes in cylinder volume), heat transfer to the chamber walls, as well as mass flow in and out of crevice regions between the piston, rings and cylinder liner.

Thus if an accurate knowledge of how the combustion process propagates through the combustion chamber is desired, each of these processes must be related to the cylinder pressure, so the combustion process can be distinguished. The reduction of the effects of volume change, heat transfer, and mass loss on the cylinder pressure is called *heat-release analysis* and is done within the framework of the first law of thermodynamics, when the intake and exhaust valves are closed, i.e. during the closed part of the engine cycle. The simplest approach is to regard the cylinder contents as a *single zone*, whose thermodynamic state and properties are modeled as being uniform throughout the cylinder and represented by average values. No spatial variations are considered, so the model is said to be zero-dimensional. Models for heat transfer and crevice effects can easily be included. A more accurate thermodynamic analysis would be to use a multi-zone model, where the cylinder is divided into a number of zones, differing in composition and properties. Each zone being uniform in composition and temperature, and the pressure is the same for all zones.

This chapter deals with the structure of different single-zone heat-release

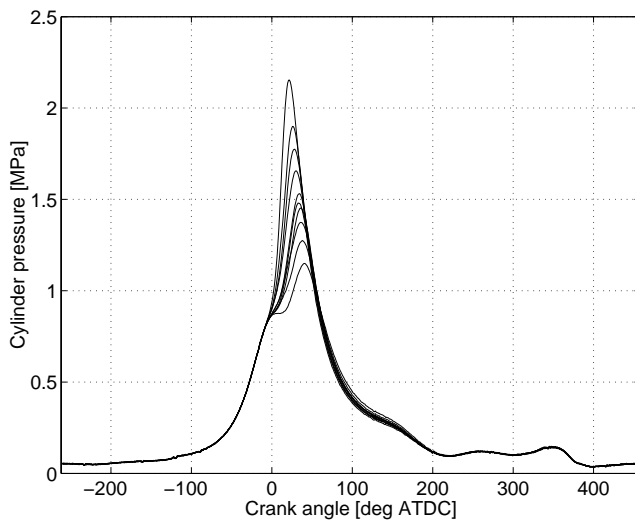


Figure 2.1: Cyclic dispersion of cylinder pressure for ten consecutive cycles.

model families and how they are derived. The subsequent chapter (chapter 3) gives a more thorough description of the model components.

Single-zone models for analyzing the heat-release rate and simulating cylinder pressure are closely connected; they share the same basic balance equation and can be interpreted as each others inverse. They both result in a first order ordinary differential equation which has to be solved. For a given heat-release model an equivalent pressure model can be derived by reordering the terms in the ordinary differential equation. Since they are so closely connected it is beneficial to discuss them together.

In spark-ignition engines the combustion process varies significantly from one engine cycle to the next one. This cycle-to-cycle variation is an important constraint on engine operation, since all cycles can not be at optimum. The variation can be quite large, as seen in figure 2.1 where the in-cylinder pressure for ten consecutive cycles is shown. Cyclic dispersion is due to varying turbulence within the cylinder from cycle to cycle, inhomogeneous air/fuel mixture and the exhaust residual gas not being fully mixed with the unburned mixture [Johansson, 1995]. If this cyclic dispersion could be eliminated, an increase in fuel economy could be achieved, since all cycles could burn at optimum rate [Stone, 1999, p.181].

Due to the cyclic dispersion there is also a need for calculating the burn rate for every individual cycle, which can be done efficiently using a single-zone heat-release model.

2.1 Model basis and assumptions

The basis for the majority of the heat-release models is the first law of thermodynamics; the energy conservation equation. For an open system, it can be stated as

$$dU = \bar{d}Q - \bar{d}W + \sum_i h_i dm_i \quad (2.1)$$

where dU is the change in internal energy of the mass in the system, $\bar{d}Q$ is the heat transported to the system, $\bar{d}W$ is the work produced by the system and $\sum_i h_i dm_i$ is the enthalpy flux across the system boundary. Possible mass flows dm_i are: 1) flows in and out of the valves; 2) direct injection of fuel into the cylinder; 3) flows in and out of crevice regions; 4) piston ring blow-by; 5) The mass flow dm_i is positive for a mass flow into the system and h_i is the mass specific enthalpy of flow i . Note that h_i is evaluated at conditions given by the zone the mass element leaves.

As mentioned earlier, single-zone models is our focus at the moment, so we will now look into those in more detail. Some commonly made assumptions for the single-zone models are

- the cylinder contents and the state is uniform throughout the entire chamber
- the combustion is modeled as a release of heat
- the heat released from the combustion occurs uniformly in the chamber
- the gas mixture is an ideal gas

Consider the combustion chamber to be an open system (single zone), with the cylinder head, cylinder wall and piston crown as boundary. Figure 2.2 shows a schematic of the combustion chamber, where the sign conventions used in pressure and heat-release models are defined. The change in heat $\bar{d}Q$ consists of the released chemical energy from the fuel $\bar{d}Q_{ch}$, which is a heat adding process, and the heat transfer to the chamber walls $\bar{d}Q_{ht}$, which is a heat removing process. So, the heat transport is represented by $Q = Q_{ch} - Q_{ht}$. Note that the heat transfer cools most of the time, but sometimes heats the air-fuel mixture. The work done by the fluid on the piston W_p is positive, therefore $\bar{d}W = \bar{d}W_p$. The first law of thermodynamics (2.1) can then be rewritten as

$$\bar{d}Q_{ch} = dU_s + \bar{d}W_p - \sum_i h_i dm_i + \bar{d}Q_{ht} \quad (2.2)$$

The piston work $\bar{d}W_p$ can also be written as $\bar{d}W_p = pdV$. For an ideal gas, the change in sensible energy dU_s is a function of mean charge temperature T only, thus:

$$U_s = m_c u(T) \quad (2.3)$$

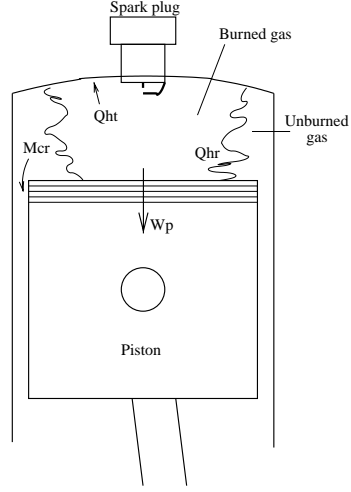


Figure 2.2: Schematic of the combustion process in the cylinder, that defines the sign convention used in the pressure and heat-release models.

which in its differentiated form becomes:

$$dU_s = m_c c_v(T) dT + u(T) dm_c \quad (2.4)$$

where m_c is the charge mass, and $c_v = \left(\frac{\partial u}{\partial T}\right)_V$ is the mass specific heat at constant volume. The mean temperature is found from the ideal gas law as $T = \frac{pV}{m_c R}$, and its differentiated form is

$$dT = \frac{1}{m_c R} (V dp + p dV - RT dm_c) \quad (2.5)$$

assuming R to be constant. For reading convenience, the dependence of T for c_p , c_v and γ is often left out in the following equations. Equation (2.2) can now be rewritten as

$$dQ_{ch} = \frac{c_v}{R} V dp + \frac{c_v + R}{R} p dV + (u - c_v T) dm_c - \sum_i h_i dm_i + dQ_{ht} \quad (2.6)$$

using equations (2.4) and (2.5). The specific heat ratio is defined as $\gamma = \frac{c_p}{c_v}$ and assuming an ideal gas the mass specific gas constant R can be written as $R = c_p - c_v$, yielding that the mass specific heat at constant volume is given by

$$c_v = \frac{R}{\gamma - 1} \quad (2.7)$$

The mass specific heat is the amount of energy that must be added or removed from the mixture to change its temperature by 1 K at a given temperature

and pressure. It relates internal energy with the thermodynamic state variables p and T , and is therefore an important part of the heat release modeling. Inserting (2.7) into (2.6) results in

$$\mathrm{d}Q_{ch} = \frac{1}{\gamma-1}V dp + \frac{\gamma}{\gamma-1}p dV + \left(u - \frac{RT}{\gamma-1}\right)dm_c - \sum_i h_i dm_i + \mathrm{d}Q_{ht} \quad (2.8)$$

From this equation, four different single-zone models with various levels of complexity will be derived. First, the polytropic model will be derived and this model forms the basis for calculating the mass fraction burned with the Rassweiler-Withrow method [Rassweiler and Withrow, 1938]. Secondly, a model for computing the apparent heat release first proposed in Krieger and Borman [1967] will be derived. Thirdly, the pressure ratio developed by Matekunas [1983] is shortly summarized. Finally, a model including heat transfer and crevice effects [Gatowski et al., 1984] will be given.

2.2 Rassweiler-Withrow model

The Rassweiler-Withrow method was originally presented in 1938 and many still use the method for determining the mass fraction burned, due to its simplicity and it being computationally efficient. The mass fraction burned $x_b(\theta) = \frac{m_b(\theta)}{m_c}$ is the burned mass $m_b(\theta)$ normalized by the total charge mass m_c , and it can be seen as a normalized version of the heat-release trace $Q_{ch}(\theta)$ such that it assumes values in the interval $[0,1]$. The relation between the mass fraction burned and the amount of heat released can be justified by noting that the energy released from a system is proportional to the mass of fuel that is burned. The input to the method is a pressure trace $p(\theta_j)$ where the crank angle θ at each sample j is known (or equivalently; the volume is known at each sample) and the output is the mass fraction burned trace $x_b(\theta_j)$.

A cornerstone for the method is the fact that pressure and volume data can be represented by the polytropic relation

$$pV^n = \text{constant} \quad (2.9)$$

where the constant exponent $n \in [1.25, 1.35]$ gives a good fit to experimental data for both compression and expansion processes in an engine [Lancaster et al., 1975]. The exponent is termed the polytropic index. It is comparable to the average value of γ_u for the unburned mixture during the compression phase, prior to combustion. But due to heat transfer to the cylinder walls, index n is greater than γ_b for the burned mixture during expansion [Heywood, 1988, p.385].

The polytropic relation in (2.9) can be found from the first law of thermodynamics (2.8) by:

- neglecting crevice effects and leakages to the crankcase (often called blow-by), i.e. $dm_c = dm_i = 0$

- taking no explicit account for heat transfer $\bar{d}Q_{ht} = 0$, thus $\bar{d}Q = \bar{d}Q_{ch} - \bar{d}Q_{ht} = \bar{d}Q_{ch}$
- assuming that the specific heat ratio is captured by the (constant) polytropic index $\gamma(T) = n$
- using that there is no release of chemical energy during the compression phase prior to the combustion or during the expansion phase after the combustion, therefore $\bar{d}Q = 0$

This yields:

$$dp = -\frac{np}{V}dV \quad (2.10)$$

from which the polytropic relation is found by integration and noting that n is considered to be constant. Note that some of the effects of heat transfer are included implicitly in the polytropic index.

When considering combustion $\bar{d}Q = \bar{d}Q_{ch} \neq 0$, equation (2.8) can be rewritten as

$$dp = \frac{n-1}{V}\bar{d}Q - \frac{np}{V}dV = dp_c + dp_v \quad (2.11)$$

where dp_c is the pressure change due to combustion, and dp_v is the pressure change due to volume change and equals dp in (2.10). In the Rassweiler-Withrow method [Rassweiler and Withrow, 1938], the actual pressure change $\Delta p = p_{j+1} - p_j$ during the interval $\Delta\theta = \theta_{j+1} - \theta_j$, is assumed to be made up of a pressure rise due to combustion Δp_c , and a pressure rise due to volume change Δp_v ,

$$\Delta p = \Delta p_c + \Delta p_v \quad (2.12)$$

which is justified by (2.11). The pressure change due to volume change during the interval $\Delta\theta$ is given by the polytropic relation (2.9), which gives

$$\Delta p_v(j) = p_{j+1,v} - p_j = p_j \left(\left(\frac{V_j}{V_{j+1}} \right)^n - 1 \right) \quad (2.13)$$

Applying $\Delta\theta = \theta_{j+1} - \theta_j$, (2.12) and (2.13) yields the pressure change due to combustion as

$$\Delta p_c(j) = p_{j+1} - p_j \left(\frac{V_j}{V_{j+1}} \right)^n \quad (2.14)$$

By assuming that the pressure rise due to combustion in the interval $\Delta\theta$ is proportional to the mass of mixture that burns, the mass fraction burned at the end of the j 'th interval thus becomes

$$x_b(j) = \frac{m_b(j)}{m_b(\text{total})} = \frac{\sum_{k=0}^j \Delta p_c(k)}{\sum_{k=0}^M \Delta p_c(k)} \quad (2.15)$$

where M is the total number of crank angle intervals and $\Delta p_c(k)$ is found from (2.14). The result from a mass fraction burned analysis is shown in fig-

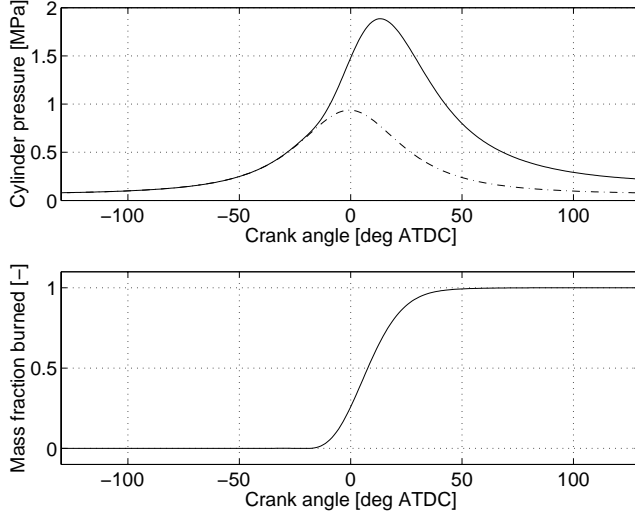


Figure 2.3: Top: Measured pressure trace (solid) and motored pressure trace (dash-dotted). Bottom: Calculated mass fraction burned profile using the Rassweiler-Withrow method.

ure 2.3, where the mass fraction burned profile is plotted together with the corresponding pressure trace. In the upper plot two measured cylinder pressures, one from a firing cycle (solid) and one from a motored cycle (dash-dotted) are displayed. When the pressure rise from the combustion becomes visible, i.e. it rises above the motored pressure, the mass fraction burned profile starts to increase above zero. The mass fraction burned profile increases monotonously as the combustion propagates throughout the combustion chamber.

If instead a heat-release trace is sought, the pressure change due to combustion in (2.11), $dp_c = \frac{n-1}{V} dQ$, can be rewritten and approximated by

$$\Delta Q(j) = \frac{V_{j+1/2}}{n-1} \Delta p_c(j) \quad (2.16)$$

where the volume V during interval j is approximated with $V_{j+1/2}$ (the volume at the center of the interval), and $\Delta p_c(j)$ is found from (2.14). The apparent heat-release trace is then found by summation. The calculated heat release is the released chemical energy from the fuel minus energy-consuming processes such as the heat transfer to the cylinder walls and crevice effects. If heat transfer and crevice effects were non-existent, the apparent heat release would correspond directly to the amount of work output from the engine, therefore the term apparent. The heat-release trace for the same data as in figure 2.3 is displayed in the upper plot of figure 2.4 as the dash-dotted line.

As mentioned earlier, there are several approximations made when using the

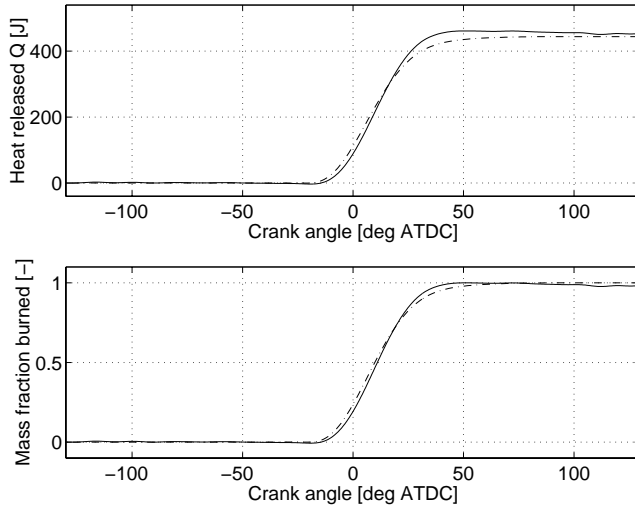


Figure 2.4: Calculated heat-release trace (upper) and mass fraction burned trace (lower), using the apparent heat release (solid) and Rassweiler-Withrow (dash-dotted) methods.

Rassweiler-Withrow method. The polytropic index n is constant. However, $\gamma(T)$ varies from compression to expansion and changes during the combustion process. It also varies with engine operating conditions.

2.3 Apparent heat release model

The first work in this direction derived from the first law of thermodynamics was proposed in Krieger and Borman [1967] and was called the computation of apparent heat release. It is also called the computation of net heat release. The method takes neither heat transfer nor crevice effects into account, thus dQ_{ht} is lumped into $dQ = dQ_{ch} - dQ_{ht}$ and $dm_c = dm_i = 0$ in (2.8). Hence, the apparent heat release dQ can be expressed as:

$$dQ = \frac{1}{\gamma(T) - 1} V dp + \frac{\gamma(T)}{\gamma(T) - 1} p dV \quad (2.17)$$

which is the same expression as (2.11) from which the Rassweiler-Withrow method is based upon, assuming that $\gamma(T) = n$. The Rassweiler-Withrow method in (2.15) is a difference equation, and this causes a quantization effect compared to the ordinary differential equation given in (2.17). The net heat-release trace and mass fraction burned profile from the Krieger and Borman model are similar to those from the Rassweiler-Withrow method, the first being

Method	θ_{10}	θ_{50}	θ_{85}	θ_b
Rassweiler-Withrow	-4.5	9.8	25.2	29.8
Apparent heat release	-6.4	11.0	26.9	33.3

Table 2.1: Crank angle positions for 10 %, 50 % and 85 % mfb as well as the rapid burn angle $\theta_b = \theta_{85} - \theta_{10}$, all given in degrees ATDC for the mass fraction burned trace in figure 2.4.

physically the more accurate one. This is shown in figure 2.4, where the upper plot shows the net heat-release traces and the lower plot shows the mass fraction burned traces, from the cylinder pressure in figure 2.3. For this particular case, the Rassweiler-Withrow method yields a higher burn rate compared to the apparent heat release method for the same data. This is reflected in the crank angle for 50 % mfb θ_{50} , which is 11.0 [deg ATDC] for the apparent heat release method and 9.8 [deg ATDC] for the Rassweiler-Withrow method. Table 2.1 summarizes the crank-angle positions for 10 %, 50 % and 85 % mfb as well as the rapid burn angle duration θ_b , and shows that the Rassweiler-Withrow method yields a shorter burn duration for this particular case. The rapid burn angle duration is defined in section 3.5 as $\theta_b = \theta_{85} - \theta_{10}$.

This is also reflected in the heat release trace, and the difference is due to the assumptions on n and $V_{j+1/2}$ in the Rassweiler-Withrow method. The mass fraction burned profile is calculated assuming that the mass of burned mixture is proportional to the amount of released chemical energy.

Pressure simulation

An ordinary differential equation for the pressure can be simulated by solving (2.17) for the pressure differential dp :

$$dp = \frac{(\gamma(T) - 1) dQ - \gamma(T) p dV}{V} \quad (2.18)$$

When performing a heat-release analysis the pressure is used as input and the heat release is given as output, and when the pressure trace is being simulated the heat-release trace is given. Therefore the cylinder pressure simulation, with the equation above, can be seen as the inverse of the heat release analysis (2.17). The only additional information that is needed for the computation is the initial value of the pressure.

2.4 Matekunas pressure ratio

The pressure ratio management was developed by Matekunas [1983] and is a computationally efficient method to determine an approximation of the mass fraction burned trace $x_b(\theta)$ at every crank angle θ . The pressure ratio is defined

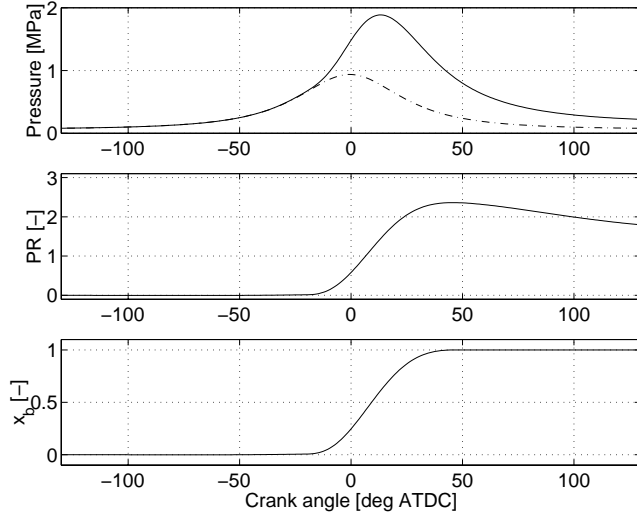


Figure 2.5: Top: Measured pressure trace (solid) and motored pressure trace (dash-dotted), same as in the upper plot of figure 2.3. Middle: Matekunas pressure ratio $PR(\theta)$ (2.19). Bottom: Computed mass fraction burned profile using (2.20).

as the ratio of the cylinder pressure from a firing cycle $p(\theta)$ and the corresponding motored cylinder pressure $p_0(\theta)$:

$$PR(\theta) = \frac{p(\theta)}{p_0(\theta)} - 1 \quad (2.19)$$

The pressure ratio (2.19) is then normalized by its maximum

$$PR_N(\theta) = \frac{PR(\theta)}{\max PR(\theta)} \quad (2.20)$$

which produces traces that are similar to the mass fraction burned profiles. The difference between them has been investigated in [Eriksson, 1999], and for position $PR_N(\theta) = 0.5$ the difference was in the order of 1-2 degrees. This suggests $PR_N(\theta)$ can be used as the mass fraction burned trace x_b . The cylinder pressure in the upper plot of figure 2.5 yields the pressure ratio PR (2.19) given in the middle plot, and an approximation of the mass fraction burned in the lower plot.

2.5 Gatowski et al. model

A more complex model is to incorporate models of heat transfer, crevice effects and thermodynamic properties of the cylinder charge into the energy conserva-

tion equation (2.8). This was first done in [Gatowski et al., 1984], where the heat-release model was developed and applied to three different engine types, among those a spark-ignited engine.

Crevice effect model

Crevices are small, narrow volumes connected to the combustion chamber. During compression some of the charge flows into the crevices, and remain there until the expansion phase, when most of the charge returns to the combustion chamber and some charge stays in the crevices. However, a small part of the charge in the crevices blows by the top ring and ends up in the crank-case, a phenomena termed blow-by. Since the flame can not propagate into the crevices, the charge residing in the crevices is not combusted. The temperature in the crevices are assumed to be close to the cylinder wall temperature, due to that the crevices are narrow [Heywood, 1988, p.387]. This has the result that during the closed phase a substantial amount of charge could be trapped in the crevices. According to Gatowski et al. [1984], the crevice volumes constitute as much as 1-2 per cent of the clearance volume in size. In section 3.4 it is shown that as much as 10 (mass) per cent of the charge could then be trapped in crevices at peak pressure.

The model in Gatowski et al. [1984] assumes all crevices can be modeled as a single aggregate constant volume V_{cr} , and that the charge in the crevice assumes the wall temperature T_w and is at the same pressure as in the combustion chamber. The ideal gas law thus gives

$$pV_{cr} = m_{cr}RT_w \implies dm_{cr} = \frac{V_{cr}}{RT_w} dp \quad (2.21)$$

where it is assumed that T_w and R are constant.

Here, we will only consider spark-ignition engines with a premixed air-fuel charge during the closed part of the engine cycle. Hence when neglecting blow-by, the only mass flow occurring is the one in and out of the crevice region. Mass balance thus yields

$$dm_c = dm_i = -dm_{cr} \quad (2.22)$$

Equation (2.8) can then be rewritten using (2.21) and (2.22) as:

$$\dot{d}Q_{ch} = \frac{1}{\gamma-1} V dp + \frac{\gamma}{\gamma-1} p dV + \left(\frac{RT}{\gamma-1} - u + h' \right) dm_{cr} + \dot{d}Q_{ht} \quad (2.23)$$

The enthalpy h' is evaluated at cylinder conditions when the mass crevice flow is out of the cylinder ($dm_{cr} > 0$), and at crevice conditions otherwise.

Heat transfer model

The heat transfer correlation model relies upon Newton's law of cooling

$$\dot{Q}_{ht} = h_c A \Delta T = h_c A (T - T_w) \quad (2.24)$$

and Woschni [1967] found a correlation between the convection heat transfer coefficient h_c and some geometric and thermodynamic properties¹,

$$h_c = \frac{0.013B^{-0.2}p^{0.8} \left(C_1 u_p + \frac{C_2(p-p_0)T_r V_s}{p_r V_r} \right)^{0.8}}{T^{0.55}} \quad (2.25)$$

Woschni's heat transfer correlation model, among others, is more fully described in section 3.7. Note that when simulating heat transfer in the crank angle domain,

$$\frac{dQ_{ht}}{d\theta} = \frac{dQ_{ht}}{dt} \frac{dt}{d\theta} = \dot{Q}_{ht} \frac{60}{2\pi N} \quad (2.26)$$

should be used, where N [rpm] is the engine speed.

Model of thermodynamic properties

The ratio of specific heats $\gamma(T)$ is modeled as a linear function of temperature.

$$\gamma_{lin}(T) = \gamma_{300} + b(T - 300) \quad (2.27)$$

In Gatowski et al. [1984] it is stated that this component is important, since it captures how the internal energy varies with temperature. This is an approximation of the thermodynamic properties but it is further stated that this approximation is consistent with the other approximations made in the model. The thermodynamic properties of both unburned and burned air-fuel charges are further investigated in section 4.2. Using $\gamma(T) = \frac{c_p(T)}{c_v(T)}$ and $R(T) = c_p(T) - c_v(T)$, together with the linear model of $\gamma(T)$ in (2.27), ends up in an expression for $c_v(T)$:

$$c_v(T) = \frac{R}{\gamma(T) - 1} = \frac{R}{\gamma_{300} + b(T - 300) - 1} \quad (2.28)$$

The only thing remaining in (2.23) to obtain a full description of the model, is an expression for $c_v T + h' - u$. Remembering that $h = RT + u$ and $c_v = \left(\frac{\partial u}{\partial T}\right)_V$,

$$\begin{aligned} c_v T + h' - u &= c_v T + RT' + u' - u \\ &= c_v T + RT' + \int_T^{T'} c_v dT \end{aligned} \quad (2.29)$$

Integrating c_v from the cylinder conditions to crevice conditions gives the amount of energy left or added to the system when a mass enters the crevice volume. The integration is performed below:

$$\begin{aligned} u' - u &= \int_T^{T'} c_v dT \\ &= \frac{R}{b} \{ \ln(\gamma_{300} + b(T' - 300) - 1) - \ln(\gamma_{300} + b(T - 300) - 1) \} \\ &= \frac{R}{b} \ln \left(\frac{\gamma'_{lin} - 1}{\gamma_{lin} - 1} \right) \end{aligned} \quad (2.30)$$

¹The value of the first coefficient differs from the one in [Woschni, 1967], since it is recalculated to fit the SI-unit system

When using a higher order polynomial $\gamma(T) = \gamma_{300} + b_1(T - 300) + \dots + b_n(T - 300)^n$, the energy term in (2.30) must be rewritten as:

$$\begin{aligned} u' - u &= \int_T^{T'} c_v dT \\ &= R \left\{ \frac{1}{b(T')} \ln(\gamma(T') - 1) - \frac{1}{b(T)} \ln(\gamma(T) - 1) \right\} \end{aligned} \quad (2.31)$$

where $b(T) = b_1 + \dots + nb_n(T - 300)^{n-1}$. Equation 2.31 is valid for $n = 1, 2, \dots$

Gross heat-release simulation

Inserting equations (2.21) to (2.30) into (2.8), yields the following expression for the released chemical energy:

$$\begin{aligned} dQ_{ch} &= \frac{1}{\gamma-1} V dp + \frac{\gamma}{\gamma-1} p dV + dQ_{ht} + (c_v T + R T' + \frac{R}{b} \ln \left(\frac{\gamma'-1}{\gamma-1} \right)) \frac{V_{cr}}{R T_w} dp \\ &= \underbrace{\frac{1}{\gamma-1} V dp + \frac{\gamma}{\gamma-1} p dV}_{dQ_{net}} + \underbrace{\left(\frac{1}{\gamma-1} T + T' + \frac{1}{b} \ln \left(\frac{\gamma'-1}{\gamma-1} \right) \right) \frac{V_{cr}}{T_w} dp}_{dQ_{crevice}} \end{aligned} \quad (2.32)$$

This ordinary differential equation can easily be solved numerically for the heat-release trace, if a cylinder pressure trace is provided, together with an initial value for the heat release. Given the cylinder pressure in figure 2.3, the heat-release trace given in figure 2.6 is calculated. The solid line is the gross heat released, i.e. the chemical energy released during the engine cycle. The dash-dotted line shows heat released if not considering the crevice effect, and the dashed line shows the net heat release, i.e. when not considering neither heat transfer nor crevice effects. For this particular case, the heat transfer is about 70 J and the crevice effect is about 30 J, i.e. approximately 14 and 6 per cent of the total released energy respectively.

Cylinder pressure simulation

Reordering (2.32), gives an expression for the pressure differential as

$$dp = \frac{dQ_{ch} - \frac{\gamma}{\gamma-1} p dV - dQ_{ht}}{\frac{1}{\gamma-1} V + \frac{V_{cr}}{T_w} \left(\frac{T}{\gamma-1} - \frac{1}{b} \ln \left(\frac{\gamma-1}{\gamma'-1} \right) + T' \right)} \quad (2.33)$$

This ordinary differential equation can easily be solved numerically for the cylinder pressure, if a heat-release trace dQ_{ch} is provided, together with an initial value for the cylinder pressure. For this purpose the well-known Vibe function in its differentiated form is used, and it is introduced in section 3.5.

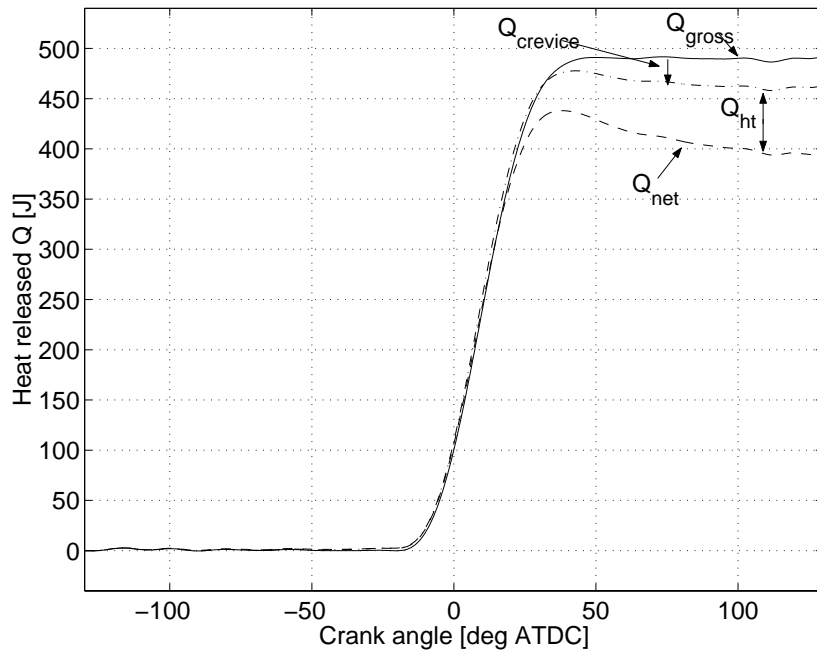


Figure 2.6: Heat-release trace from the Gatowski model given the cylinder pressure in figure 2.3.

2.6 Comparison of heat release traces

The single zone heat release models presented in the previous sections all yield different heat release traces for a given cylinder pressure trace. This is shown in figure 2.7, where the heat release traces for the Rassweiler-Withrow, apparent heat release and Gatowski models are displayed in the upper plot. As expected, the accumulated heat release is higher for the Gatowski model since it accounts for heat transfer and crevice effects. The mass fraction burned traces do not differ as much, as displayed in the lower plot of figure 2.7. For this operating point, the Rassweiler-Withrow model produces a mass fraction burned trace more like the one found by the Gatowski model, as shown by comparing the burn angles given in table 2.2. Note that the heat release traces from the Rassweiler-Withrow, apparent heat release and Matekunas models are set constant when they have reached their maximum values. If not, their behavior would be similar to the net heat release trace Q_{net} given in figure 2.6.

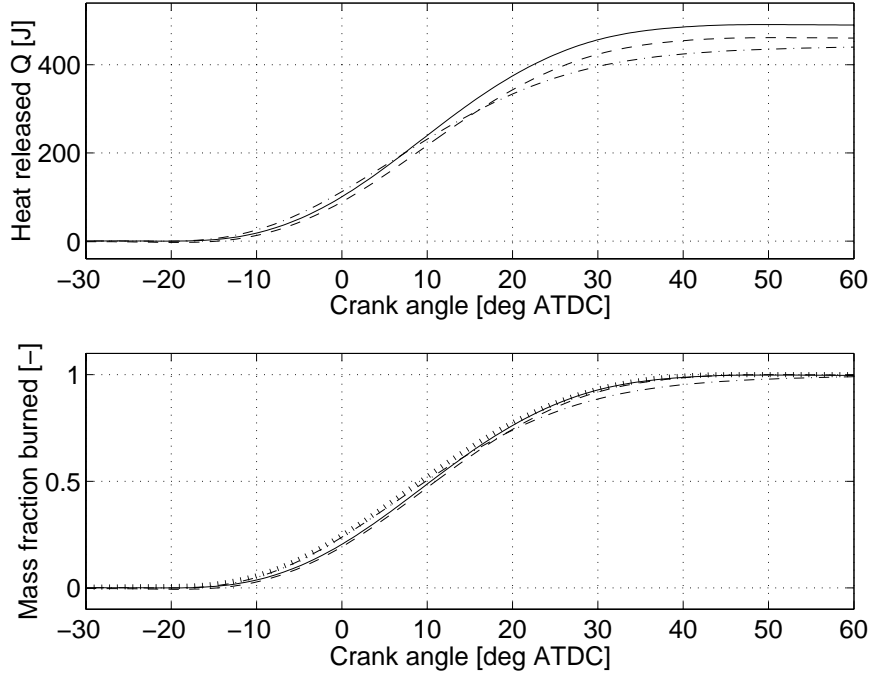


Figure 2.7: *Upper*: Heat-release trace from the Gatowski (solid), apparent heat release (dashed) and Rassweiler-Withrow (dash-dotted) models given the cylinder pressure in figure 2.3. *Lower*: Mass fraction burned traces corresponding to the upper plot and from Matekunas pressure ratio (dotted).

Method	θ_{10}	θ_{50}	θ_{85}	θ_b
Rassweiler-Withrow	-4.5	9.8	25.2	29.8
Apparent heat release	-6.4	11.0	26.9	33.3
Matekunas	-6.9	9.2	24.0	30.9
Gatowski et.al.	-5.1	10.4	24.4	29.5

Table 2.2: Crank angle positions for 10 %, 50 % and 85 % mfb as well as the rapid burn angle $\theta_b = \theta_{85} - \theta_{10}$, all given in degrees ATDC for the mass fraction burned traces in the lower plot of figure 2.7.

2.7 Summary

A family of single-zone heat release models have been derived starting from the first law of thermodynamics, the energy conservation equation. The three models described are then compared and their specific model assumptions are pointed out. The most elaborate one is the Gatowski et al. model, which includes heat transfer described by Woschni's heat transfer correlation and crevice effects. This model also assumes that the specific heat ratio for the cylinder charge can be described by a linear function in temperature. The other three models, the Rassweiler-Withrow model, the Matekunas pressure ratio and the apparent heat release model, are all more computationally efficient than the Gatowski et al. model, merely since they lack the modeling of heat transfer and crevice effect, as well as having a constant specific heat ratio. This computational efficiency of course comes to a cost of less descriptive models. Therefore, the Gatowski et al. model will be the model used for the parameter estimations and the Rassweiler-Withrow model will only serve as an initialization. The model components in the Gatowski et al. model will now be more thoroughly described in chapter 3.

HEAT-RELEASE MODEL COMPONENTS

No model is better than its components, therefore models for the various components given in chapter 2 and especially in section 2.5 for the Gatowski et al.-model, are treated more fully here in a separate chapter. Some of the model components have already been introduced in section 2.5, but all components will be more thoroughly explained and compared to other model components in sections 3.1-3.7. In section 3.8 the cylinder pressure sensitivity to the parameter initializations is briefly investigated. The equations that form the complete Gatowski et al. single-zone heat release model are boxed, and the model is summarized in section 3.9.

3.1 Pressure sensor model

The in-cylinder pressure is measured using a water-cooled quartz pressure transducer, a piezoelectric sensor that becomes electrically charged when there is a change in the forces acting upon it. Piezoelectric transducers react to pressure changes by producing a charge proportional to the pressure change. This charge is then integrated by the charge amplifier, and results in a relative pressure given in volts. The charge amplifier also drifts due to current leakage. It is however assumed that this drift is slow, and then a static model of the pressure sensor can be used:

$$\boxed{p_m = K_p p + \Delta p} \quad (3.1)$$

where p_m is the measured cylinder pressure and p is the true cylinder pressure. The gain K_p is considered as constant for the measurement setup, but the

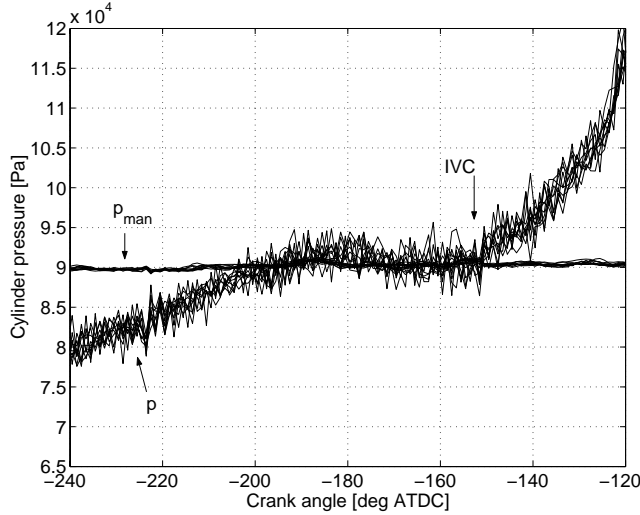


Figure 3.1: Ram effect in the intake runners clearly visible between -200 [deg ATDC] and IVC.

offset Δp changes during the cycle due to leakage in the charge amplifier and thermal shock of the sensor. Due to the assumption of a slow drift in the charge amplifier, the pressure offset Δp is considered to be constant for one cycle.

Parameter initialization – pressure offset Δp

The determination of the pressure offset is referred to as pegging the pressure signal, or cylinder pressure referencing. The pressure offset can be estimated with various methods [Randolph, 1990; Brunt and Pond, 1997]. It is generally recommended that pegging is performed once for every pressure cycle. One method is to find Δp in a least squares sense using a polytropic model for the cylinder pressure p .

Another method is to reference the measured cylinder pressure $p_m(\theta)$ to the intake manifold pressure p_{man} before inlet valve closing (IVC), for several samples of p_{man} . This method is often referred to as intake manifold pressure referencing (IMPR) [Brunt and Pond, 1997]. Due to standing waves (ram effect) in the intake runners at certain operating points, see figure 3.1, the referencing might prove to be insufficient. The referencing should be done at crank angles where the change in cylinder pressure is approximately flat for all operating points, i.e. where the intake manifold pressure p_{man} and the measured cylinder pressure p_m are the same or have a constant difference [Brunt and Pond, 1997]. Figure 3.2 shows the cylinder pressure change for $\theta \in [-200, -160]$ [deg ATDC] for a number of operating points. Using the same approach as

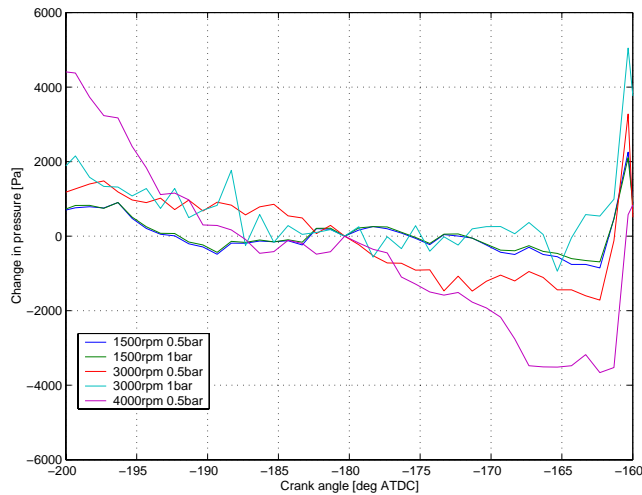


Figure 3.2: Pressure offset as function of CAD when referencing to intake manifold pressure. The pressure change is approximately flat for all operating points between -167 and -162 CAD.

in Brunt and Pond [1997], the referencing should be done between -167 to -162 CAD.

If IMPR proves to be insufficient, Δp must be estimated from the measured cylinder pressure data to achieve a correct referencing, but referencing to p_{man} serves well as an initialization.

Parameter initialization – pressure gain K_p

The gain K_p can be determined in at least three different ways, summarized in Johansson [1995]: The first is to determine the gain for each component in the measurement chain and multiply them to get K_p ; The second is to calibrate the total chain by applying a well defined pressure step and measure the result; The third way being to determine the total gain in conjunction with a thermodynamic model. Here the first method is used, and the gain K_p is determined by using tabulated values from the manufacturer.

3.1.1 Crank angle phasing

The pressure trace is sampled at certain events, such as every crank angle degree. Since the mounting can not be performed with infinite precision, an uncertainty in the exact crank angle position for the sampling pulses is inherent. So, when calculating the heat-release trace (2.32), the phasing of the pressure trace relative to the volume trace will most definitively affect the outcome.

According to Amann [1985]; Morishita and Kushiyama [1997]; Staś [2000], this phasing need to be accurate within 0.1 CAD, in order to accurately calculate the work (imep) from a specific cylinder. According to Brunt and Emtage [1997] the phasing need to be within 0.2 CAD to find imep accurate within 1 %, since typically a 1 CAD phase shift induce a 4 % imep error with gasoline engines and the relationship between imep error and crank angle error is linear [Brunt and Emtage, 1996].

In Schagerberg and McKelvey [2003], models for crank angle offset θ_0 in a multi-cylinder engine are developed. The crank angle offset depends on the cylinder number and the phase of the cycle, i.e. θ_0 differs during compression, combustion and expansion. This is due to crank-shaft torsion and flexibility, which can be as large as 1 CAD [Stone, 1999].

Here a rigid crank shaft is considered and therefore these effects are neglected. Neglecting these effects, and assuming that the sampled value at crank angle θ_i can be modeled as having a constant offset θ_0 from the true crank angle $\theta_{i,\text{true}}$, ends up in

$$\boxed{\theta_i + \theta_0 = \theta_{i,\text{true}}} \quad (3.2)$$

Parameter initialization – crank angle offset θ_0

The determination of θ_0 is often referred to as *TDC determination*. θ_0 is one of the parameters to be identified from the thermodynamic model of the cylinder pressure, and an initial value of θ_0 is provided from a motoring cycle.

Other methods of finding the crank angle offset θ_0

The easiest way to find θ_0 is of course to consider only motored cycles, i.e. when there is no combustion. Then the cylinder pressure would have its maximum at TDC if it were not for heat transfer and crevice effects. Instead, the peak for the compression pressure occurs before TDC. This difference is referred to as “thermodynamic loss angle” [Hohenberg, 1979]. Attempts to avoid the problem connected with unknown heat transfer have been taken in Staś [1996]; Morishita and Kushiyama [1997]; Nilsson and Eriksson [2004], by using the polytropic relation to determine the position of TDC.

3.2 Cylinder volume model

The cylinder volume $V(\theta, x_{off})$ consists of a clearance volume $V_c(x_{off})$ and an instantaneous displacement volume $V_{id}(\theta, x_{off})$, as

$$\boxed{V(\theta, x_{off}) = V_c(x_{off}) + V_{id}(\theta, x_{off})} \quad (3.3)$$

The instantaneous displaced volume V_{id} depends on the crank angle θ , cylinder bore B , crank radius a , connecting rod length l , pin-off x_{off} and is given by

$$V_{id}(\theta, x_{off}) = \frac{\pi B^2}{4} (\sqrt{(l+a)^2 - x_{off}^2} - a \cos \theta - \sqrt{l^2 - (x_{off} + a \sin \theta)^2}) \quad (3.4)$$

for $x_{off} \in [-(l-a), (l-a)]$. The pin-off is defined as positive in the direction of the crank angle revolution. Note that for an engine with pin-off, the crank positions for BDC and TDC are affected. They are given by:

$$\theta_{TDC} = -\arcsin \frac{x_{off}}{l+a} \quad (3.5a)$$

$$\theta_{BDC} = -\arcsin \left(\frac{x_{off}}{l-a} \right) + \pi \quad (3.5b)$$

and are not symmetric, as would be the case without pin-off. The pin-off also affects the piston stroke S , and therefore the displacement volume since $V_d = \frac{\pi B^2}{4} S$. The piston stroke is given by

$$S = \sqrt{(l+a)^2 - x_{off}^2} - \sqrt{(l-a)^2 - x_{off}^2} \geq 2a \quad (3.6)$$

and this yields a greater displacement volume than in the case of no pin-off ($S = 2a$). The impact of pin-off on the cylinder volume is more closely investigated in appendix B.5. It is found for the SVC engine that the relative error in instantaneous cylinder volume can be as large as 1.6 %. By interpreting the difference in crank angle position of TDC due to pin-off as a constant crank angle offset θ_0 , as in (3.2), the relative error in $V(\theta, x_{off})$ is reduced to less than 0.3 %. Not accounting for pin-off therefore contributes to the problem of TDC determination. So, if the engine's pin-off is unknown, the discrepancy in computing the cylinder volume $V(\theta, 0)$ (3.3) can almost fully be captured by the crank angle offset model (3.2). If the pin-off x_{off} is known, there is no reason for not including it in $V(\theta, x_{off})$ (3.3), since it increases the accuracy of $V(\theta, x_{off})$ at almost no additional computational cost.

The cylinder volume is further disrupted when the mono-head can be tilted, as in the case of the SVC engine. This is further described in appendix B.6, where the tilting is interpreted as an additional pin-off.

The compression ratio index r_c of a cylinder is defined as the ratio between the maximum and minimum cylinder volume:

$$r_c = \frac{V_d + V_c}{V_c} = 1 + \frac{V_d}{V_c} \quad (3.7)$$

Parameter initialization – clearance volume V_c

The clearance volume V_c strongly influences the maximum cycle temperature and pressure through the compression ratio index, and for heat release and pressure simulations it is therefore of great importance. Due to geometric uncertainties in manufacturing, a spread of the actual clearance volume from engine

to engine and cylinder to cylinder is inherent [Amann, 1985]. The compression ratio index given from the manufacturer serves well as an initialization. It can also be initialized by using a polytropic relation, an initialization that works better the lower the real compression ratio index is [Klein et al., 2002]. This since the polytropic relation does not take heat transfer and crevice effects into account explicitly.

When simulating either the heat release (2.32) or the cylinder pressure (2.33), knowing the differential volume $\frac{dV(\theta)}{d\theta}$ is necessary and it is given by

$$\boxed{\frac{dV(\theta)}{d\theta} = \frac{\pi B^2 a}{4} \left(\sin \theta + \frac{(x_{off} + a \sin \theta) \cos \theta}{\sqrt{l^2 - (x_{off} + a \sin \theta)^2}} \right)} \quad (3.8)$$

When computing the heat transfer rate (3.24), the instantaneous combustion chamber surface area $A(\theta)$ through which the heat transfer occurs is computed as

$$A(\theta) = A_{ch} + A_{pc} + A_{lat}(\theta) \quad (3.9)$$

where A_{ch} is the cylinder head surface area and A_{pc} is the piston crown surface area. For flat-topped pistons, $A_{pc} = \frac{\pi B^2}{4}$. The lateral surface area $A_{lat}(\theta)$ is approximated by the lateral surface of a cylinder, and A_{ch} is assumed to be equal to A_{pc} . The instantaneous combustion chamber surface area can then be expressed as

$$\boxed{A(\theta) = \frac{\pi B^2}{2} + \pi B \left(\sqrt{(l+a)^2 - x_{off}^2} - a \cos \theta - \sqrt{l^2 - (x_{off} + a \sin \theta)^2} \right)} \quad (3.10)$$

3.3 Temperature models

Two models for the in-cylinder temperature will be described, the first is the mean charge single-zone temperature model and is the one used in the Gatowski et al.-model. The second is a two-zone mean temperature model, used to compute the single-zone thermodynamic properties as mean values of the properties in a two-zone model, an approach will be introduced in section 4.2.

3.3.1 Single-zone temperature model

The mean charge temperature T for the single-zone model is found from the state equation $pV = m_c RT$, assuming the total mass of charge m_c and the mass specific gas constant R to be constant. These assumptions are reasonable since the molecular weights of the reactants and the products are essentially the same [Gatowski et al., 1984]. If all thermodynamic states $(p_{ref}, T_{ref}, V_{ref})$ are known/evaluated at a given reference condition r , such as IVC, the mean

charge temperature T is computed as

$$T = \frac{T_{IVC}}{p_{IVC}V_{IVC}}pV \quad (3.11)$$

The cylinder volume at IVC is computed using the cylinder volume given in (3.4) for θ_{IVC} and is therefore considered to be known. The two other states at IVC (p_{IVC}, T_{IVC}) are considered unknown and have to be estimated.

Parameter initialization – mean charge temperature at IVC T_{IVC}

The mean charge temperature at IVC differs from the gas temperature in the intake manifold T_{man} . The charge is heated due to both mixing with residual gases which are approximately at 1400 K [Heywood, 1988, p.178], and to in-cylinder heat transfer from piston, valves and cylinder walls. On the other hand, fuel evaporation can cool the charge by as much as 25 K according to [Stone, 1999]. Altogether these effects make T_{IVC} become larger than T_{man} .

An approximative model for finding the residual gas fraction $x_r = \frac{m_r}{m_c}$ and temperature T_r cited in Heywood [1988, p.178] is used to find T_{IVC} . The residual gas mass is given by m_r and the total cylinder gas mass by m_c . The residual gas is left behind from the exhaust process and fills the clearance volume V_c at pressure p_{exh} and temperature T_6 , where p_{exh} is the exhaust manifold pressure and T_6 is the mean charge temperature at $\theta = 360$ CAD, i.e. at the end of the exhaust stroke. The intake manifold contains a fresh air-fuel charge at pressure p_{man} and temperature T_{man} . As the intake valve opens, the residual gases expand isentropically to volume V_r and temperature T_r according to

$$V_r = V_c \frac{p_{exh}}{p_{man}} \quad (3.12a)$$

$$T_r = T_6 \left(\frac{p_{man}}{p_{exh}} \right)^{\frac{\gamma}{\gamma-1}} \quad (3.12b)$$

The rest of the cylinder volume V_{af} is filled with fresh air-fuel charge, i.e. $V_{af} = V - V_r$. The ideal gas law is then used to compute the residual gas fraction x_r as:

$$\begin{aligned} x_r &= \frac{m_r}{m_{af} + m_r} = \frac{\frac{p_{man}V_r}{RT_r}}{\frac{p_{man}V_{af}}{RT_{man}} + \frac{p_{man}V_r}{RT_r}} = \dots \\ &= \left(1 + \frac{T_r}{T_{man}} \left(r_c \frac{p_{man}}{p_{exh}} - \left(\frac{p_{man}}{p_{exh}} \right)^{(\gamma-1)/\gamma} \right) \right)^{-1} \end{aligned} \quad (3.13)$$

and the mean charge temperature at IVC is then computed as:

$$T_{IVC} = T_r r_c x_r \left(\frac{p_{man}}{p_{exh}} \right) \quad (3.14)$$

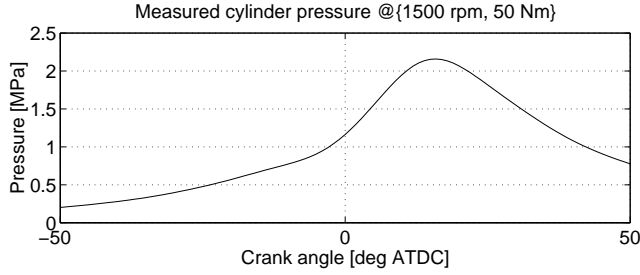


Figure 3.3: Experimental cylinder pressure.

where $T_r = 1400$ K and $(\gamma - 1)/\gamma = 0.24$ are appropriate average values to use for initial estimates [Heywood, 1988, p.178]. This model does not take valve overlap into account. For the cylinder pressure given in figure 3.3, the residual gas mass fraction was found to be $x_r = 5.7\%$ and the mean charge temperature at IVC $T_{IVC} = 346$ K.

Another approach of calculating the residual gas fraction was introduced in Fox et al. [1993]. The approach relies upon intake and exhaust manifold pressures only, and therefore the influence of combustion can not be accounted for. In Mladek and Onder [2000] the use of the cylinder pressure is included, and there the combustion event is also accounted for. None of these approaches will however be used here.

Parameter initialization – cylinder pressure at IVC p_{IVC}

The parameter p_{IVC} is initialized by the measured cylinder pressure p_m in conjunction with the pressure sensor offset Δp and gain K_p , and the crank angle offset θ_0 by using equations (3.1) and (3.2).

3.4 Crevice model

In an engine, gases flow in and out of the crevices connected to the combustion chamber as the cylinder pressure raises and falls. Crevices include those between piston, rings and liner, any head gasket gap, spark plug threads and space around the the pressure transducer. During compression some of the charge flows into the crevices, and remain there until the expansion phase, when most of the charge returns to the combustion chamber. The part of the charge that does not return to the cylinder, ends up in the crank-case and is termed blow-by. The flame can not propagate into the crevices, and therefore some of the charge is not combusted.

When modeling the crevice effect, the temperature in the crevices are assumed to be close to the cylinder wall temperature, so during the closed phase

a substantial amount of charge could be trapped in the crevices. According to Gatowski et al. [1984], the crevice volumes can constitute as much as 1-2 per cent of the clearance volume in size. Consider the ratio of charge mass to the mass in the crevices:

$$\frac{m_{cr}}{m_c} = \frac{V_{cr}}{V} \frac{T}{T_{cr}} \quad (3.15)$$

Due to the temperature difference in the cylinder and in the crevices which at the end of combustion approaches a factor 4-5, as much as 10 (mass) per cent of the charge could then be trapped in crevices at peak pressure.

The model developed and applied in Gatowski et al. [1984] assumes that all crevices can be modeled as a single aggregate constant volume V_{cr} , and that the charge in the crevice assumes the average wall temperature T_w and is at the same pressure as in the combustion chamber. The ideal gas law thus gives

$$pV_{cr} = m_{cr}RT_w \implies dm_{cr} = \frac{V_{cr}}{RT_w} dp \quad (3.16)$$

where it is assumed that T_w and R are constant. Gatowski et al. [1984] points out that this model is not meant to account for each crevice, but rather to account for the overall crevice effect.

Parameter initialization – crevice volume V_{cr}

The single aggregate crevice volume V_{cr} is unknown and is therefore set to 1 per cent of the clearance volume V_c , which is a reasonable value according to Gatowski et al. [1984]. For an engine with varying clearance volume, such as the SVC engine, this would yield a crevice volume dependent of the compression ratio index. To avoid this, V_{cr} is set to 1% V_c at $r_c = 11$, i.e. the clearance volume in the mid range of the compression ratio index is used.

Parameter initialization – cylinder mean wall temperature T_w

The cylinder wall temperature T_w is not only used in the crevice model, but also in the heat transfer model described in section 3.7. It varies during the engine cycle due to heat transfer in the cylinder block, but here a area-weighted mean value of the temperatures of the exposed cylinder walls, the head and the piston crown for the closed part of the engine cycle is used. Here T_{wall} is initialized to a constant value of 440 K [Eriksson, 1998; Brunt and Emtage, 1997], set only by it being a reasonable value. One method of finding the mean wall temperature is developed in Arsie et al. [1999]. It uses that at the beginning of the compression stroke the mean charge temperature is lower than the mean cylinder wall temperature, i.e. the heat flux is from the chamber walls to the charge. As the compression proceeds, the charge temperature will increase due to the piston work, and the heat flux will eventually become inverted. This is valid for all driving conditions except early stages of cold start, where instead the heat flux is from charge to the cold cylinder walls during the whole cycle.

The method finds the polytropic index $n(\theta)$ in (2.9) at every sample during an adiabatic compression and it is compared to the specific heat ratio $\gamma(\theta)$. When these coincide, i.e. $n(\theta') = \gamma(\theta')$, there is no net heat flux between the charge and the cylinder wall, and therefore the mean charge temperature T equals the cylinder mean wall temperature T_w at θ' . The method assumes that T_{ivc} , Δp and θ_0 are known, and works well in the absence of noise, and is therefore suitable to use for simulations.

3.5 Combustion model

The combustion of fuel and air is a very complex process, and would require extensive modeling to be fully captured. Our approach here is to use a parameterization of the burn rate of the combusted charge. The prevailing combustion model is the Vibe function [Vibe, 1970], which sometimes is spelled Wiebe function.

3.5.1 Vibe function

The Vibe function is often used as a parameterization of the mass fraction burned x_b , and it has the following form

$$x_b(\theta) = 1 - e^{-a\left(\frac{\theta - \theta_{ig}}{\Delta\theta}\right)^{m+1}} \quad (3.17)$$

and the burn rate is given by its differentiated form

$$\boxed{\frac{dx_b(\theta)}{d\theta} = \frac{a(m+1)}{\Delta\theta} \left(\frac{\theta - \theta_{ig}}{\Delta\theta}\right)^m e^{-a\left(\frac{\theta - \theta_{ig}}{\Delta\theta}\right)^{m+1}}} \quad (3.18)$$

where θ_{ig} is the start of the combustion, $\Delta\theta$ is the total combustion duration, and a and m are adjustable parameters. The Vibe function is over-parameterized in a , m , and $\Delta\theta$, since for example the sets [$a = 1$, $\Delta\theta = 1$, $m = 1$] and [$a = 4$, $\Delta\theta = 2$, $m = 1$] give identical function values. To parameterize the mass fraction burned (mfb) trace with physical parameters, two burn rate angles are often used, namely the flame-development angle θ_d which corresponds to the crank angle from 0 % mfb (ignition) to 10 % mfb, and the rapid burn angle θ_b (10-85 % mfb) [Heywood, 1988; Eriksson, 1999], illustrated in figure 3.4. The burn angle parameters have a direct relation to the parameters in the Vibe function, but due to the over-parameterization in a and $\Delta\theta$, one of them must be specified before-hand to get a unique solution. If $\Delta\theta$ is specified, the Vibe parameters become:

$$\boxed{m = \frac{\ln(\ln(1 - 0.1) - \ln(1 - 0.85))}{\ln\theta_d - \ln(\theta_d + \theta_b)} - 1} \quad (3.19a)$$

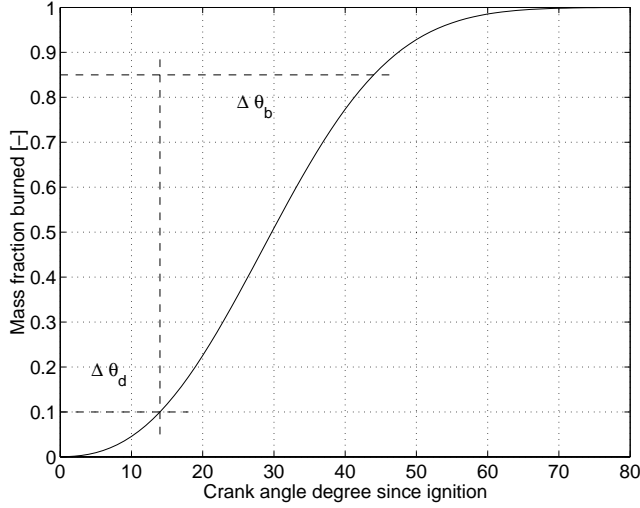


Figure 3.4: Mass fraction burned profile with the flame development angle θ_d and rapid burn angle θ_b marked.

$$a = -\left(\frac{\Delta\theta}{\theta_d}\right)^{m+1} \ln(1 - 0.1) \quad (3.19b)$$

The differentiated Vibe function (3.18) is used to produce a mass fraction burned trace, i.e. a normalized heat-release trace. The absolute value of the heat-release rate $\frac{dQ_{ch}}{d\theta}$ is given by the fuel mass m_f , the specific heating value of the fuel q_{HV} , and combustion efficiency η_f as

$$\frac{dQ_{ch}}{d\theta} = m_f q_{HV} \eta_f \frac{dx_b}{d\theta} = Q_{in} \frac{dx_b}{d\theta} \quad (3.20)$$

where Q_{in} represents the total energy released from combustion.

Summing up, the combustion process is described by (3.20) and parameterized by Q_{in} , θ_{ig} , θ_d , and θ_b .

Parameter initialization – total energy released Q_{in}

The total energy released Q_{in} is influenced by a lot of parameters, such as residual gas fraction, combustion efficiency, mass of fuel, fuel heating value, but also the mass fraction burned rate due to the dependence of thermodynamic properties for the mixture of temperature and pressure. One approach to find

a reasonable initial value of Q_{in} is to rewrite m_f in (3.20) as

$$m_f = \frac{m_{af}}{1 + \lambda(\frac{A}{F})_s} = \frac{(1 - x_r)m_c}{1 + \lambda(\frac{A}{F})_s} \quad (3.21)$$

where the total charge mass m_c is found using the ideal gas law at a reference point during the high-pressure phase, e.g. IVC, yielding $m_c = \frac{p_{IVC}V_{IVC}}{RT_{IVC}}$. The fuel is assumed to be iso-octane, that has $R = 290 \frac{J}{kgK}$ (at 300 K), lower heating value $q_{HV} = 44.0 \frac{MJ}{kg}$, and stoichiometric air-fuel equivalence ratio $(\frac{A}{F})_s = 14.6$ [Heywood, 1988, p.915]. The residual gas fraction was found earlier in (3.13). So Q_{in} is initialized as

$$Q_{in} = m_f \eta_f q_{HV} = \frac{(1 - x_r)}{1 + \lambda(\frac{A}{F})_s} \frac{p_{IVC}V_{IVC}}{RT_{IVC}} \eta_f q_{HV} \quad (3.22)$$

where the combustion efficiency η_f is assumed to be one.

Parameter initialization – angle-related parameters $\{\theta_{ig}, \theta_d, \theta_b\}$

The angle-related parameters $\{\theta_{ig}, \theta_d, \theta_b\}$ are initialized by the mass fraction burned trace found from the Rassweiler-Withrow method mentioned in section 2.2. Nominal values are [Eriksson, 1999]:

$\theta_{ig} \in$	$\theta_d \in$	$\theta_b \in$
[-30 , 0] [deg ATDC]	[15, 40] [deg]	[10, 50] [deg]

Other heat-release regressors

In van Nieuwstadt et al. [2000] a number of heat-release regressors are applied to a gasoline direct injected (GDI) engine, which typically has four different operating modes. One of these modes has homogenous stoichiometric mixing, and this mode is therefore comparable to the operating mode of the SI engine. It is found that the classical Vibe function with its four free parameters provides a good approximation of the heat-release trace, and that the proposed regressor in [van Nieuwstadt et al., 2000] (called SEQ) with its six free parameters, does not improve the accuracy immensely for one operating point. Therefore, the Vibe function will be used here. However, when dealing with a larger operating range of the engine, the SEQ function proved to yield parameters that were easier to regress with respect to engine operating conditions.

3.6 Thermodynamic properties

The accuracy with which the energy balance can be calculated for a combustion chamber depends in part on how accurately changes in the internal energy of the cylinder charge are represented. The most important thermodynamic property used in calculating the heat release rates for engines is the

ratio of specific heats, $\gamma = \frac{c_p}{c_v}$ [Gatowski et al., 1984; Chun and Heywood, 1987; Guezennec and Hamama, 1999].

In the Gatowski et al.-model, the specific heats ratio $\gamma(T)$ is modeled as a linear function of temperature.

$$\boxed{\gamma_{lin}(T) = \gamma_{300} + b(T - 300)} \quad (3.23)$$

Gatowski et al. [1984] states that this component is important, since it captures how the internal energy varies with temperature. This is an approximation of the thermodynamic properties but it is further stated that this approximation is consistent with the other approximations made in the model. It will be shown in chapter 4 that the linear model of γ in temperature T introduces a modeling error in cylinder pressure which is 15 times the cylinder pressure measurement noise in mean. A model of γ that introduces an error in the same order as the noise is also given.

3.7 Heat transfer

When transfer of energy is due only to a temperature difference, i.e. no work is done on the substance, this is referred to as heat transfer. There are three different types of heat transfer, namely heat transfer through *conduction*, *convection* and *radiation* [Schmidt et al., 1993].

Conduction is the transfer of energy through a substance, a solid or a fluid due to a temperature gradient in the substance.

Convection is the transfer of energy between a fluid and a solid surface.

Radiation is the transfer of energy by electro-magnetic waves.

3.7.1 Engine Heat Transfer

Typically 20-35 % of the fuel energy is passed on by heat transfer to the engine coolant, the upper limit is reached for low load conditions [Stone, 1999, p.429]. Of the total heat transfer, about half comes from in-cylinder heat transfer and the rest from heat transfer in the exhaust port. Exhaust ports are sometimes isolated, which reduces the heat flow to the coolant, reassuring further oxidation of the combustion products due to the higher exhaust gas temperature. This extra energy can also be used by the turbine. Since we are only trying to model the in-cylinder pressure, the heat transfer in the exhaust port is not accounted for.

In-cylinder heat transfer

The in-cylinder heat transfer occurs by both convection and radiation, where convection constitutes the major part. This applies for most forced convection applications [Schmidt et al., 1993]. In SI engines, up to approximately 20 %, but

usually much less of the in-cylinder heat transfer is due to radiation [Woschni, 1967], but this is often included in the correlation for convective heat transfer. For CI engines however, the heat transfer originating from radiation can constitute a more significant part (up to 40 % [Heywood, 1988, p.696]) and has to be accounted for explicitly [Annand, 1963]. Since we are dealing with SI engines, only convective heat transfer is modeled, keeping in mind that the radiative heat transfer is accounted for by the correlations.

Heat transfer by convection is the transfer of energy between a fluid and a solid surface. The first phenomena is the diffusion or conduction of energy through the fluid because of the presence of a temperature gradient within the fluid. The diffusion and conduction is a molecular transport phenomena with a rate controlled by the thermophysical properties of the substance as well as the thermal environment. The second is the transfer of energy within the fluid due to the movement of the fluid from one thermal environment, temperature field, to another. This phenomenon is associated with the macroscopic characteristics, the movement or flow of the fluid, as well as the thermophysical characteristics of the fluid and the thermal characteristics of the solid [Schmidt et al., 1993].

The magnitude of the rate of energy transfer by convection \dot{Q}_{ht} , which occurs in a direction perpendicular to the fluid surface interface, is obtained by use of an expression referred to as Newton's law of cooling

$$\boxed{\dot{Q}_{ht} = h_c A \Delta T = h_c A (T - T_w)} \quad (3.24)$$

where A is the surface area of the body which is in contact with the fluid, ΔT is the appropriate temperature difference, and h_c is the convection heat transfer coefficient. The coefficient h_c varies both in time and space, and since it is a composite of both microscopic and macroscopic phenomena, many factors must be taken into consideration for a full understanding. This level of accuracy is needed if for example thermal stress on the cylinder head is to be investigated [Bergstedt, 2002]. On the other hand, a position-averaged heat transfer coefficient will be sufficient for predicting the heat flow to the coolant, and this will be the approach taken here. Note that $\dot{Q}_{ht} = \frac{dQ_{ht}}{dt}$, thus when simulating heat transfer in the crank angle domain

$$\boxed{\frac{dQ_{ht}}{d\theta} = \frac{dQ_{ht}}{dt} \frac{dt}{d\theta} = \dot{Q}_{ht} \frac{60}{2\pi N}} \quad (3.25)$$

should be used, where N [rpm] is the engine speed.

For various geometries, such as a cylinder, and assuming that the heat transfer is mainly caused by convection, the basic effects can be derived from the laws of similarity for turbulent tube flow. The turbulent flow conditions are given by the Reynolds number [Hohenberg, 1979]:

$$\text{Re} = \frac{\rho v L}{\mu} \quad (3.26)$$

This relates to the Nusselt number as:

$$\text{Nu} = a (\text{Re})^b \quad (3.27)$$

and the Nusselt number can be expressed as:

$$\text{Nu} = \frac{h_c L}{k} \quad (3.28)$$

where

ρ	gas density	$[kg/m^3]$
v	characteristic velocity	$[m/s]$
L	characteristic length	$[m]$
μ	gas dynamic viscosity	$[kg/(m\ s)]$
h_c	convection heat transfer coefficient	$[W/(m^2\ K)]$
k	gas thermal conductivity	$[W/(m\ K)]$

From these equations an expression for the heat transfer coefficient h_c can be formed as

$$h_c = a \frac{k}{L} \left(\frac{Lvp}{RT\mu} \right)^b \quad (3.29)$$

where the ideal gas law has been used in the expression for the density ρ . To get the heat transfer coefficient h_c the critical choices to be made are: (1) the characteristic length L and velocity v to be used in the Reynolds number; (2) the gas temperature at which to evaluate the gas properties in the Reynold and Nusselt numbers; and (3) the gas temperature to be used in the heat-transfer equation (3.24).

There exists several correlations for calculating the instantaneous heat transfer where most use the Nusselt-Reynolds number in (3.29), differing primarily in the way the Reynolds and Nusselt numbers are defined. This is due to differences in how to interpret the critical choices mentioned above. The lack of any generally accepted engine heat transfer model attests to the uncertainty of this aspect of heat release analysis.

Woschni's heat-transfer correlation

The form proposed by Woschni [1967] is based on the correlation of the form in (3.29). After assuming that the gas thermal conductivity k is proportional to $T^{0.75}$, where T is the average gas temperature and the gas dynamic conductivity μ being proportional to $T^{0.62}$, he arrived at an equation for the heat transfer coefficient:

$$h_c = C(pv)^b L^{b-1} T^{0.75-1.62b} \quad (3.30)$$

where C is a constant. By setting the exponent $b = 0.8$, which applies for turbulent flow in pipes, and choosing the cylinder bore diameter B as the characteristic length L , Woschni could now rewrite (3.30) as:

$$h_c = C(pv)^{0.8} B^{-0.2} T^{-0.55} \quad (3.31)$$

Woschni found that the exponent for T should be -0.53, but this is not consistent with (3.30). Woschni then states that the characteristic speed v depends on two terms. One is due to piston motion and is modeled as the mean piston speed u_p [m/s]. The other term is due to swirl originating from the combustion event, which is modeled as a function of the pressure rise due to combustion, i.e. $p - p_0$ where p_0 is the motored pressure. Woschni used the measured motored pressure, but later on Watson and Janota [1982] proposed to use a polytropic process model instead:

$$p_0 = p_{ref} \left(\frac{V_{ref}}{V} \right)^n \quad (3.32)$$

where n is the polytropic exponent, and (p_{ref}, V_{ref}) are evaluated at any reference condition. The characteristic speed v can then be expressed as:

$$v = C_1 u_p + C_2 (T - T_0) = C_1 u_p + C_2 \frac{V T_r}{p_{ref} V_{ref}} (p - p_0) \quad (3.33)$$

where the first term originates from convection caused by piston motion and the second term from the combustion itself, where T_0 is the motored mean gas temperature. This results in the following expression for the heat transfer coefficient h_c ¹:

$$h_c = \frac{0.013 B^{-0.2} p^{0.8} \left(C_1 u_p + \frac{C_2 (p-p_0) T_r V_i}{p_r V_r} \right)^{0.8}}{T^{0.55}} \quad (3.34)$$

where

p	cylinder pressure for firing cycle	[Pa]
p_0	cylinder pressure for motored cycle	[Pa]
T	mean gas temperature	[K]
u_p	mean piston speed	[m/s]
V	instantaneous cylinder volume	[m ³]
C_1	constant	[-]
C_2	constant	[m/(s K)]
$(p_{ref}, V_{ref}, T_{ref})$	evaluated at any reference condition ref	

Woschni found experimentally that during the gas exchange process, the parameters $C_1 = 6.18$ and $C_2 = 0$ should be used, but during the closed part of the engine cycle, i.e. during compression, combustion and expansion, the parameters $C_1 = 2.28$ and $C_2 = 3.24 \cdot 10^{-3}$ were found to give a better fit. Woschni also pointed out that the parameters (C_1, C_2) are engine dependent, and are therefore likely to change for different engine geometries.

¹The numerical value of the first coefficient differs from the one in [Woschni, 1967], since it is calculated to fit the SI-unit system

Hohenberg's heat transfer correlation

Hohenberg [1979] proposed a new correlation for the heat transfer coefficient, and in doing so he uses (3.29) and reviews Woschni's correlation (3.31) with some modifications; First Hohenberg argues that the piston land area must be included in the convective surface area in (3.24). This area is proposed to be:

$$A = A_{\text{chamber}} + 0.3 \cdot A_{\text{piston land}} \quad (3.35)$$

where it is assumed that the heat transfer in the piston land is 30 % of that in the combustion chamber, and with $A_{\text{piston land}} = \pi B^2 / 4$. If the heat release model used includes a model for the crevice effect, this extra term is probably already accounted for.

Secondly, Hohenberg suggests that the characteristic length L in (3.29) should be interpreted as the diameter D of a ball with the same volume as the instantaneous cylinder volume V :

$$V = \frac{D^3 \pi}{6} \rightarrow D \propto V^{1/3} \rightarrow D^{-0.2} \propto V^{-0.066} \quad (3.36)$$

Hohenberg then compensates for radiation by letting $D^{-0.2} \propto V^{-0.06}$, referring to that increased diameter yields increased radiation.

Thirdly, the characteristic speed v is modeled as:

$$v^{0.8} = p^{0.2} T^{0.1} (u_p + C_2)^{0.8} \quad (3.37)$$

A constant term C_2 is included for the combustion, and therefore seems less flexible to deal with different operating points compared to the Woschni correlation. This also means that C_2 should be set to 0 for motored cycles. Hohenberg comments upon this that the extra computation for Woschni's term is not worth the effort. Last but not least, some exponents in (3.31) are altered to give a better fit to experimental data.

The resulting expression for the convective heat transfer coefficient is therefore:

$$h_c = C_1 V^{-0.06} p^{0.8} T^{-0.4} (u_p + C_2)^{0.8} \quad (3.38)$$

where

h_c	heat transfer coefficient	$[W/(m^2 K)]$
V	instantaneous cylinder volume	$[m^3]$
p	instantaneous cylinder pressure	$[Pa]$
T	mean gas temperature	$[K]$
u_p	mean piston speed	$[m/s]$
C_1	Constant	$[-]$
C_2	Constant	$[m/s]$

The mean values for the parameters (C_1, C_2) are found experimentally for diesel engines to be: ²

$$C_1 = 13 \cdot 10^{-3} \text{ and } C_2 = 1.4$$

²The numerical value of C_1 differs from the one in [Hohenberg, 1979], since it is calculated to fit the SI-unit system

Just as Woschni, Hohenberg states that the parameters are likely to differ for various engines.

Summarizing works on heat transfer

In the example model in section 2.5 from Gatowski et al. [1984], the heat transfer was modeled using (3.34) from Woschni [1967]. The work by Shayler et al. [1993] compared the correlations from Annand [1963] and Woschni [1967] among others, and found that the heat transfer to the coolant best agreed with the Woschni correlation. At the same time, Hayes et al. [1993] also examined the accuracy of the Woschni correlation and reported good agreement with the measurement results for a four-cylinder spark-ignited engine. The works by Pivec et al. [1998] and Wimmer et al. [2000] investigate different heat transfer correlations both during the closed part of the engine cycle and during the gas exchange processes. They again found that Woschni's correlation proved to be the better one for the closed part.

However, the variation in heat transfer correlations does not have a significant influence on the engine performance prediction. Typically, a 10 per cent error in the prediction of in-cylinder heat transfer leads to an error in the order of 1 per cent for the engine performance [Stone, 1999, p.429]. This is also supported by the sensitivity analysis performed in section 3.8, where all parameters are perturbed 10 % from their nominal values. There it was found that the two Woschni parameters C_1 and C_2 does not affect the resulting cylinder pressure significantly. Our choice will therefore be to use the Woschni heat transfer correlation, since it is most widely used and since a heat transfer modeling error does not affect the cylinder pressure immensely.

Parameter initialization – $\{C_1, C_2\}$

The parameters values found by Woschni and Hohenberg respectively, serves well as initializations. For the Woschni heat transfer coefficient (3.34) the parameter values $C_1 = 2.28$ and $C_2 = 3.24 \cdot 10^{-3}$ are used, and for the Hohenberg heat transfer coefficient (3.38) the parameter values $C_1 = 13 \cdot 10^{-3}$ and $C_2 = 1.4$ are used.

3.8 Sensitivity in pressure to parameter initialization

The cylinder pressure is simulated for the nominal values in the table 3.1, and yields the cylinder pressure given in figure 3.5. To get an idea of how sensitive the cylinder pressure is to errors in the initialized parameters, a modest sensitivity analysis is performed by perturbing the parameters one at a time with 10 per cent of their nominal value.

Par.	Nominal Value		RMSE [kPa]	Max Res [kPa]
γ_{300}	1.3678	[-]	204.0	541.0
V_c	35.5	[cm^3]	84.1	237.0
K_p	1	[-]	75.3	186.0
p_{ivc}	50	[kPa]	42.8	97.5
T_w	440	[K]	41.8	99.6
Q_{in}	500	[J]	38.3	99.6
θ_{ig}	-15	[deg ATDC]	33.9	122.0
θ_d	20	[deg]	28.2	106.0
θ_b	30	[deg]	22.1	84.8
T_{ivc}	340	[K]	16.7	45.4
b	$-8.13 \cdot 10^{-5}$	[K^{-1}]	7.0	21.1
Δp	30	[kPa]	3.0	3.0
V_{cr}	1	[% V_c]	1.7	5.3
C_2	$3.24 \cdot 10^{-3}$	[$m/(s K)$]	1.4	3.0
C_1	2.28	[-]	0.9	1.6
θ_0	0.4	[deg]	0.8	2.2

Table 3.1: Nominal values, and their respective root mean square error (RMSE) and maximal residual when perturbing the nominal values with 10 %.

The perturbed simulated cylinder pressure is then compared to the nominal one, in the measured root mean square error (RMSE) and maximum absolute residual value (Max Res). The results are summarized in table 3.1. When comparing the RMSE for every parameter, the constant γ_{300} in the linear specific heat ratio model, the clearance volume V_c and the pressure gain K_p show most sensitivity in the mean and are therefore more in need of a proper initialization than the others. On the other hand, disturbances in the values of the two Woschni parameters C_1 and C_2 do not affect the resulting cylinder pressure significantly. Note that the model of the cylinder pressure is nonlinear, so the results found from this analysis is only valid locally, but it still gives an idea of which parameters are the most sensitive ones.

3.9 Summary of single-zone heat-release models

The model component equations, which are boxed in chapter 2 and 3, for the Gatowski et al.-model are given here as a summary, together with the inputs, outputs and unknown parameters for the model.

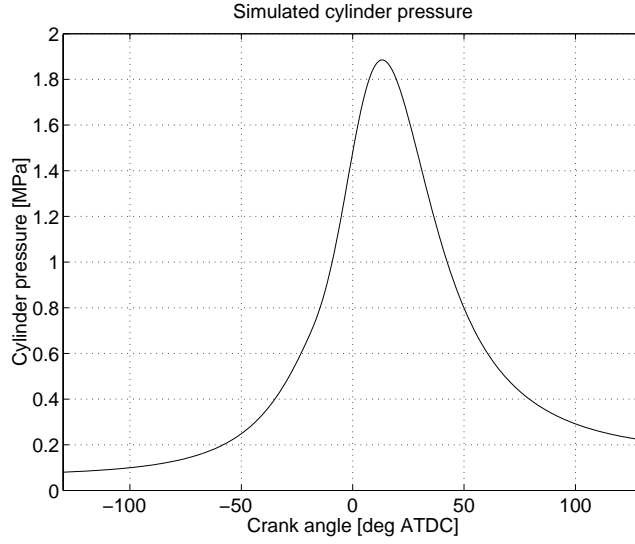


Figure 3.5: Simulated cylinder pressure using nominal values in table 3.1.

Model input and output

Input	Description	Unit
λ	air-fuel ratio	[-]
N	engine speed	[rpm]
p_{exh}	exhaust manifold pressure	[Pa]
p_{man}	intake manifold pressure	[Pa]
T_{man}	intake manifold temperature	[K]
θ_{IVC}	crank angle degree for IVC	[deg ATDC]
Output	Description	Unit
p	cylinder pressure	[Pa]
Q_{ch}	chemical energy released as heat	[J]

Model component equations

Cylinder pressure differential (2.33);

$$dp = \frac{\dot{d}Q_{ch} - \frac{\gamma}{\gamma-1} p dV - \dot{d}Q_{ht}}{\frac{1}{\gamma-1} V + \frac{V_{ex}}{T_w} \left(\frac{T}{\gamma-1} - \frac{1}{b} \ln \left(\frac{\gamma-1}{\gamma'-1} \right) + T' \right)} \quad (3.39)$$

Pressure sensor model (3.1);

$$p_m = K_p p + \Delta p \quad (3.40)$$

Crank angle phasing (3.2);

$$\theta_i + \theta_0 = \theta_{i,\text{true}} \quad (3.41)$$

Cylinder volume $V(\theta, x_{\text{off}})$ (3.3), (3.4) and (3.8);

$$V(\theta, x_{\text{off}}) = V_c(x_{\text{off}}) + V_{id}(\theta, x_{\text{off}}) \quad (3.42a)$$

$$V_{id}(\theta, x_{\text{off}}) = \frac{\pi B^2}{4} (\sqrt{(l+a)^2 - x_{\text{off}}^2} - a \cos \theta - \sqrt{l^2 - (x_{\text{off}} + a \sin \theta)^2}) \quad (3.42b)$$

$$\frac{dV(\theta)}{d\theta} = \frac{\pi B^2 a}{4} \left(\sin \theta + \frac{(x_{\text{off}} + a \sin \theta) \cos \theta}{\sqrt{l^2 - (x_{\text{off}} + a \sin \theta)^2}} \right) \quad (3.42c)$$

Temperature model (3.11);

$$T = \frac{T_{IVC}}{p_{IVC} V_{IVC}} p V \quad (3.43)$$

Crevise model (3.16);

$$dm_{cr} = \frac{V_{cr}}{R T_w} dp \quad (3.44)$$

Vibe combustion model (3.20), (3.18) and (3.19);

$$\frac{dQ_{ch}}{d\theta} = m_f q_{HV} \eta_f \frac{dx_b}{d\theta} = Q_{in} \frac{dx_b}{d\theta} \quad (3.45a)$$

$$\frac{dx_b(\theta)}{d\theta} = \frac{a(m+1)}{\Delta\theta} \left(\frac{\theta - \theta_{ig}}{\Delta\theta} \right)^m e^{-a \left(\frac{\theta - \theta_{ig}}{\Delta\theta} \right)^{m+1}} \quad (3.45b)$$

$$m = \frac{\ln(\ln(1-0.1) - \ln(1-0.85))}{\ln \theta_d - \ln(\theta_d + \theta_b)} - 1 \quad (3.45c)$$

$$a = - \left(\frac{\Delta\theta}{\theta_d} \right)^{m+1} \ln(1-0.1) \quad (3.45d)$$

Specific heat ratio model (4.2);

$$\gamma_{in}(T) = \gamma_{300} + b(T - 300) \quad (3.46)$$

Woschni's heat transfer correlation (3.25), (3.24), (3.34) and (3.10);

$$\frac{dQ_{ht}}{d\theta} = \frac{dQ_{ht}}{dt} \frac{dt}{d\theta} = \dot{Q}_{ht} \frac{60}{2\pi N} \quad (3.47a)$$

$$\dot{Q}_{ht} = h_c A \Delta T = h_c A (T - T_w) \quad (3.47b)$$

Par.	Description	Value	Equation
γ_{300}	constant specific heat ratio [-]	1.3678	(3.23)
b	slope for specific heat ratio [K^{-1}]	$-8.13 \cdot 10^{-5}$	(4.2)
C_1	heat-transfer parameter [-]	2.28	(3.34)
C_2	heat-transfer parameter [-]	$3.24 \cdot 10^{-3}$	(3.34)
θ_0	crank angle phasing [deg ATDC]	0.4	(3.2)
Δp	bias in pressure measurements [kPa]	30	(3.1)
K_p	pressure measurement gain[-]	1	(3.1)
p_{ivc}	cylinder pressure at IVC [kPa]	100	(3.11)
T_{ivc}	mean charge temperature at IVC [K]	340	(3.11)
T_w	mean wall temperature [K]	440	(3.16),(3.24)
V_c	clearance volume [cm^3]	35.5	(3.3)
V_{cr}	single aggregate crevice volume [% V_c]	1	(3.16)
θ_{ig}	ignition angle [deg ATDC]	-20	(3.18)
θ_d	flame-development angle [deg ATDC]	15	(3.18)
θ_b	rapid-burn angle [deg ATDC]	30	(3.18)
Q_{in}	released energy from combustion [J]	500	(3.20)

Table 3.2: Nominal values for the parameters in the Gatowski et al. single-zone heat release model. For firing cycles, $T_w = 440$ K and $T_{ivc} = 340$ K, and for motored cycles, $T_w = 400$ K and $T_{ivc} = 300$ K.

$$h_c = \frac{0.013 B^{-0.2} p^{0.8} \left(C_1 u_p + \frac{C_2 (p-p_0) T_r V_i}{p_r V_r} \right)^{0.8}}{T^{0.55}} \quad (3.47c)$$

$$A(\theta) = \frac{\pi B^2}{2} + \pi B \left(\sqrt{(l+a)^2 - x_{off}^2} - a \cos \theta - \sqrt{l^2 - (x_{off} + a \sin \theta)^2} \right) \quad (3.47d)$$

Unknown parameters

The parameters used in the single-zone model and their nominal values are summarized in table 3.2.

A SPECIFIC HEAT RATIO MODEL FOR SINGLE-ZONE HEAT RELEASE MODELS

An accurate specific heat ratio model is important for an accurate heat release analysis, since the specific heat ratio couples the systems energy to other thermodynamic quantities. The objective is therefore to investigate models of the specific heat ratio for the single-zone heat release model, and find a model accurate enough to introduce a cylinder pressure modeling error less than or in the order of the cylinder pressure measurement noise, while keeping the computational complexity at a minimum. Based on assumptions of frozen mixture for the unburned mixture and chemical equilibrium for the burned mixture, the specific heat ratio is calculated using a full equilibrium program for an unburned and a burned air-fuel mixture, and compared to already existing and newly proposed models of γ .

A two-zone mean temperature model and the Vibe function are used to parameterize the mass fraction burned. The mass fraction burned is used to interpolate the specific heats for the unburned and burned mixture, and then form the specific heat ratio, which renders a small enough modeling error in γ . The impact that this modeling error has on the cylinder pressure is less than that of the measurement noise. The specific heats for the unburned mixture are captured within 0.2 % by linear functions, and the specific heats for the burned mixture are captured within 1 % by higher-order polynomials for the major operating range of a spark ignited (SI) engine.

Large parts of the material in this chapter and in appendix A has previously been published in Klein and Eriksson [2004]. Appendix A is an extension of the appendices in Klein and Eriksson [2004], and contains further details and argumentation that support the specific heat ratio models, as well as it gives a

thorough explanation of some of the details in the models.

4.1 Introduction

The accuracy with which the energy balance can be calculated for a combustion chamber depends in part on how accurately changes in the internal energy of the cylinder charge are represented. The most important thermodynamic property used when calculating the heat release rates in engines is the ratio of specific heats, $\gamma(T, p, \lambda) = \frac{c_p}{c_v}$ [Gatowski et al., 1984; Chun and Heywood, 1987; Guezennec and Hamama, 1999].

Based on the first law of thermodynamics, Gatowski et al. [1984] developed a single-zone heat release model that has been widely used, where the specific heat ratio is represented by a linear function in mean charge temperature T :

$$\gamma_{lin}(T) = \gamma_{300} + b(T - 300) \quad (4.1)$$

This allows a critical examination of the burning process by analysis of the heat release. In order to compute the heat release correctly, the parameters in the single-zone model need to be well tuned. These parameters, such as heat transfer coefficients, γ_{300} and b in the linear γ -model (4.1) and so on, can be tuned using well known methods. For instance, Eriksson [1998] uses standard prediction error methods [Ljung, 1999] to tune the parameters. This is done by minimizing the prediction error of the measured cylinder pressure, i.e. by minimizing the difference between the modeled and measured cylinder pressure. Applying these standard methods usually ends up in absurd and non-physical values of γ_{300} , as it becomes larger than 1.40, which is the value of γ_{300} for pure air. But more importantly, the linear approximation of γ (4.1) itself introduces a model error in the cylinder pressure which has a root mean square error of approximately 30 kPa, for low load engine operating points, and approximately 90 kPa in the mean for operating points covering the entire operating range. These errors are more than four and ten times the error introduced by the measurement noise, and will affect the computed heat release. Therefore a better model of $\gamma(T, p, \lambda)$ is sought. A correct model of $\gamma(T, p, \lambda)$ is also desirable in order to avoid badly tuned (biased) parameters.

The objective is to investigate models of the specific heat ratio for the single-zone heat release model, and find a model accurate enough to introduce a modeling error less than or in the order of the cylinder pressure measurement noise, while keeping the computational complexity at a minimum. Such a model would help us to compute a more accurate heat release trace.

4.1.1 Outline

In the following section three existing γ -models are described. Then based on chemical equilibrium, a reference model for the specific heat ratio is described. Thereafter, the reference model is calculated for an unburned and a burned

air-fuel mixture respectively, and compared to these existing models in the two following sections. With the knowledge of how to describe γ for the unburned and burned mixture respectively, the focus is turned to finding a γ -model during the combustion process, i.e. for a partially burned mixture. This is done in section 4.6, where a number of approximative models are proposed. These models are evaluated in terms of the normalized root mean square error related to the reference γ -model found from chemical equilibrium, as well as the influence the models have on the cylinder pressure, and also in terms of computational time.

4.2 Existing models of γ

The computational time involved in repeated use of a full equilibrium program, such as CHEPP [Eriksson, 2004] or the NASA program [Svehla and McBride, 1973], can be substantial, and therefore models of the thermodynamic properties have been developed. Three such models will now be described.

4.2.1 Linear model in T

The specific heat ratio during the closed part of the cycle, i.e. when both intake and exhaust valves are closed, is most frequently modeled as either a constant, or as a linear function of temperature. The latter model is used in [Gatowski et al., 1984], where it is stated that the model approximation is in parity with the other approximations made for this family of single-zone heat-release models. The linear function in T can be written as:

$$\gamma_{lin}(T) = \gamma_{300} + b(T - 300) \quad (4.2)$$

Depending on which temperature region and what air-fuel ratio λ the model will be used for, the slope b and constant γ_{300} in (4.2) have to be adjusted. Concerning the temperature region, this shortcoming can be avoided by increasing the complexity of the model and use a second (or higher) order polynomial for $\gamma_{lin}(T)$. This has been done in for example Brunt et al. [1998]. Such an extension reduces the need for having different values of γ_{300} and b for different temperature regions. Later on, $\gamma_{lin}(T)$ is calculated in a least squares sense for both burned and unburned mixtures.

4.2.2 Segmented linear model in T

According to Chun and Heywood [1987], the commonly made assumption that $\gamma(T)$ is constant or a linear function of mean temperature is not sufficiently accurate. Instead, they propose a segmentation of the closed part of the engine cycle into three segments; compression, combustion and post-combustion (expansion). Both the compression and post-combustion are modeled by linear functions of T , while the combustion event is modeled by a constant γ . They

further state that with these assumptions, the one-zone analysis framework will provide accurate enough predictions. The model of γ can be written as:

$$\gamma_{seg}(T, x_b) = \begin{cases} \gamma_{300}^{comp} + b^{comp}(T - 300) & x_b < 0.01 \\ \gamma_{300}^{comb} & 0.01 \leq x_b \leq 0.99 \\ \gamma_{300}^{exp} + b^{exp}(T - 300) & x_b > 0.99 \end{cases} \quad (4.3)$$

where the mass fraction burned x_b is used to classify the three phases. The γ -model proposed by Chun and Heywood [1987] has discontinuities when switching between the phases compression, combustion and post-combustion. This can pose a problem when estimating e.g. the mass fraction burned.

4.2.3 Polynomial model in p and T

The third model is a polynomial model of the internal energy u developed in Krieger and Borman [1967] for combustion products of C_nH_{2n} , e.g. iso-octane. For weak and stoichiometric mixtures ($\lambda \geq 1$), a single set of equations could be stated, whereas different sets were found for each $\lambda < 1$. The model of u for $\lambda \geq 1$ is given by:

$$u(T, p, \lambda) = A(T) - \frac{B(T)}{\lambda} + u_{corr}(T, p, \lambda) \quad (4.4)$$

given in [kJ/(kg of original air)], where

$$A(T) = a_1T + a_2T^2 + \dots + a_5T^5 \quad (4.5a)$$

$$B(T) = b_0 + b_1T + \dots + b_4T^4 \quad (4.5b)$$

The gas constant was found to be:

$$R(T, p, \lambda) = 0.287 + \frac{0.020}{\lambda} + R_{corr}(T, p, \lambda) \quad (4.6)$$

given in [kJ/(kg of original air) K]. Krieger and Borman suggested that the correction terms u_{corr} and R_{corr} should account for dissociation, that they are non-zero for $T > 1450$ K and are given by:

$$u_{corr}(T, p, \lambda) = c_u \exp(D(\lambda) + E(T, \lambda) + F(T, p, \lambda)) \quad (4.7a)$$

$$D(\lambda) = d_0 + d_1\lambda^{-1} + d_3\lambda^{-3} \quad (4.7b)$$

$$E(T, \lambda) = \frac{e_0 + e_1\lambda^{-1} + e_3\lambda^{-3}}{T} \quad (4.7c)$$

$$F(T, p, \lambda) = (f_0 + f_1\lambda^{-1} + f_3\lambda^{-3} + \frac{f_4 + f_5\lambda^{-1}}{T}) \ln(f_6p) \quad (4.7d)$$

a_1 0.692	a_2 $39.17 \cdot 10^{-6}$	a_3 $52.9 \cdot 10^{-9}$	a_4 $-228.62 \cdot 10^{-13}$
a_5 $277.58 \cdot 10^{-17}$	b_0 3049.33	b_1 $-5.7 \cdot 10^{-2}$	b_2 $-9.5 \cdot 10^{-5}$
b_3 $21.53 \cdot 10^{-9}$	b_4 $-200.26 \cdot 10^{-14}$	c_u 2.32584	c_r $4.186 \cdot 10^{-3}$
d_0 10.41066	d_1 7.85125	d_3 -3.71257	e_0 $-15.001 \cdot 10^3$
e_1 $-15.838 \cdot 10^3$	e_3 $9.613 \cdot 10^3$	f_0 -0.10329	f_1 -0.38656
f_3 0.154226	f_4 -14.763	f_5 118.27	f_6 14.503
r_0 -0.2977	r_1 11.98	r_2 -25442	r_3 -0.4354

Table 4.1: Coefficient values for Krieger-Borman polynomial given in (4.5)-(4.8).

$$R_{corr}(T, p, \lambda) = c_r \exp \left(r_0 \ln \lambda + \frac{r_1 + r_2/T + r_3 \ln(f_6 p)}{\lambda} \right) \quad (4.8)$$

where T is given in Kelvin (K) and p in bar. The values of the coefficients are given in Table 4.1. For a fuel of composition $C_n H_{2n}$, the stoichiometric fuel-air ratio is 0.0676. Therefore, equations (4.4)-(4.6) should be divided by $(1 + 0.0676\lambda^{-1})$, to get the internal energy per unit mass of products. In general, the error in u was found to be less than 2.5 per cent in the pressure and temperature range of interest, where the extreme end states were approximately $\{2300 \text{ K}, 0.07 \text{ MPa}\}$ and $\{3300 \text{ K}, 35 \text{ MPa}\}$, and less than 1 per cent over most of the range. A model of γ is then found as

$$\gamma_{KB} = \frac{c_p}{c_v} = 1 + \frac{R}{c_v} \quad (4.9)$$

where R is given by (4.6) and $c_v = \frac{\partial u}{\partial T}$ is found by differentiating (4.4) with respect to T .

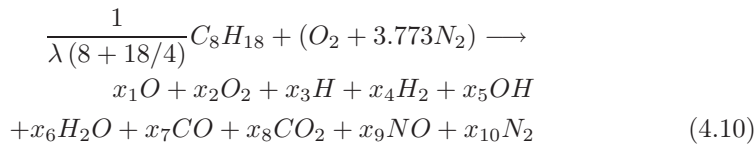
4.2.4 Summary of existing γ -models

Apparently there are ambiguities in which model structure to use for γ , therefore $\gamma(T, p, \lambda)$ is calculated for adequate temperature and pressure regions for both unburned and burned mixture, assuming that the unburned cylinder charge is frozen and the burned mixture is at equilibrium at every instant. This in order to find out what model structure of γ that is accurate enough for our purposes. One such purpose is to estimate parameters in the single-zone model such as heat transfer coefficients, burn rate parameters and so on, using the

measured cylinder pressure. This requires a model of the cylinder pressure in which the γ -model has a key role, and therefore the impact each γ -model has on the cylinder pressure is monitored. All thermodynamic properties depend on the air-fuel ratio λ , but for notational convenience this dependence is hereafter left out when there is no explicit dependence.

4.3 Chemical equilibrium

According to Heywood [1988, p.86], it is a good approximation for performance estimates to consider the unburned gases as frozen and the burned gases as in chemical equilibrium. However, the latter assumption is not valid late in the expansion stroke. Assuming that the unburned air-fuel mixture is frozen and that the burned mixture is at equilibrium at every instant, the specific heat ratio and other thermodynamic properties of various species can be calculated using the Matlab package CHEPP [Eriksson, 2004]. The fuel iso-octane, C_8H_{18} , reacts with air according to:



where the products given on the right hand side are chosen by the user and λ is the air-fuel ratio (AFR). The coefficients x_i are found by CHEPP and when scaled properly with λ they reveal the mole fraction of specie i that the mixture consists of at a given temperature, pressure and air-fuel ratio. The mixture is assumed to obey the Gibbs-Dalton law, which states that under the ideal-gas approximation, the properties of a gas in a mixture are not influenced by the presence of other gases, and each gas component in the mixture behaves as if it exists alone at the mixture temperature and mixture volume [Çengel and Boles, 2002, Ch 12]. Therefore, the properties can be added together as e.g. in:

$$u(T, p) = \sum_i x_i(T, p) u_i(T) \quad (4.11)$$

where u_i is the internal energy from specie x_i and u is the total internal energy.

4.4 Unburned mixture

First of all, the specific heat ratio for an unburned frozen mixture of iso-octane is computed using CHEPP in the temperature region $T \in [300, 1000]$ K, which is valid for the entire closed part of a motored cycle. The specific heat ratio for air-fuel ratio $\lambda = 1$ is shown in figure 4.1 as a function of temperature, together with its linear approximation (4.2) in a least squares sense. The linear approximation

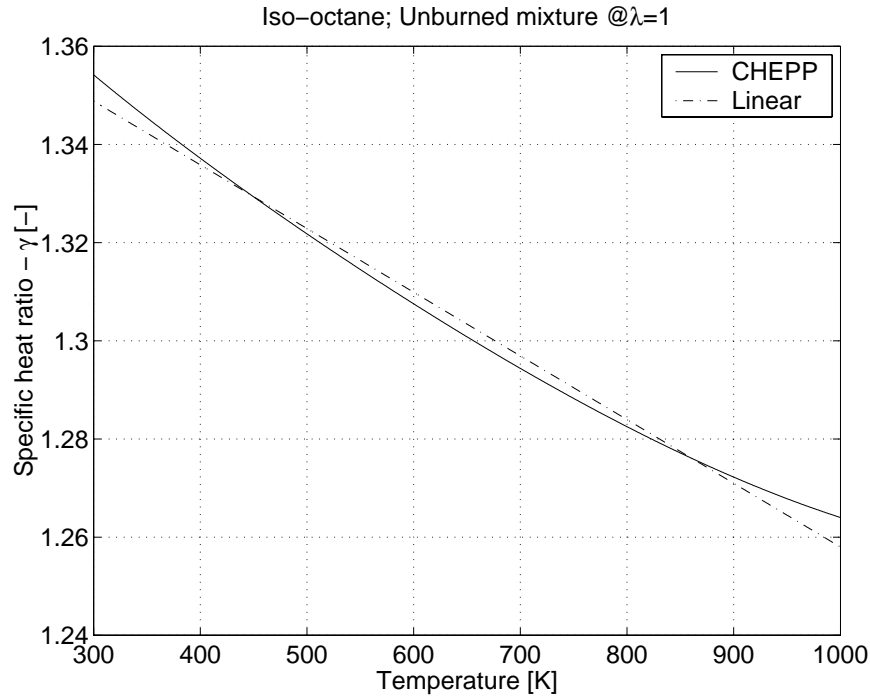


Figure 4.1: Specific heat ratio for unburned stoichiometric mixture using CHEPP and the corresponding linear function of temperature.

Property	Constant	Slope	NRMSE	RMSE
γ_{lin}^u [-]	1.3488	$-13.0 \cdot 10^{-5}$	0.19 %	0.0024
$c_{p,u}^{lin}$ [J/(kg K)]	1051.9	0.387	0.15 %	1.78
$c_{v,u}^{lin}$ [J/(kg K)]	777.0	0.387	0.20 %	1.78

Table 4.2: Coefficients, normalized RMSE and RMSE in linear approximations of γ , mass-specific c_v and c_p , for temperature region $T \in [300, 1000]$ K and $\lambda = 1$

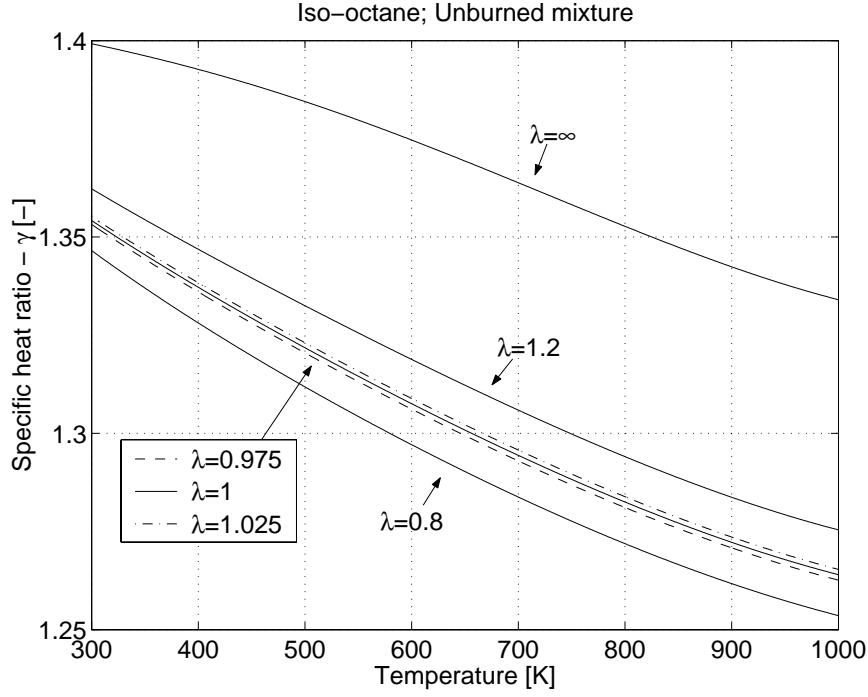


Figure 4.2: Specific heat ratio for unburned stoichiometric mixture using CHEPP for various air fuel ratios λ as functions of temperature. $\lambda = \infty$ corresponds to pure air.

γ_{lin}^u is fairly good for $\lambda = 1$. Actually, the specific heats c_p and c_v from which γ is formed, are fairly well described by linear functions of temperature. Table 4.2 summarizes the root mean square error (RMSE), normalized RMSE (NRMSE) and the coefficients of the respective linear function for γ , mass-specific heats c_v and c_p for temperature region $T \in [300, 1000]$ K and $\lambda = 1$. The RMSE of γ_{lin}^u is defined as:

$$RMSE = \sqrt{\frac{1}{M} \sum_{j=1}^M (\gamma(T_j) - \gamma_{lin}^u(T_j))^2} \quad (4.12)$$

where M are the number of samples. The NRMSE is then found by normalizing RMSE with the mean value of $\gamma(T)$:

$$NRMSE = \frac{RMSE}{\frac{1}{M} \sum_{j=1}^M \gamma(T_j)} \quad (4.13)$$

Besides temperature, the specific heat ratio also varies with AFR, as shown

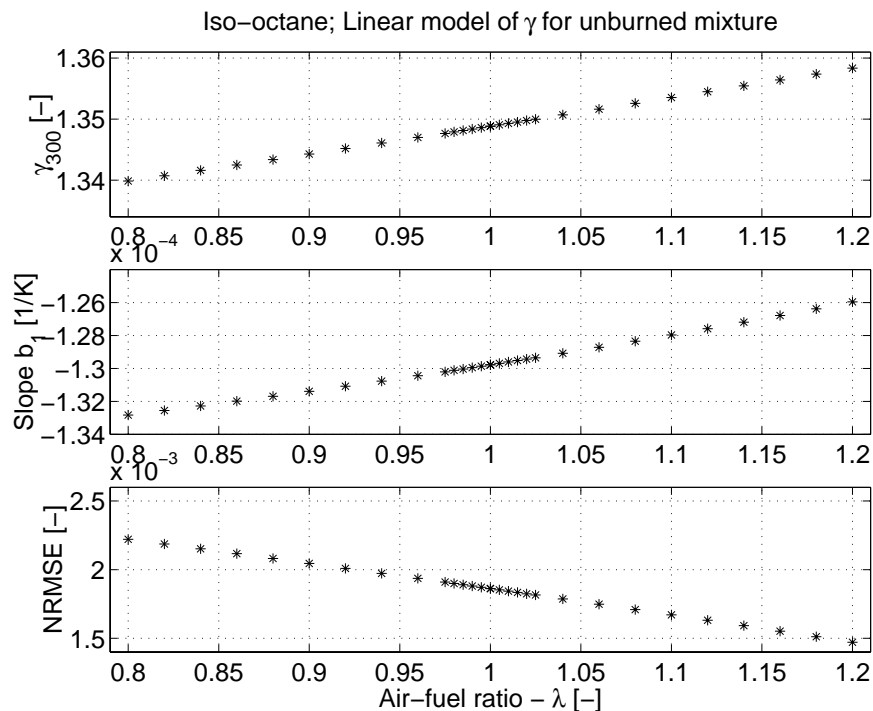


Figure 4.3: *Upper:* The constant value γ_{300} in (4.2) as a function of λ for unburned mixture at equilibrium. *Middle:* The value of the slope coefficient b in (4.2) as a function of AFR. *Bottom:* Normalized root mean square error (NRMSE) for $\gamma_{lin}^u(T)$.

in figure 4.2 where λ is varied between 0.8 (rich) and 1.2 (lean). For comparison, $\gamma(T)$ is also shown for $\lambda = \infty$, i.e. pure air which corresponds to fuel cut-off.

The coefficients in γ_{lin}^u (4.2) vary with λ as shown in the two upper plots of figure 4.3. Both the constant γ_{300} and the slope b become smaller as the air-fuel ratio becomes richer. From the bottom plot of figure 4.3, which shows the NRMSE for different AFR:s, it can be concluded that the linear approximation $\gamma_{lin}^u(T)$ is better the leaner the mixture is, at least for $\lambda \in [0.8, 1.2]$.

4.4.1 Modeling λ -dependence with fix slope, b

Since it is always desirable to have as simple models as possible, an important question is: –Would it inflict a major discrepancy to fix the slope coefficient b and let only γ_{300} vary with the air-fuel ratio? This is investigated by setting the slope b to the value for $\lambda = 1$, and find the coefficient γ_{300} in a least squares sense. The slope is fixed at $\lambda = 1$, since for spark ignited engines this is the

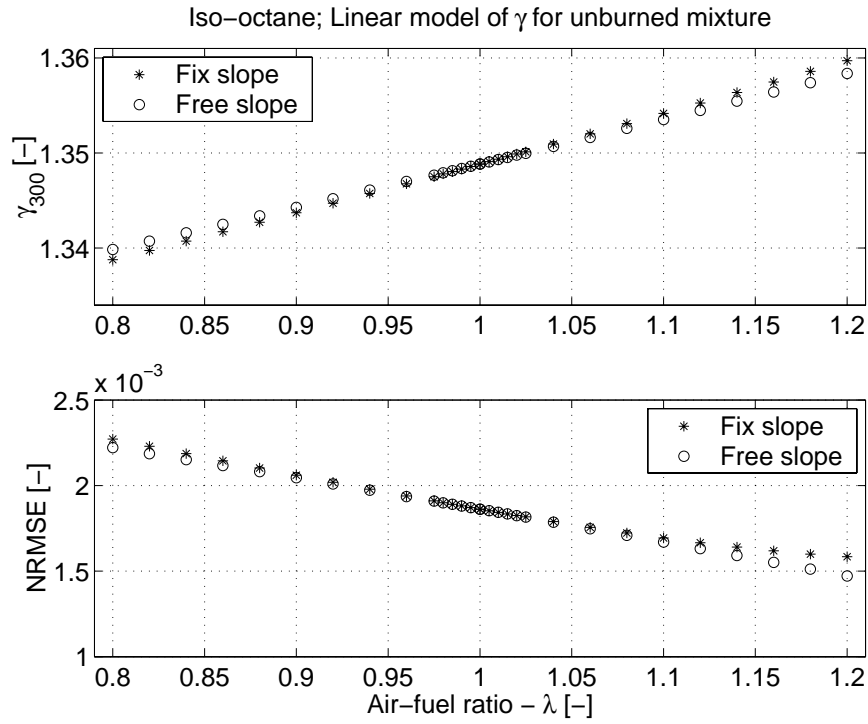


Figure 4.4: *Upper*: The constant value γ_{300} in (4.2) as a function of λ for unburned mixture at equilibrium with fixed and free slope b respectively. *Bottom*: NRMSE for $\gamma_{lin}^u(T)$ for fixed and free slope coefficient.

region where the engine should be operating most of the time, if controlled correctly. This approach leads to figure 4.4, where the coefficient γ_{300} becomes approximately the same as when letting the slope vary. The relative difference is less than 0.1 % for $\lambda \in [0.8, 1.2]$. For the NRMSE an increase for $\lambda \neq 1$ is expected, but the increase is not very significant at all, for $\lambda \in [0.8, 1.12]$ the relative difference in RMSE is less than 5 % and for $\lambda \in [0.94, 1.06]$ it is less than 1 %. This suggests that at least for $\lambda \in [0.94, 1.06]$, the linear approximation with fixed slope set at $\lambda = 1$, can be used as a model of $\gamma(T)$ with good accuracy for the unburned mixture. The parameter γ_{300} is therefore taking care of the λ -dependence with good accuracy.

4.5 Burned mixture

The specific heat ratio γ for a burned mixture of iso-octane is computed using CHEPP in temperature region $T \in [500, 3500]$ K and pressure region $p \in [0.25, 100]$ bar, which covers most of the closed part of a firing cycle. The mixture is assumed to be at equilibrium at every instant. The specific heat ratio is strongly dependent on mixture temperature T , but γ also depends upon the air-fuel ratio λ and pressure p as shown in figure 4.5 and figure 4.6 respectively. For the same deviation from $\lambda = 1$, rich mixtures tend to deviate more from the stoichiometric mixture, than lean mixtures do. The pressure dependence of γ is only visible for $T > 1500$ K, and a higher pressure tends to retard the dissociation and yields a higher γ .

To model the specific heat ratio with a linear function $\gamma_{lin}^b(T)$ of temperature, and thereby neglecting the dependence of pressure, will of course introduce a modeling error. This modeling error depends on which temperature (and pressure) region the linear function is estimated for, since different regions will yield different coefficient values in (4.2). In figure 4.7 γ is computed at $\lambda = 1$ and $p = 7.5$ bar for $T \in [500, 3500]$ K, and as well as the corresponding linear function γ_{lin}^b (4.2) and the polynomial γ_{KB} (4.9) developed by Krieger and Borman [1967].

The linear approximation $\gamma_{lin}^b(T)$ does not capture the behavior of $\gamma(T)$ for $\lambda = 1$ very well. The coefficients for the linear model $\gamma_{lin}^b(T)$ vary for the specific temperature region. They are given for temperature regions A to E in Table 4.3. A second order polynomial shows the same behavior as the linear case, but when the order of the polynomial is increased to three, the model captures the modes of $\gamma(T)$ quite well. By increasing the complexity of the model even more, an even better fit is found. This has been done in the Krieger-Borman polynomial, and for this example it captures the behavior of $\gamma(T)$ well for temperatures below 2800 K as seen in figure 4.7 and in the right-most (NRMSE) column in table 4.4, where the NRMSE value is much higher for temperature region A than for the other regions. In table 4.4, the NRMSE and maximum relative error (MRE) for the linear approximation γ_{lin}^b and the Krieger-Borman polynomial γ_{KB} at various temperature regions are given. As expected, the

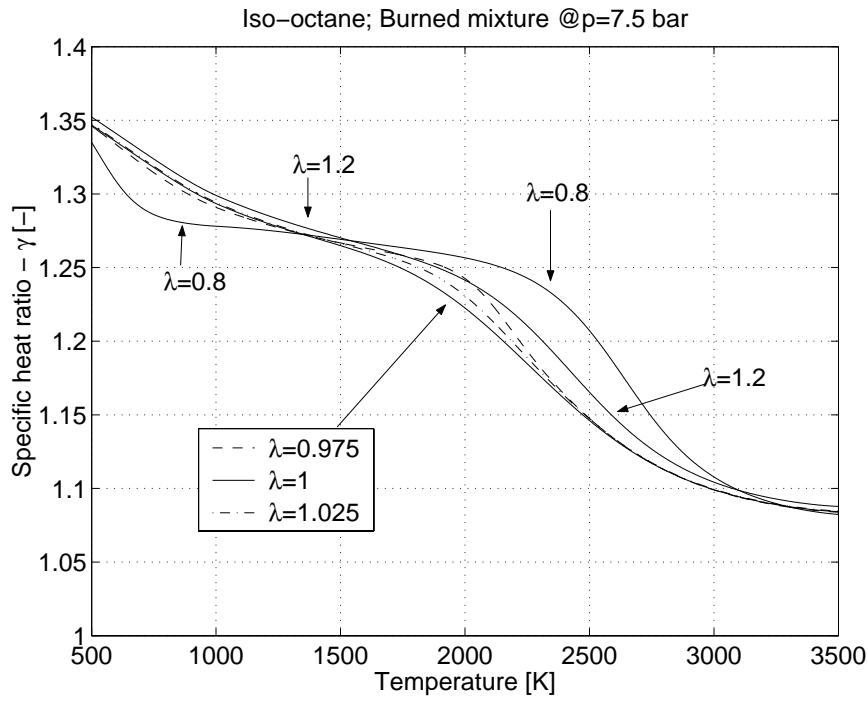


Figure 4.5: Specific heat ratio for burned mixture at various air-fuel ratios λ at 7.5 bar using CHEPP.

Region	$T \in$	γ_{300}	b
A	[500, 3500]	1.3695	$-9.6 \cdot 10^{-5}$
B	[500, 3000]	1.3726	$-9.9 \cdot 10^{-5}$
C	[500, 2700]	1.3678	$-9.4 \cdot 10^{-5}$
D	[500, 2500]	1.3623	$-8.8 \cdot 10^{-5}$
E	[1200, 3000]	1.4045	$-11.4 \cdot 10^{-5}$

Table 4.3: Coefficients in linear approximation $\gamma_{lin}^b(T)$ found in (4.2) for $\lambda = 1$ and $p = 7.5$ bar.

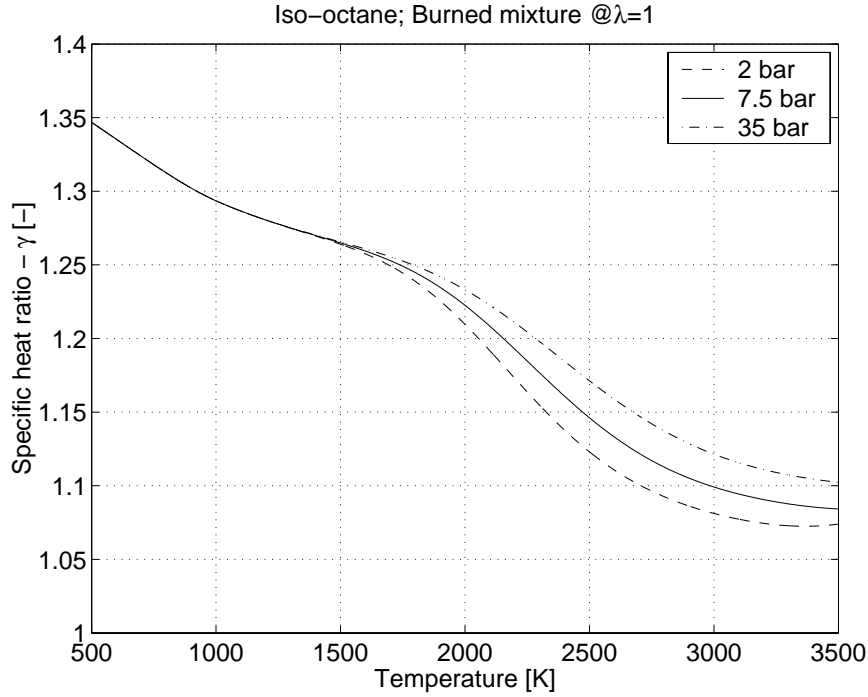


Figure 4.6: Specific heat ratio for burned stoichiometric mixture using CHEPP at various pressures.

Krieger-Borman polynomial is better than the linear approximation in every chosen temperature region, since the NRMSE is smaller. Comparing just the MRE:s could result in false conclusions. Take the temperature region A for instance, where the respective MRE are approximately the same. One could then conclude that the models describe γ equally well, but in figure 4.7 it was clearly visible that γ_{KB} is the better one, which is also the conclusion when comparing the respective NRMSE.

In table 4.5, the NRMSE and MRE for the Krieger-Borman polynomial $\gamma_{KB}(T, p, \lambda)$ for λ close to stoichiometric is displayed. For $\lambda \geq 1$ (lean), γ_{KB} fits the equilibrium γ better than for $\lambda < 1$, a tendency which is most evident when comparing the NRMSE for temperature region B. For temperature region A the difference for different λ is less striking, since the γ_{KB} does not fit γ as well for $T > 3000$ K. Therefore the Krieger-Borman polynomial is preferably only to be used on the lean side. On the rich side and close to stoichiometric (within 2.5 %), the Krieger-Borman polynomial does not introduce an error larger than the linear approximation given in table 4.4, and γ_{KB} should therefore be used in this operating range.

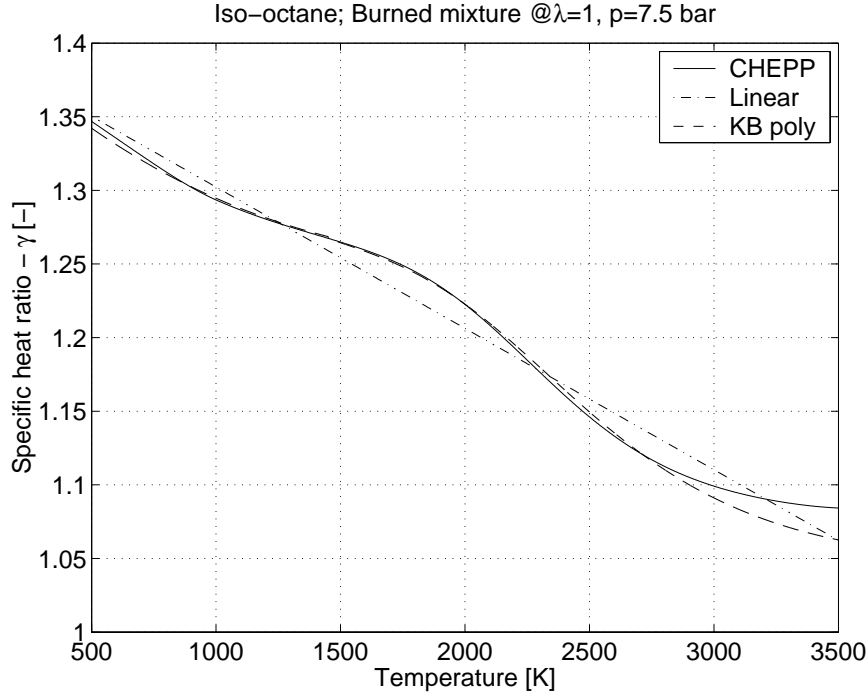


Figure 4.7: Specific heat ratio for burned stoichiometric mixture using CHEPP, the corresponding linear function γ_{lin}^b and Krieger-Bormans polynomial γ_{KB} .

Region	$T \in$	γ_{lin}^b		γ_{KB}	
		MRE	NRMSE	MRE	NRMSE
A	[500, 3500]	2.0 %	0.97 %	2.0 %	0.56 %
B	[500, 3000]	1.6 %	0.95 %	0.7 %	0.20 %
C	[500, 2700]	1.9 %	0.90 %	0.3 %	0.17 %
D	[500, 2500]	2.4 %	0.74 %	0.3 %	0.17 %
E	[1200, 3000]	1.6 %	0.74 %	0.7 %	0.21 %

Table 4.4: Maximum relative error (MRE) and normalized root mean square error (NRMSE) for different temperature regions at $\lambda = 1$ and $p = 7.5$ bar.

Region	$\gamma_{KB}@\lambda = 0.975$		$\gamma_{KB}@\lambda = 1$		$\gamma_{KB}@\lambda = 1.025$	
	MRE	NRMSE	MRE	NRMSE	MRE	NRMSE
A	1.9 %	0.86 %	2.0 %	0.56 %	2.1 %	0.59 %
B	1.8 %	0.73 %	0.7 %	0.20 %	0.7 %	0.28 %

Table 4.5: Maximum relative error (MRE) and normalized root mean square error (NRMSE) for different temperature regions for $\gamma_{KB}(T, p, \lambda)$ at $p = 7.5$ bar and $\lambda = \{0.975, 1, 1.025\}$

If a linear model of γ is preferred for computational reasons, the performance of the linear model could be enhanced by proper selection of temperature region. However, the MRE does not decrease for every reduction in interval, as seen when comparing MRE:s for regions D and B in table 4.4. Thus, the temperature region should be chosen with care by using the NRMSE as measure:

- When using the single-zone temperature T to describe the specific heat ratio of the burned mixture, temperature region B is preferable, since during the closed part $T \leq 3000$ K.
- When using the burned-zone temperature T_b in a two-zone model, temperature region E is recommended, since for most cases $T_b \in [1200, 3000]$. The temperature limits are found by evaluating a number of experimental cylinder pressure traces using (A.1) and (A.7). By choosing region E instead of region B, the NRMSE is reduced by 25%.

4.6 Partially burned mixture

The specific heat ratio γ as a function of mixture temperature T and air-fuel ratio λ for unburned and burned mixture of air and iso-octane has been investigated in the two previous sections. During the closed part of a motored engine cycle, the previous investigations would be enough since the models of the unburned mixture will be valid for the entire region. When considering firing cycles on the other hand, an assumption of either a purely unburned or a purely burned mixture approach is not valid for the entire combustion chamber during the closed part of the engine cycle.

To describe the specific heat ratio in the single-zone model for a partially burned mixture, the mass fraction burned trace x_b is used to interpolate the (mass-)specific heats of the unburned and burned zones to find the single-zone specific heats. The specific heat ratio is then found as the ratio between the interpolated specific heats.

4.6.1 Reference model

The single-zone specific heats are found from energy balance between the single-zone and the two-zone model, from which the single-zone specific heat ratio γ_{CE} can be stated:

$$c_p(T, p, x_b) = x_b c_{p,b}(T_b, p) + (1 - x_b) c_{p,u}(T_u) \quad (4.14a)$$

$$c_v(T, p, x_b) = x_b c_{v,b}(T_b, p) + (1 - x_b) c_{v,u}(T_u) \quad (4.14b)$$

$$\gamma_{CE}(T, p, x_b) = \frac{c_p(T, p, x_b)}{c_v(T, p, x_b)} \quad (4.14c)$$

where the mass fraction burned x_b is used as an interpolation variable. The single-zone (T), burned zone (T_b) and unburned zone (T_u) temperatures are given by the two temperatures models (A.1) and (A.7) described in appendix A.1. The first is the ordinary single-zone temperature model and the second is a two-zone mean temperature model developed by Andersson [2002]. The mass specific heats in (4.14) are computed using CHEPP [Eriksson, 2004] and γ_{CE} then forms the reference model.

To compute γ_{CE} is computationally heavy. Even when the specific heats are computed before-hand at a number of operating points, the computational burden is still heavy due to the numerous table look-ups and interpolations required. Therefore, a computationally more efficient model which retains accuracy is sought for. A number of γ -models will therefore be described in the following subsection, where they are divided into three subgroups based upon their modeling assumptions. These γ -models are then compared to the reference model γ_{CE} found from (4.14), in terms of four evaluation criteria, specified in the subsection ‘‘Evaluation criteria’’.

How to find x_b ?

To compute the specific heat ratio γ_{CE} (4.14), a mass fraction burned trace x_b is needed. For simulated pressure data, the mass fraction burned is considered to be known, which is the case in this work. However, if one were to use experimental data to e.g. do heat release analysis, x_b can not be considered to be known. There are then two ways of determining the mass fraction burned; The first is to use a simple and computationally efficient method to get x_b from a given cylinder pressure trace. Such methods were described in chapter 2 and include the pressure ratio management by Matekunas [1983] described in section 2.4. If one does not settle for this, the second approach is to initialize x_b using a simple method from the first approach, and then iteratively refine the mass fraction burned trace x_b using the computed heat release.

4.6.2 Grouping of γ -models

Twelve γ -models have been investigated and based upon their modeling assumptions, they are divided into three subgroups; The first group contains models for *burned mixture* only. The second contains models based on *interpolation of the specific heat ratios* directly, and the third group, to which (4.14) belongs, contains the models based on *interpolation of the specific heats*, from which the ratio is determined.

Group \mathcal{B} : Burned mixture

The first subgroup represents the in-cylinder mixture as a single zone of burned mixture with single-zone temperature T , computed by (A.1). The first model, denoted \mathcal{B}_1 , is the linear approximation in (4.2):

$$\mathcal{B}_1 : \gamma_{\mathcal{B}_1}(T) = \gamma_{lin}^b(T) = \gamma_{300} + b(T - 300) \quad (4.15)$$

where the coefficients can be determined in at least two ways; One way is to use the coefficients that are optimized for temperature region $T \in [500, 3000]$ (region B in Table 4.3) for a burned mixture. This approach is used in [Gatowski et al., 1984], although the coefficients differ somewhat compared to the ones given in Table 4.3. Another way is to optimize the coefficients from the reference model (4.14). This approach will be the one used here, since it yields the smallest modeling errors in both γ and cylinder pressure p . The approach has optimal conditions for the simulations, and will therefore give the best results possible for this model structure.

The second model, denoted \mathcal{B}_2 , is the Krieger-Borman polynomial described in (4.4)

$$\mathcal{B}_2 : u = A(T) - \frac{B(T)}{\lambda} \longrightarrow \gamma_{\mathcal{B}_2}(T) = \gamma_{KB}(T) \quad (4.16)$$

without the correction term for dissociation. The Krieger-Borman polynomial is used in model \mathcal{B}_3 as well,

$$\begin{aligned} \mathcal{B}_3 : u &= A(T) - \frac{B(T)}{\lambda} + u_{corr}(T, p, \lambda) \\ &\longrightarrow \gamma_{\mathcal{B}_3}(T, p) = \gamma_{KB}(T, p) \end{aligned} \quad (4.17)$$

with the correction term $u_{corr}(T, p, \lambda)$ for dissociation included. The fourth and simplest model uses a constant γ :

$$\mathcal{B}_4 : \gamma_{\mathcal{B}_4} = \text{constant} \quad (4.18)$$

As for model \mathcal{B}_1 , the coefficient in (4.18) is determined from the reference model (4.14).

Group \mathcal{C} : Interpolation of specific heat ratios

The second subgroup uses a two-zone model, i.e. a burned and an unburned zone, and calculates the specific heat ratio $\gamma_b(T_b)$ and $\gamma_u(T_u)$ for each zone respectively, where the temperatures are given by the two-zone mean temperature model (A.7). The mass fraction burned trace x_b is then used to find the single-zone γ by interpolating γ_b and γ_u . Note that the energy balance equation, used in (4.14), is not fulfilled for subgroup \mathcal{C} .

The first model, denoted \mathcal{C}_1 , interpolates linear approximations of γ for the unburned and burned mixture. The linear functions are optimized in temperature region $T \in [300, 1000]$ for the unburned mixture, and temperature region $T \in [1200, 3000]$ for the burned mixture. The resulting $\gamma_{\mathcal{C}_1}$ can therefore be written as:

$$\mathcal{C}_1 : \gamma_{\mathcal{C}_1}(T, x_b) = x_b \gamma_{lin}^b(T_b) + (1 - x_b) \gamma_{lin}^u(T_u) \quad (4.19)$$

where the coefficients for the linear functions are given in Table 4.3 and Table 4.2 respectively.

The second model was proposed in [Stone, 1999, p.423], here denoted \mathcal{C}_2 , and is based on interpolation of the internal energy u computed from the Krieger-Borman polynomial:

$$\mathcal{C}_2 : u = A(T) - x_b \frac{B(T)}{\lambda} \longrightarrow \gamma_{\mathcal{C}_2}(T, x_b) \quad (4.20)$$

This model includes neither dissociation nor the internal energy of the unburned mixture.

An improvement of model \mathcal{C}_1 is expected when substituting the linear model for the burned mixture with the Krieger-Borman polynomial. This new model is denoted \mathcal{C}_3 and described by:

$$\mathcal{C}_3 : \gamma_{\mathcal{C}_3}(T, p, x_b) = x_b \gamma_{KB}(T_b, p) + (1 - x_b) \gamma_{lin}^u(T_u) \quad (4.21)$$

The fourth model interpolates $\gamma_u(T_u)$ and $\gamma_b(T_b, p)$ given by CHEPP:

$$\mathcal{C}_4 : \gamma_{\mathcal{C}_4}(T, p, x_b) = x_b \gamma_b(T_b, p) + (1 - x_b) \gamma_u(T_u) \quad (4.22)$$

and this model is denoted \mathcal{C}_4 . This model will reflect the modeling error introduced by interpolating the specific heat ratios directly instead of using the definition through the specific heats (4.14).

The segmented linear model (4.3) developed by Chun and Heywood [1987] is also investigated and here denoted by model \mathcal{C}_5 :

$$\mathcal{C}_5 : \gamma_{\mathcal{C}_5}(T, x_b) = \gamma_{seg}(T, x_b) = \begin{cases} \gamma_{300}^{comp} + b^{comp}(T - 300) & x_b < 0.01 \\ \gamma_{300}^{comb} & 0.01 \leq x_b \leq 0.99 \\ \gamma_{300}^{exp} + b^{exp}(T - 300) & x_b > 0.99 \end{cases} \quad (4.23)$$

Model \mathcal{C}_5 uses the single-zone temperature for each phase, and classifies into group \mathcal{C} due to that the switching used for x_b in (4.23) can be seen as a nearest neighbor interpolation. As for model \mathcal{B}_1 and \mathcal{B}_4 , the coefficients in (4.23) are determined from the reference model (4.14).

Group \mathcal{D} : Interpolation of specific heats

The last subgroup uses a two-zone model, i.e. a burned and an unburned zone, just as the second subgroup, and the specific heats are interpolated to get the single-zone specific heats. The first model, denoted \mathcal{D}_1 , uses the Krieger-Borman polynomial for the burned zone to find $c_{p,b}(T_b, p)$ and $c_{v,b}(T_b, p)$, and the linear approximations of $c_{p,u}(T_u)$ and $c_{v,u}(T_u)$ given in Table 4.2 for the unburned zone:

$$\mathcal{D}_1 : \gamma_{\mathcal{D}_1}(T, p, x_b) = \frac{x_b c_{p,b}^{KB}(T_b, p) + (1 - x_b) c_{p,u}^{lin}(T_u)}{x_b c_{v,b}^{KB}(T_b, p) + (1 - x_b) c_{v,u}^{lin}(T_u)} \quad (4.24)$$

An extension of model \mathcal{D}_1 is to use the unburned specific heats $c_{p,u}(T_u)$ and $c_{v,u}(T_u)$ computed from CHEPP:

$$\mathcal{D}_2 : \gamma_{\mathcal{D}_2}(T, p, x_b) = \frac{x_b c_{p,b}^{KB}(T_b, p) + (1 - x_b) c_{p,u}(T_u)}{x_b c_{v,b}^{KB}(T_b, p) + (1 - x_b) c_{v,u}(T_u)} \quad (4.25)$$

This model is denoted \mathcal{D}_2 and reflects the model error introduced by using the linear approximation of the unburned mixture specific heats, when comparing to \mathcal{D}_1 .

Model \mathcal{D}_1 is also extended for the burned mixture, where the specific heats for the burned mixture $c_{p,b}(T_b, p)$ and $c_{v,b}(T_b, p)$ are computed using CHEPP. This model is denoted \mathcal{D}_3 :

$$\mathcal{D}_3 : \gamma_{\mathcal{D}_3}(T, p, x_b) = \frac{x_b c_{p,b}(T_b, p) + (1 - x_b) c_{p,u}^{lin}(T_u)}{x_b c_{v,b}(T_b, p) + (1 - x_b) c_{v,u}^{lin}(T_u)} \quad (4.26)$$

and reflects the model error introduced by using the Krieger-Borman approximation of the specific heats, when comparing to \mathcal{D}_1 .

The reference model γ_{CE} (4.14) belongs to this group and is denoted \mathcal{D}_4 :

$$\mathcal{D}_4 : \gamma_{\mathcal{D}_4}(T, p, x_b) = \gamma_{CE}(T, p, x_b) \quad (4.27)$$

4.6.3 Evaluation criteria

The different γ -models given by (4.15)-(4.26) are evaluated in terms of four criteria. The criteria are:

1. Normalized root mean square error (NRMSE) in γ , which gives a measure of the mean error in γ .
2. Maximum relative error (MRE) for γ , which yields a measure of the maximum error in γ .
3. Root mean square error (RMSE) for the corresponding cylinder pressures. This measure will give a measure of the impact that a certain model error has on the cylinder pressure and will help to find a γ -model accurate enough for the single-zone model.

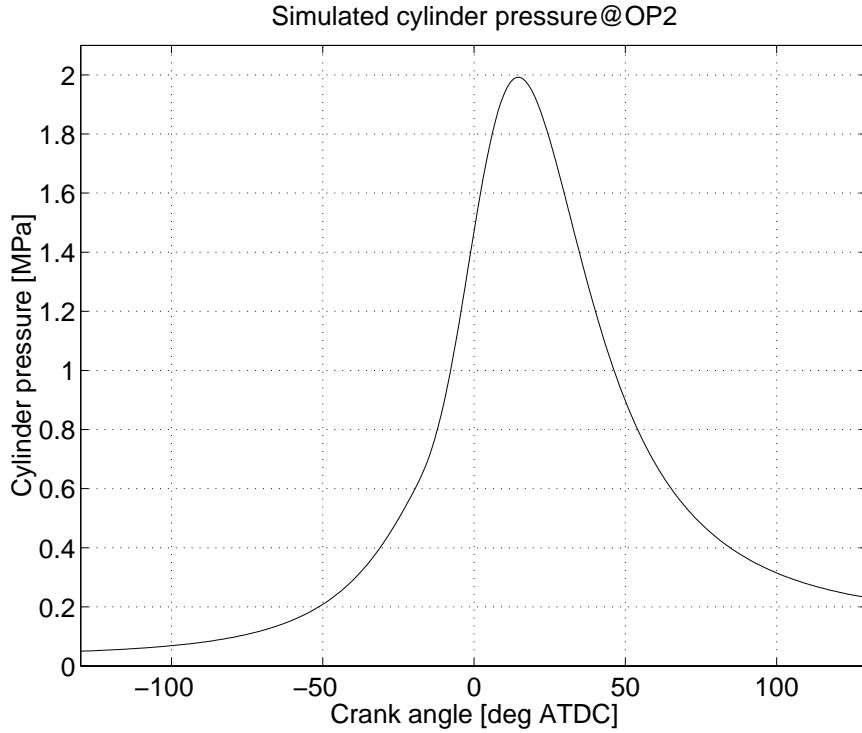


Figure 4.8: Simulated cylinder pressure using Gatowski et al.-model with nominal values in table 3.2, and the linear γ -model \mathcal{B}_1 replaced by reference model \mathcal{D}_4 .

4. The computational efficiency is also evaluated by comparing the required simulation time of the cylinder pressure given a burn rate trace and a specific γ -model.

4.6.4 Evaluation covering one operating point

At first, only one operating point is considered. This operating point is given by the parameter values in table 3.2, except for Q_{in} which now is 760 J, and corresponds to the cylinder pressure given in figure 4.8, i.e. at low engine load conditions. The cylinder pressure given in figure 4.8 is used as an example that illustrates the effect that each model has on specific heat ratio γ and cylinder pressure. To investigate if the engine operating condition influences the choice of model, nine operating points covering most parts of the operating range of an engine are used to do the same evaluations. These operating points are given in table A.7 and their corresponding cylinder pressures are displayed in figure A.6,

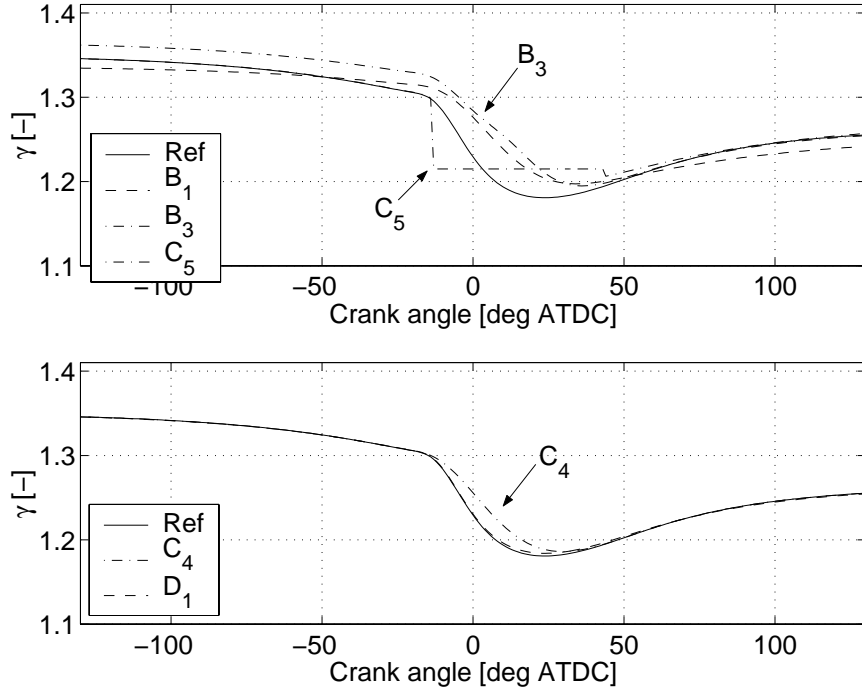


Figure 4.9: *Upper:* Specific heat ratios for models B_1 , B_3 and C_5 as compared to the reference model D_4 . *Lower:* Specific heat ratios for models C_4 and D_1 as compared to the reference model D_4 .

where operating point 2 corresponds to the cylinder pressure in figure 4.8.

γ -domain

The γ -models in the three subgroups are compared to the reference model γ_{CE} (4.14). A summary of the results are given here while a complete picture is given in appendix A.7, see e.g. figures A.7 and A.8, where γ is plotted as a function of crank angle. In those figures, the reference model γ_{CE} is the dashed line and the solid line corresponds to each specific model. The specific heat ratio for each model is also given in figure A.9 and figure A.10 as a function of single-zone temperature T . Figure 4.9 compares the reference model D_4 with the computed values of γ for a few of these models, namely B_1 , B_3 , C_5 , C_4 and D_1 .

Of these models, only model D_1 (4.24) is able to capture the reference model well. This is confirmed by the $MRE(\gamma)$ and $NRMSE(\gamma)$ columns in table 4.6, where only model group D yields errors lower than 1% for both columns. Model C_4 deviates only during the combustion, which in this case occurs for $\theta \in [-15, 40]$ deg ATDC. This deviation is enough to yield a $NRMSE(\gamma)$ which

Model	MRE: γ [%]	RMSE: p [kPa]	NRMSE: γ [%]	Time [s]
\mathcal{B}_1 (4.15)	4.7	52.3	1.3	3.8
\mathcal{B}_2 (4.16)	5.9	85.8	2.7	4.1
\mathcal{B}_3 (4.17)	5.2	76.0	1.8	4.2
\mathcal{B}_4 (4.18)	7.7	62.8	4.5	3.8
\mathcal{C}_1 (4.19)	2.3	39.8	0.69	4.7
\mathcal{C}_2 (4.20)	7.3	140.7	4.1	4.9
\mathcal{C}_3 (4.21)	2.4	25.4	0.65	5.1
\mathcal{C}_4 (4.22)	2.3	22.8	0.58	211.1
\mathcal{C}_5 (4.23)	8.4	82.9	1.5	4.0
\mathcal{D}_1 (4.24)	0.27	2.8	0.10	5.2
\mathcal{D}_2 (4.25)	0.26	2.6	0.09	12.3
\mathcal{D}_3 (4.26)	0.04	0.3	0.01	381.9
\mathcal{D}_4 (4.14)	0.0	0.0	0.0	384.2

Table 4.6: Evaluation of γ -models, on the single cycle shown in figure 4.8.

is almost 0.6 %, approximately six times that found for \mathcal{D}_1 .

Of the models previously proposed in literature, the linear model \mathcal{B}_1 (4.15) has the best performance, although it does not capture the reference model very well, as seen in the upper plot of figure 4.9. Model \mathcal{B}_3 (4.17) is only able to capture the reference model after the combustion, since model \mathcal{B}_3 is optimized for a burned mixture. Model \mathcal{C}_5 (4.23) has good behavior before and after the combustion. But during the combustion, the constant γ_{300}^{comb} does not capture γ_{CE} very well. Models \mathcal{B}_4 and \mathcal{C}_2 has even worse behavior, as shown in figure A.7.

To conclude, model group \mathcal{D} yields errors in γ which are less than 1% for this operating point. Of these models, model \mathcal{D}_3 has the best performance compared to the reference model \mathcal{D}_4 .

Pressure domain

The impact that the γ -models have on the corresponding cylinder pressure is shown in figure 4.10 for models \mathcal{B}_1 , \mathcal{B}_3 , \mathcal{C}_5 , \mathcal{C}_4 and \mathcal{D}_1 , and for all models in figures A.11 and A.12. The plots show the difference between the simulated cylinder pressure for reference model \mathcal{D}_4 and the γ -models, i.e. the cylinder pressure error induced by the modeling error in γ . Note that the scaling in the figures are different. The cylinder pressure model used for the simulations is the model developed by Gatowski et al. [1984]. Section 2.5 gives the model equations and appendix A.2 gives more details about the implementation used here.

The RMSE of the measurement noise is approximately 6 kPa and it is only model group \mathcal{D} that introduces a modeling error in the same order as the noise

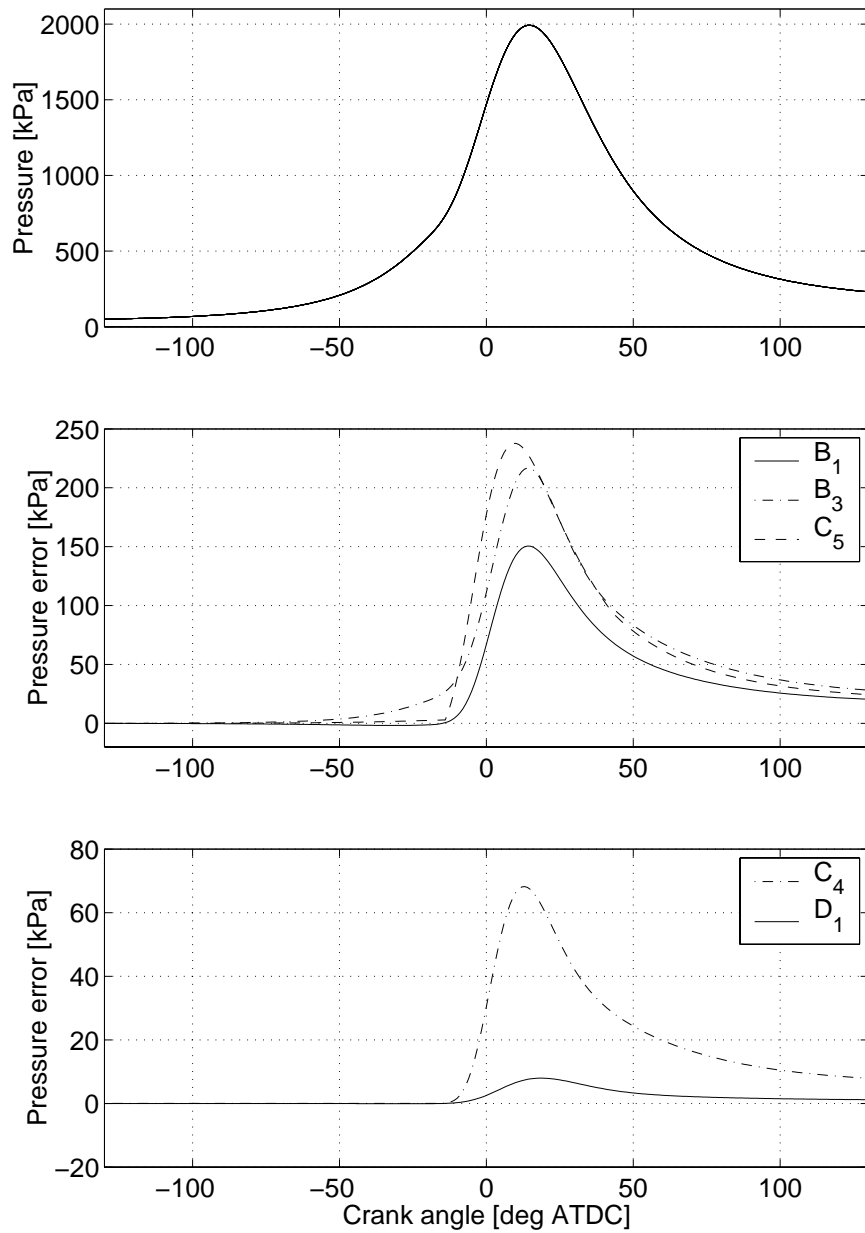


Figure 4.10: *Upper:* Reference cylinder pressure, the same as given in figure 4.8. *Middle:* Cylinder pressure error introduced by models B_1 , B_3 and C_5 . For convenience, the sign for C_5 is changed. *Lower:* Cylinder pressure error introduced by models C_4 and D_1 . Note that the scaling in the plots are different.

in terms of RMSE. Thus, the other γ -models will introduce a modeling error which is significantly larger than the measurement noise as seen in Table 4.6, and thereby affect the accuracy of the parameter estimates. Within group \mathcal{D} , models \mathcal{D}_3 and \mathcal{D}_4 have the smallest RMSE(p), and therefore yield the highest accuracy. Model \mathcal{D}_1 does not introduce a significantly larger RMSE(p) than \mathcal{D}_2 , and therefore the most time efficient one should be used of these two. Altogether this suggests that any model in group \mathcal{D} could be used.

The previously proposed γ -models \mathcal{B}_1 , \mathcal{B}_2 , \mathcal{B}_3 , \mathcal{B}_4 and \mathcal{C}_5 , described in section 4.2, all introduce modeling errors which are at least seven times the measurement noise for this operating point. Clearly, a large error, so none of these models are recommended. Of these models, \mathcal{B}_1 induces the smallest RMSE(p) and should, if any, be the one used of the previously proposed models.

A note on crevice volume modeling

Note that the usage of a γ -model different from the linear model used in Gatowski et al. [1984], will also affect the amount of energy left or added to the system when a mass element enters or leaves the crevice volume. This energy $u' - u = \int_T^{T'} c_v dT$ is quantified by (2.30) for \mathcal{B}_1 , and has been given in (2.31) for a γ -model polynomial of order n . This energy term has to be restated for every γ -model at hand except model \mathcal{B}_1 , and this is done for model \mathcal{D}_1 in appendix A.5.

Computational time

The right-most column of table 4.6 shows the computational time. The time value given is the mean time for simulating the closed part of one engine cycle using Matlab 6.1 on a SunBlade 100, which has a 64-bit 500 MHz processor. The proposed model \mathcal{D}_1 is approximately 70 times faster than the reference model \mathcal{D}_4 , where the reference model uses look-up tables for precomputed values of the specific heats c_p and c_v . Introducing the model improvement in model \mathcal{D}_1 of the specific heat ratio to the Gatowski et al. single-zone heat release model is simple, and it does not increase the computational burden immensely compared to the original setting, i.e. \mathcal{B}_1 . The increase in computational effort is less than 40 % compared to the linear γ -model when simulating the Gatowski et al. single-zone heat release model.

4.6.5 Evaluation covering all operating points

The same analysis as above has been made for the simulated cylinder pressure from nine different operating points, where $p_{IVC} \in [0.25, 2]$ bar and $T_{IVC} \in [325, 372]$ K. The parameters for each cycle is given in table A.7 as well as the corresponding cylinder pressures in figure A.6. The operating range in p and T that these cycles cover is given in figure 4.11, where the upper plot shows the range covered for the unburned mixture, and the lower shows the range covered

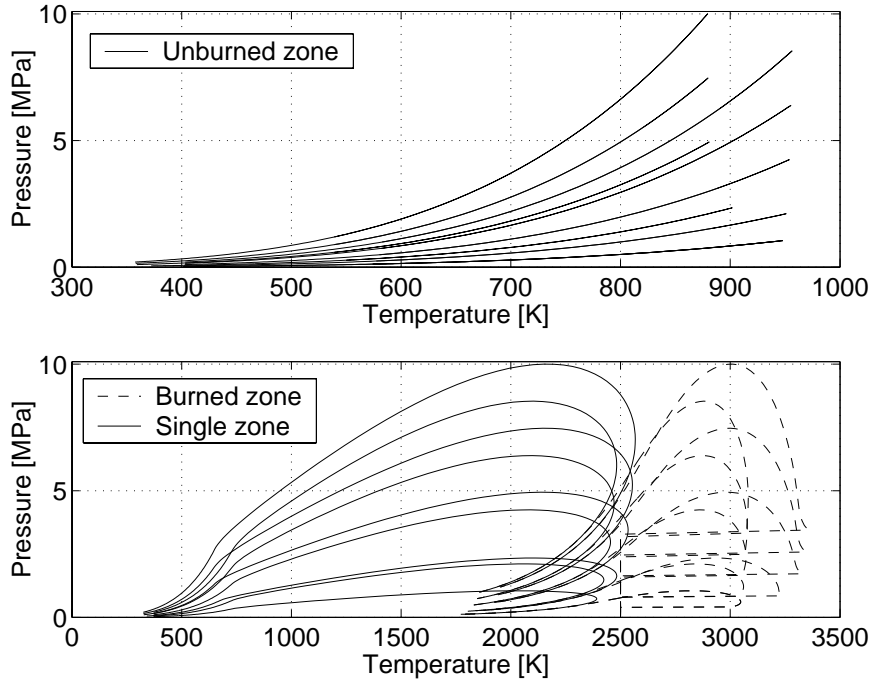


Figure 4.11: Operating range in p and T . *Upper:* Unburned zone. *Lower:* Single zone (solid) and burned zone (dashed).

for single-zone (solid) and burned (dashed) mixture. According to [Heywood, 1988, p.109], the temperature region of interest for an SI engine is 400 to 900 K for the unburned mixture; for the burned mixture, the extreme end states are approximately $\{1200 \text{ K}, 0.2 \text{ MPa}\}$ and $\{2800 \text{ K}, 3.5 \text{ MPa}\}$. Of course, not all points in the range are covered but the cycles at hand cover the extremes of the range of interest.

The results are summarized in terms of NRMSE for γ (table A.8), RMSE for p in table A.9 and MRE for γ in table A.10, where the mean values over the operating points for each model and the values for each cycle are given. The mean values for each model are also given here as a summary in table 4.7.

Ordering of models

When comparing the NRMSE for γ in table 4.7, the ordering of the γ -models, where the best one comes first, is:

$$\mathcal{D}_4 \prec \mathcal{D}_3 \prec \mathcal{D}_2 \prec \mathcal{D}_1 \prec \mathcal{C}_4 \prec \mathcal{C}_3 \prec \mathcal{C}_1 \prec \mathcal{B}_1 \prec \mathcal{C}_5 \prec \mathcal{B}_3 \prec \mathcal{B}_2 \prec \mathcal{C}_2 \prec \mathcal{B}_4 \quad (4.28)$$

Model	MRE: γ [%]	RMSE: p [kPa]	NRMSE: γ [%]
\mathcal{B}_1	3.4	84.9	1.2
\mathcal{B}_2	5.2	153.6	2.4
\mathcal{B}_3	4.5	137.3	1.7
\mathcal{B}_4	7.1	110.0	4.2
\mathcal{C}_1	1.9	56.6	0.77
\mathcal{C}_2	6.6	269.2	3.9
\mathcal{C}_3	1.9	42.4	0.53
\mathcal{C}_4	1.8	36.7	0.46
\mathcal{C}_5	8.3	191.9	1.6
\mathcal{D}_1	0.26	5.8	0.097
\mathcal{D}_2	0.25	5.1	0.092
\mathcal{D}_3	0.044	0.7	0.016

Table 4.7: Evaluation of γ -models, in terms of the mean values for all operating points in table A.7.

Here $\mathcal{B}_2 \prec \mathcal{C}_2$ means that model \mathcal{B}_2 is better than \mathcal{C}_2 . Comparing RMSE for the cylinder pressure p , the ordering of the γ -models becomes:

$$\mathcal{D}_4 \prec \mathcal{D}_3 \prec \mathcal{D}_2 \prec \mathcal{D}_1 \prec \mathcal{C}_4 \prec \mathcal{C}_3 \prec \mathcal{C}_1 \prec \mathcal{B}_1 \prec \mathcal{B}_4 \prec \mathcal{B}_3 \prec \mathcal{B}_2 \prec \mathcal{C}_5 \prec \mathcal{C}_2 \quad (4.29)$$

This ordering is not the same as in (4.28), but the only difference lies in models \mathcal{C}_5 and \mathcal{B}_4 . Model \mathcal{C}_5 has poor performance in terms of $\text{RMSE}(p)$, compared to $\text{NRMSE}(\gamma)$. For model \mathcal{B}_4 , it is the other way around.

Model group \mathcal{D}

In terms of $\text{NRMSE}(\gamma)$ (4.28) and $\text{RMSE}(p)$ (4.29) model group \mathcal{D} behaves as expected, and obeys the rule: the higher the complexity is, the higher the accuracy becomes. According to the $\text{RMSE}(p)$ column in table 4.7, the models in \mathcal{D} all introduce an $\text{RMSE}(p)$ which is less than that found for the measurement noise. Comparing models \mathcal{D}_1 (4.24) and \mathcal{D}_2 (4.25), it is obvious that not much is gained in accuracy by using the unburned specific heats from CHEPP instead of the linear functions. The computational cost for \mathcal{D}_2 was more than two times the one for \mathcal{D}_1 , as shown in table 4.6. This suggests that the unburned specific heats are sufficiently well described by the linear approximation. Model \mathcal{D}_3 (4.26) utilizes the burned specific heat from CHEPP, and this is an improvement compared to model \mathcal{D}_1 which uses the Krieger-Borman polynomial for $c_{p,b}$ and $c_{v,b}$. This improvement reduces the $\text{RMSE}(p)$ with a factor 7, but the cost in computational time is high, approximately a factor 70 according to table 4.6. This is considered to be a too high cost at the moment. The comparison also shows that if we want to reduce the impact on the cylinder pressure, the effort

should be to increase the accuracy of the Krieger-Borman polynomial for the burned mixture. In figures A.4 and A.5, see appendix A.6, the specific heats for CHEPP and the Krieger-Borman polynomial are given, and this verifies that the polynomial has poorer performance for higher temperatures. A new polynomial for the burned mixture, valid for a smaller but more relevant region for SI engines could increase the accuracy. This is however left as future work for the moment, and in the meanwhile model \mathcal{D}_1 is recommended as a good compromise between computational accuracy and efficiency.

Model group \mathcal{C}

In model group \mathcal{C} , model \mathcal{C}_5 has good performance when considering the NRMSE in γ (4.28), but not as good in $\text{RMSE}(p)$ (4.29). This perhaps explains why Chun and Heywood [1987] consider this to be a good and accurate enough model for single-zone models. This illustrates the importance of evaluating the modeling error in the γ -domain to the cylinder pressure domain, and it also reflects that $\text{RMSE}(p)$ is the more important model performance measure of the two. Model \mathcal{C}_2 [Stone, 1999, p.423] has really bad performance and would be the last choice here. The rest of the models in group \mathcal{C} obeys the same rule as group \mathcal{D} , i.e. $\mathcal{C}_4 \prec \mathcal{C}_3 \prec \mathcal{C}_1$.

When the best model in group \mathcal{C} , i.e. \mathcal{C}_4 , is compared to all models in group \mathcal{D} , and especially the reference model \mathcal{D}_4 , it is concluded that the specific heats should be interpolated, and not the specific heat ratios. This conclusion can be drawn since the only difference between \mathcal{C}_4 and \mathcal{D}_4 is how the interpolation is performed. Model \mathcal{C}_4 interpolates the specific heat ratios found from CHEPP directly, and model \mathcal{D}_4 interpolates the specific heats from CHEPP and then form the specific heat ratio. Therefore, group \mathcal{D} has better performance than group \mathcal{C} . Since \mathcal{D}_1 has higher accuracy and approximately the same computational time as all models in group \mathcal{C} , there is no point in using any of the models in group \mathcal{C} .

Model group \mathcal{B}

As expected, the models in group \mathcal{B} has the worst performance of them all, if excluding models \mathcal{C}_2 and \mathcal{C}_5 . It is interesting to note that the linear model γ_{lin}^b (\mathcal{B}_1) performs best in the group, although it introduces a modeling error in p which is at least ten times the measurement noise in the mean. It has better performance than γ_{KB} (\mathcal{B}_3) in the pressure domain, although this is not the case in the γ -domain. This again points out the necessity of evaluating the impact of the γ -model on to the cylinder pressure. Therefore, if the assumption is that the cylinder contents should be treated as a burned mixture during the entire closed part of the engine cycle, \mathcal{B}_1 is the model to use.

Summary

To conclude, the models are ordered by their performance and with computational efficiency in ascending order:

$$\mathcal{D}_4 \prec \mathcal{D}_1 \prec \mathcal{B}_1 \prec \mathcal{B}_4 \quad (4.30)$$

Some of the models are excluded from this list, either due to their low accuracy, high computational time, or because another model with approximately the same computational time has higher accuracy. Of the models given in (4.30), \mathcal{D}_1 is recommended as a compromise between computational time and accuracy. Compared to the original setting in Gatowski et al. [1984], the computational burden increases with 40 % and the modeling error is more than ten times smaller in the mean. This also stresses that the γ -model is an important part of the heat release model, since it has a large impact on the cylinder pressure. The focus is now turned to how the γ -models will affect the heat release parameters.

4.6.6 Influence of γ -models on heat release parameters

The question is: What impact does each of the proposed γ -models have on the heat release parameters? This is investigated by using the cylinder pressure for operating point 2, given in figure 4.8, and estimate the three heat release parameters θ_d , θ_b and Q_{in} in the Vibe function, introduced in appendix A.3. The cylinder pressure is simulated using reference model \mathcal{D}_2 in conjunction with the Gatowski et al. cylinder pressure model, and this forms the cylinder pressure measurement signal to which measurement noise is added.

The heat release trace is then estimated given the measurement from reference model \mathcal{D}_2 . The heat release trace is parameterized by the Vibe function, which has the heat release parameters θ_d , θ_b and Q_{in} . The estimation is performed by minimizing the prediction error, i.e. by minimizing the difference between the measured cylinder pressure and the modeled cylinder pressure. The Levenberg-Marquardt method described in appendix B.3 is used as optimization algorithm. The heat release parameters are then estimated for each of the γ -models using the Gatowski et al.-model, where the γ -model is replaced in an obvious manner in the equations. In the estimations, only the three heat release parameters are estimated. The other parameters are set to their true values given in table 3.2. The results are summarized in table 4.8, which displays the relative estimation error (RE) and the relative 95 % confidence interval (RCI) in θ_d , θ_b and Q_{in} respectively for each γ -model. The computational time and $\text{RMSE}(p)$ are also given.

Discussion

The RMSE of the applied measurement noise is approximately 6.7 kPa, which is also the RMSE found when using most γ -models. All methods are able to estimate the rapid burn angle θ_b most accurately of the three, and almost all

Model	θ_d [%]		θ_b [%]		Q_{in} [%]		RMSE(p) [kPa]	Time [min]
	RE	RCI	RE	RCI	RE	RCI		
\mathcal{B}_1	5.1	1.7	0.29	3.1	-9.2	1.4	9.8	3.5
\mathcal{B}_2	3.1	1.7	0.63	2.9	-7.3	1.3	9.1	3.8
\mathcal{B}_3	3.4	1.7	-0.2	2.9	-7.2	1.3	9.1	3.9
\mathcal{B}_4	6.8	1.7	-0.11	3.2	-6.2	1.4	10.1	3.5
\mathcal{C}_1	0.074	1.4	1.1	2.4	-2.9	1.1	6.5	4.4
\mathcal{C}_2	9.6	2.1	-1	3.9	-14	1.7	16.0	4.6
\mathcal{C}_3	0.19	1.4	0.75	2.4	-2.5	1.2	6.5	4.8
\mathcal{C}_4	0.14	1.5	0.64	2.4	-2	1.2	6.7	200
\mathcal{C}_5	-8	1.5	-2.5	2.3	27	0.92	6.6	3.7
\mathcal{D}_1	0.21	1.5	-0.062	2.4	-0.67	1.3	6.7	4.9
\mathcal{D}_2	0.2	1.5	-0.08	2.4	-0.61	1.3	6.7	11
\mathcal{D}_3	0.22	1.5	-0.13	2.4	-0.48	1.3	6.7	360
\mathcal{D}_4	0.21	1.5	-0.13	2.4	-0.42	1.3	6.7	360

Table 4.8: Relative estimation error (RE) and relative 95 % confidence interval (RCI) given in per cent, for heat release parameters using various γ -models at operating point 2. The nominal values for the heat release parameters are: $\theta_d = 15$ deg, $\theta_b = 30$ deg and $Q_{in} = 760$ J. The computational time and cylinder pressure RMSE are also given.

of them are accurate within 1%. On the other hand, only model group \mathcal{D} is accurate within 1 % for all three parameters, and this suggests that any of the \mathcal{D} -models can be used, preferably model \mathcal{D}_1 due to its lower computational time. Note also that \mathcal{C}_5 gives the highest deviation in the estimates of them all.

4.6.7 Influence of air-fuel ratio λ

An investigation is performed here to see how the proposed model \mathcal{D}_1 behaves for different air-fuel ratios λ . The $\text{NRMSE}(\gamma; \mathcal{D}_1, \lambda)$ and $\text{RMSE}(p; \mathcal{D}_1, \lambda)$ are computed for model \mathcal{D}_1 (4.24) compared to reference model \mathcal{D}_4 for the air-fuel ratio region $\lambda \in [0.975, 1.025]$, at operating point 2. It is assumed that the λ -controller of the SI engine has good performance, and therefore keeps the variations in λ small. The results are displayed in figure 4.12, where the upper plot shows the $\text{NRMSE}(\gamma; \mathcal{D}_1, \lambda)$, and the lower plot shows the $\text{RMSE}(p; \mathcal{D}_1, \lambda)$. Lean and stoichiometric mixtures have the lowest errors in the γ domain, which is expected since the Krieger-Borman polynomial for the burned mixture is estimated for lean mixtures. The error in pressure domain is approximately symmetric around $\lambda = 0.995$, and the magnitude is still less than the measurement noise. This assures that for a few per cent deviation in λ from stoichiometric conditions, the introduced error is still small and acceptable.

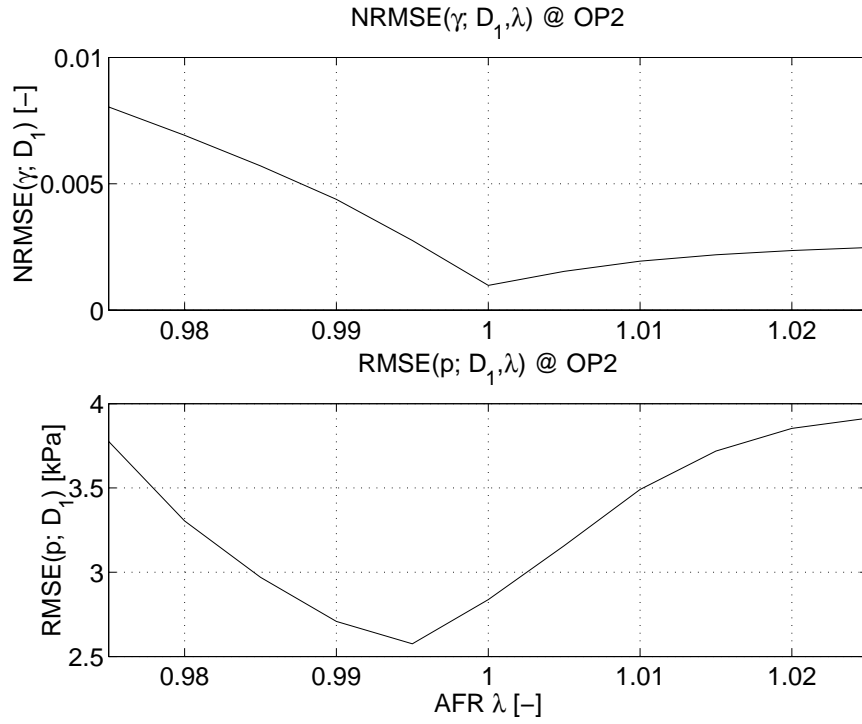


Figure 4.12: *Upper:* $\text{NRMSE}(\gamma; \mathcal{D}_1, \lambda)$ for $\lambda \in [0.975, 1.025]$. *Lower:* $\text{RMSE}(p; \mathcal{D}_1, \lambda)$ for $\lambda \in [0.975, 1.025]$.

A note on fuel composition

A small, and by no means exhaustive sensitivity analysis is made for fuels such as methane and two commercial fuels in appendix A.4. This in order to see if the results are valid for other fuels than iso-octane. The carbonhydrogen ratio for the fuel $C_a H_b$ is given by $y = b/a$. It is found that the hydrocarbon ratio needs to be close to 2.25, i.e. the one for iso-octane, although an exact limit can not be given without further studies. For a commercial fuel with ratio $y = 1.88$, the $\text{RMSE}(p)$ introduced is increased with less than 75 % compared to iso-octane, which is acceptable.

4.6.8 Influence of residual gas

The influence of the residual gas on the specific heat ratio has so far been neglected. Introducing the residual gas mass fraction x_r , the single-zone specific

heat ratio γ_{CE} in (4.14) is reformulated as:

$$c_p(T, p, x_b, x_r) = x_b c_{p,b}(T_b, p) + (1 - x_b) ((1 - x_r) c_{p,u}(T_u) + x_r c_{p,b}(T_u, p)) \quad (4.31a)$$

$$c_v(T, p, x_b, x_r) = x_b c_{v,b}(T_b, p) + (1 - x_b) ((1 - x_r) c_{v,u}(T_u) + x_r c_{v,b}(T_u, p)) \quad (4.31b)$$

$$\gamma_{CE}(T, p, x_b, x_r) = \frac{c_p(T, p, x_b, x_r)}{c_v(T, p, x_b, x_r)} \quad (4.31c)$$

where the model assumptions are:

- the residual gas is homogeneously distributed throughout the combustion chamber
- the residual gas is described by a burned mixture at the appropriate temperature and pressure
- a residual gas mass element in the unburned zone assumes the unburned zone temperature T_u
- when a residual gas mass element crosses the flame front, it enters the burned zone and assumes the burned zone temperature T_b . The pressure is assumed to be homogeneous throughout all zones.

In figure 4.13, the specific heat ratio γ_{CE} is computed according to (4.31) for residual gas fractions $x_r = [0, 0.05, 0.1, 0.15, 0.20]$ given the cylinder pressure in figure 4.8. It shows that the larger the residual gas fraction, the larger the γ .

The difference in γ for $x_r = [0.05, 0.1, 0.15, 0.20]$ compared to $x_r = 0$ is shown in figure 4.14. The difference is largest during compression and combustion. After the combustion, the mass specific heats for the single zone will coincide with the ones for the burned zone in accordance with the model assumptions, and there is thus no difference in γ .

Modeling of x_r -dependence

A simple model of the influence of x_r on γ is to model the influence as a linear function of x_r during the closed part, i.e.

$$\gamma(T, p, x_b, x_r) = \gamma_{CE}(T, p, x_b) + b_{x_r} x_r = \gamma_{CE}(T, p, x_b) + \gamma_{bias}(x_r) \quad (4.32)$$

where $\gamma_{CE}(T, p, x_b)$ is given by (4.14). Since x_r is constant during a cycle, the term $b_{x_r} x_r$ can be considered as a constant bias $\gamma_{bias}(x_r)$ that changes from cycle to cycle. A better model is gained if the mass fraction burned x_b is used, as described in

$$\gamma(T, p, x_b, x_r) = \gamma_{CE}(T, p, x_b) + (1 - x_b) b_{x_r} x_r = \gamma_{CE}(T, p, x_b) + (1 - x_b) \gamma_{bias}(x_r) \quad (4.33)$$

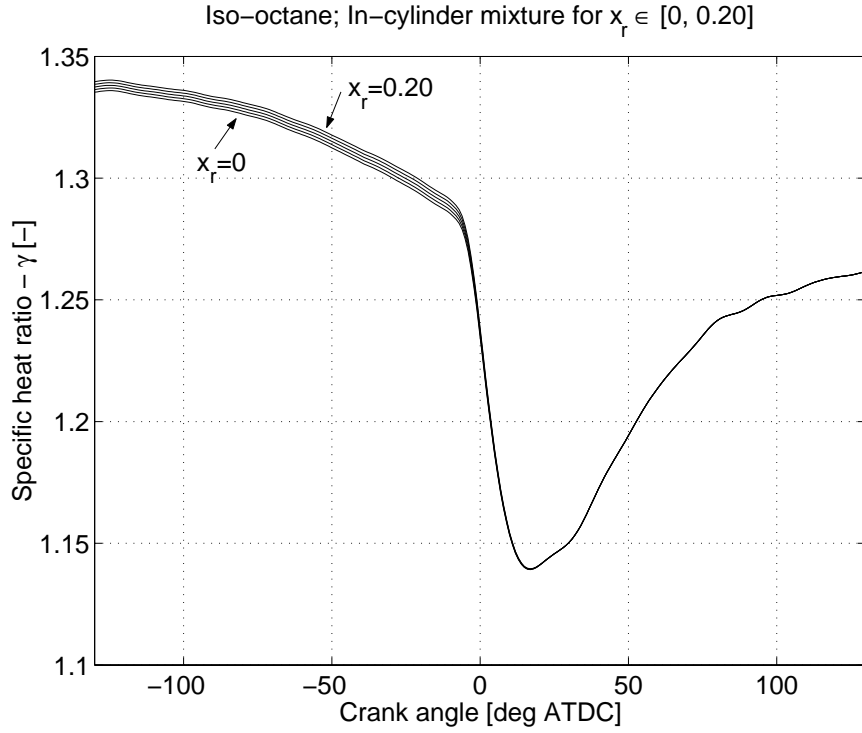


Figure 4.13: Specific heat ratio γ_{CE} for residual gas fraction $x_r = [0, 0.05, 0.1, 0.15, 0.20]$.

where it is used that $\gamma(T, p, x_b, x_r)$ coincides for every x_r when the mixture is fully burned.

A more appealing and more physically correct model is to extend model \mathcal{D}_1 in (4.24) with the Krieger-Borman polynomial for the residual gas fraction, in the same manner as in (4.31). Thus (4.24) is rewritten as

$$c_p(T, p, x_b, x_r) = x_b c_{p,b}^{KB}(T_b, p) + (1 - x_b) ((1 - x_r) c_{p,u}^{lin}(T_u) + x_r c_{p,b}^{KB}(T_u, p)) \quad (4.34a)$$

$$c_v(T, p, x_b, x_r) = x_b c_{v,b}^{KB}(T_b, p) + (1 - x_b) ((1 - x_r) c_{v,u}^{lin}(T_u) + x_r c_{v,b}^{KB}(T_u, p)) \quad (4.34b)$$

$$\gamma_{\mathcal{D}_{1x_r}}(T, p, x_b, x_r) = \frac{c_p(T, p, x_b, x_r)}{c_v(T, p, x_b, x_r)} \quad (4.34c)$$

to form the specific heat ratio $\gamma_{\mathcal{D}_{1x_r}}$ for a partially burned mixture with residual gas mass fraction x_r .

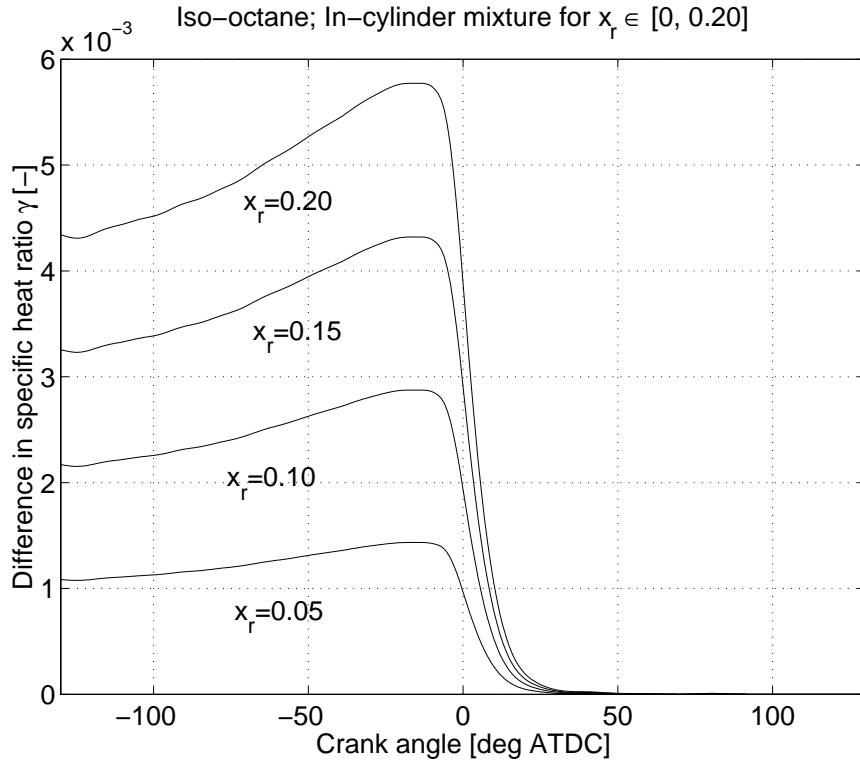


Figure 4.14: Difference in specific heat ratio γ_{CE} for residual gas fraction $x_r = [0.05, 0.1, 0.15, 0.20]$ compared to $x_r = 0$.

Evaluation

The specific heat ratio for the four models (4.32), (4.33), (4.34) and (4.14), i.e. no x_r modeling, are all compared to the reference model (4.31) for a given x_r . At the operating point in figure 4.14, the NRMSE in γ and the corresponding value of $\gamma_{bias}(x_r)$ for models (4.32) and (4.33) are given for the x_r :s at hand in table 4.9. The NRMSE for models (4.34) and (4.14) are also included. Model (4.33) has the best performance and decreases the NRMSE with approximately a factor 2, compared to model (4.14). Note that the NRMSE are relatively small compared e.g. the NRMSE given in table 4.6. The values for $\gamma_{bias}(x_r)$ depend almost linearly upon x_r , and it therefore seems promising to model $\gamma_{bias}(x_r)$ as a linear function of x_r . However, the slope b_{x_r} in $\gamma_{bias}(x_r) = b_{x_r}x_r$ will change for other operating conditions than the one given here. The model used therefore needs to be robust to changing operating conditions, a feature the Krieger-Borman polynomial has. Therefore model (4.34)

Model	NRMSE(γ) [%]			
	$x_r = 0.05$	$x_r = 0.10$	$x_r = 0.15$	$x_r = 0.20$
No model	$7.1 \cdot 10^{-2}$	$1.4 \cdot 10^{-1}$	$2.1 \cdot 10^{-1}$	$2.8 \cdot 10^{-1}$
(4.32)	$4.8 \cdot 10^{-2}$	$1.0 \cdot 10^{-1}$	$1.5 \cdot 10^{-1}$	$1.9 \cdot 10^{-1}$
(4.33)	$3.4 \cdot 10^{-2}$	$0.7 \cdot 10^{-1}$	$1.0 \cdot 10^{-1}$	$1.4 \cdot 10^{-1}$
(4.34)	$6.0 \cdot 10^{-2}$	$1.2 \cdot 10^{-1}$	$1.8 \cdot 10^{-1}$	$2.4 \cdot 10^{-1}$
Model	γ_{bias}			
	$x_r = 0.05$	$x_r = 0.10$	$x_r = 0.15$	$x_r = 0.20$
(4.32)	$6.5 \cdot 10^{-4}$	$1.3 \cdot 10^{-3}$	$2.0 \cdot 10^{-3}$	$2.6 \cdot 10^{-3}$
(4.33)	$6.0 \cdot 10^{-4}$	$1.2 \cdot 10^{-3}$	$1.8 \cdot 10^{-3}$	$2.4 \cdot 10^{-3}$

Table 4.9: Normalized root mean square error (NRMSE) and γ_{bias} for $x_r = [0.05, 0.10, 0.15, 0.20]$ using models (4.32) and (4.33). Model (4.14) corresponds to no x_r modeling.

which uses the Krieger-Borman polynomial is recommended, although it did not have the best performance of the x_r -models at this operating point.

4.6.9 Summary for partially burned mixture

The results can be summarized as:

- The modeling error must be compared both in terms of how they describe γ and the cylinder pressure.
- Comparing models \mathcal{C}_4 and \mathcal{D}_4 , it is obvious that interpolating the specific heat ratios directly instead of the specific heats causes a large pressure error. Interpolation of specific heat ratios does not fulfill the energy equation.
- The γ -models $\mathcal{B}_1, \mathcal{B}_2, \mathcal{B}_3, \mathcal{B}_4, \mathcal{C}_2$ and \mathcal{C}_5 proposed in earlier works, introduce a pressure modeling error which is at least four times the measurement noise, and at least ten times the measurement noise in the mean. If any of them should be used, model \mathcal{B}_1 should be considered.
- If only single-zone temperatures are allowed, model \mathcal{B}_1 is the better one.
- The computation times are of the same order for all models except $\mathcal{D}_3, \mathcal{D}_4$ and \mathcal{C}_4 .
- The models in group \mathcal{D} are required to get a cylinder pressure RMSE that is of the same order as the measurement noise.
- As a compromise between accuracy and computational time, model \mathcal{D}_1 is recommended. Compared to the original setting in Gatowski et al. [1984], the computational burden increases with 40 % and the cylinder pressure modeling error is 15 times smaller in mean.

- For a residual gas mass fraction x_r up to 20 %, model \mathcal{D}_1 can be extended with specific heats for the residual gas (4.34). These specific heats are modeled by the Krieger-Borman polynomial. This model extension adds a NRMSE(γ) which is less than 0.3 % to the previous modeling error for $x_r = 0$.
- The results are valid for the air-fuel ratio region $\lambda \in [0.975, 1.025]$ with retained accuracy. For other fuels than iso-octane, the hydrogencarbon ratio y needs to be close to 2.25, i.e. the one for iso-octane. The closer, the better the accuracy is. For a commercial fuel with ratio $y = 1.88$, the RMSE(p) is increased with 70 % compared to iso-octane for model \mathcal{D}_1 , which is acceptable.
- Only model group \mathcal{D} produces prediction error estimates of the heat release parameters, that are accurate within 1 % for all three parameters, and this suggests that any of the \mathcal{D} -models can be used, preferably model \mathcal{D}_1 due to its lower computational time.

4.7 Conclusions

Based on assumptions of frozen mixture for the unburned mixture and chemical equilibrium for the burned mixture [Krieger and Borman, 1967], the specific heat ratio is calculated, using a full equilibrium program [Eriksson, 2004], for an unburned and a burned air-fuel mixture, and compared to several previously proposed models of γ . It is shown that the specific heat ratio and the specific heats for the unburned mixture is captured within 0.25 % by a linear function in mean charge temperature T for $\lambda \in [0.8, 1.2]$, and the burned mixture is captured within 1 % by a higher-order polynomial in cylinder pressure p and T developed in Krieger and Borman [1967] for the major operating range of a spark ignited (SI) engine. If a linear model is preferred for computational reasons for the burned mixture, the temperature region should be chosen with care which can reduce the modeling error in γ by 25 %.

With the knowledge of how to describe γ for the unburned and burned mixture respectively, the focus is turned to finding a γ -model during the combustion process, i.e. for a partially burned mixture. This is done by interpolating the specific heats for the unburned and burned mixture using the mass fraction burned x_b . The objective of the work was to find a model of γ , which results in a cylinder pressure error less than or in the order of the measurement noise. It is found that interpolating the linear specific heats for the unburned mixture and the higher-order polynomial specific heats for the burned mixture, and then forming the specific heat ratio

$$\gamma(T, p, x_b) = \frac{c_p(T, p, x_b)}{c_v(T, p, x_b)} = \frac{x_b c_{p,b}^{KB} + (1 - x_b) c_{p,u}^{lin}}{x_b c_{v,b}^{KB} + (1 - x_b) c_{v,u}^{lin}} \quad (4.35)$$

results in a small enough modeling error in γ . This modeling error results in a cylinder pressure error less than 6 kPa in mean, which is in the same order as the cylinder pressure measurement noise.

It was also shown that it is important to evaluate the model error in γ to see what impact it has on the cylinder pressure, since a small error in γ can yield a large cylinder pressure error. This also stresses that the γ -model is an important part of the heat release model.

Applying the proposed model improvement \mathcal{D}_1 (4.35) of the specific heat ratio to the Gatowski et al. [1984] single-zone heat release model is simple, and it does not increase the computational burden immensely. Compared to the original setting, the computational burden increases with 40 % and the modeling error introduced in the cylinder pressure is reduced by a factor 15 in mean.

COMPRESSION RATIO ESTIMATION

Four methods for compression ratio estimation of an engine from cylinder pressure traces are described and evaluated for both motored and fired cycles. The first three methods rely upon a model of polytropic compression for the cylinder pressure, and it is shown that they give a good estimate of the compression ratio for simulated cycles at low compression ratios. For high compression ratios, this simple model lack the information about heat transfer and the model error causes the estimates to become biased. Therefore a fourth method is introduced where heat transfer and crevice effects are modeled, together with a commonly used heat release model for firing cycles. This method is able to estimate the compression ratio more accurately at low as well as high compression ratios.

In appendix B further details and argumentation on compression ratio estimation are given, and serves as a complement to this chapter. Parts of the material in this chapter and appendix B has previously been published [Klein et al., 2002; Klein and Eriksson, 2002; Klein et al., 2004].

5.1 Introduction

A newly developed engine, which can continuously change the compression ratio between 8 and 14 by tilting the mono-head, has been developed at SAAB Automobile AB. This ability to change the compression ratio opens up new opportunities to increase the efficiency of spark ignited (SI) engines by downsizing and super charging. But if the compression ratio gets stuck at too high ratios, the risk of engine destruction by heavy knock increases rapidly. If the compression ratio gets stuck at too low ratios, we get an unnecessary low effi-

ciency, and therefore an unnecessary high fuel consumption. It is therefore vital to monitor and diagnose the continuously changing compression ratio. Due to geometrical uncertainties, a spread of the compression ratio among the different cylinders is inherent [Amann, 1985], and since it is hard to measure the compression ratio directly, estimation is required. The questions asked here are related to: 1) accuracy, 2) convergence speed and 3) over all convergence. The approach investigated is to use cylinder pressure to estimate the compression ratio. A desirable property of the estimator is that it must be able to cope with the unknown offset introduced by the charge amplifier, changing thermodynamic conditions, and possibly also the unknown phasing of the pressure trace in relation to the crank angle revolution.

Two models for the cylinder pressure with different complexity levels, a polytropic model and a single-zone zero-dimensional heat release model [Gatowski et al., 1984] are used. To estimate the parameters in the cylinder pressure models, three different optimization algorithms minimizing the prediction error are utilized, namely:

1. *A linear subproblem approach*, where groups of the parameters are estimated one at a time and the predictor function is rewritten to be linear for the group of estimated parameters. Thus linear regression can be used at every substep for estimating the particular group of parameters.
2. *A variable projection method* [Björck, 1996], where one iteration consists of two substeps: The first substep estimates the parameters that are linear in the predictor function, holding the nonlinear constant. The second substep is to perform a line search in the direction of the negative gradient at the parameters found from substep one. This method classifies as a separable least squares method.
3. *Levenberg-Marquardt method*, i.e. a Gauss-Newton method with regularization, where numerical approximations of the gradient and the Hessian are used here.

Based on these models and optimization algorithms, four different methods are developed and used for compression ratio estimation for both motored and fired cycles.

5.2 The SVC engine

The principle of the SVC (Saab Variable Compression) engine is shown in figure 5.1. By tilting the mono-head the compression ratio can be continuously varied between 8 and 14. The geometric data for the SVC engine are given in appendix B.4.

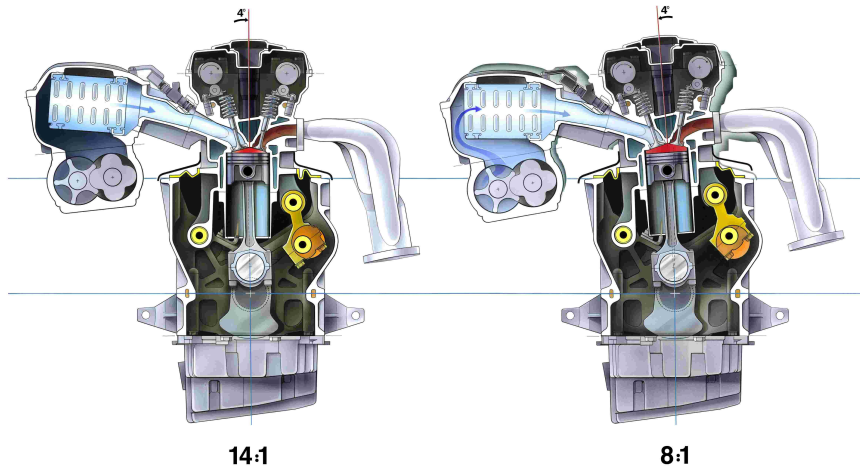


Figure 5.1: Schematic of engine with variable compression. © SAAB Automobile AB

5.2.1 SVC volume function

The cylinder volume sweep for the SVC is different in appearance compared to the standard volume function, $V_d(\theta) = \frac{\pi B^2 a}{4} \left(\frac{l}{a} + 1 - \cos \theta - \sqrt{\left(\frac{l}{a}\right)^2 - \sin^2 \theta} \right)$, since the geometry of the crank in relation to the cylinder changes when the cylinder head is tilted. This motivates the study done in appendix B.6.

5.3 Cylinder pressure modeling

Two models are used for describing the cylinder pressure trace and they are referred to as the polytropic model and the standard model. These models were described in sections 2.2 and 2.5 respectively, and this section serves as a summary of the models, repeated here for convenience.

5.3.1 Polytropic model

A simple but efficient model is the polytropic compression model:

$$p(\theta)V(\theta)^n = C \quad (5.1)$$

where p is the cylinder pressure, $V(\theta)$ is the volume function, n is the polytropic exponent and C is a cycle-to-cycle dependent constant. The model is

valid for adiabatic conditions, and works well during the compression and expansion phase of the engine cycle, but not during combustion [Heywood, 1988]. Therefore, for a firing cycle only data between inlet valve closing (IVC) and start of combustion (SOC) will be used, but for motored cycles all data during the closed part of the cycle, i.e. between IVC and exhaust valve opening (EVO), is utilized.

5.3.2 Standard model

Gatowski et al. [1984] develops, tests and applies the heat release analysis procedure used here. It maintains simplicity while still including the effects of heat transfer and crevice flows. The model has been widely used and the phenomena that it takes into account are well known [Heywood, 1988].

The pressure differential dp can be written as:

$$dp = \frac{\dot{d}Q_{ch} - \frac{\gamma}{\gamma-1} p dV - \dot{d}Q_{ht}}{\frac{1}{\gamma-1} V + \frac{V_{cr}}{T_w} \left(\frac{T}{\gamma-1} - \frac{1}{b} \ln \left(\frac{\gamma-1}{\gamma'-1} \right) + T' \right)} \quad (5.2)$$

This is an ordinary differential equation that easily can be solved numerically if a heat-release trace $\dot{d}Q_{ch}$ is provided. The heat release is modeled by the Vibe function x_b (5.3a) [Vibe, 1970] in its differentiated form (5.3b):

$$x_b(\theta) = 1 - e^{-a \left(\frac{\theta - \theta_0}{\Delta\theta} \right)^{m+1}} \quad (5.3a)$$

$$\frac{d}{d\theta} x_b(\theta) = \frac{a(m+1)}{\Delta\theta} \left(\frac{\theta - \theta_0}{\Delta\theta} \right)^m e^{-a \left(\frac{\theta - \theta_0}{\Delta\theta} \right)^{m+1}} \quad (5.3b)$$

Where x_b is the mass fraction burned, θ_0 is the start of the combustion, $\Delta\theta$ is the total combustion duration, and a and m are adjustable parameters. From (5.3b) the heat release trace is computed as:

$$\frac{dQ_{ch}}{d\theta} = Q_{in} \frac{dx_b}{d\theta} \quad (5.4)$$

where Q_{in} represents the total energy released from combustion. The standard model is valid between IVC and EVO.

5.4 Estimation methods

First a well-known method of cylinder pressure referencing is presented. Then four methods of how to estimate the compression ratio r_c are described, followed by summary in which the relation between the four methods are pointed out.

5.4.1 Cylinder pressure referencing

Piezoelectric pressure transducers are used for measuring the in-cylinder pressure, which will cause a drift in the pressure trace. This drift is assumed to be constant during one engine cycle, and can be estimated with various methods [Randolph, 1990]. Here the measured pressure trace $p_m(\theta)$ will be referenced by comparing it to the intake manifold pressure p_{man} just before inlet valve closing (IVC), for several samples of p_{man} . Due to standing waves in the intake runners at certain operating points, the referencing might prove to be insufficient. This is investigated by including a parameter for cylinder pressure bias for methods 3 and 4, and is interpreted as a second pressure referencing.

5.4.2 Method 1 – Sublinear approach

The first method estimates the polytropic exponent n , the compression ratio r_c and the constant C in the polytropic model. It iteratively solves two problems, one to determine the polytropic exponent n , and the other to determine the compression ratio r_c . By using the polytropic model (5.1)

$$p(\theta)(V_c(r_c) + V_d(\theta))^n = C \quad (5.5)$$

the compression ratio r_c can be estimated by iteratively estimating the clearance volume V_c (i.e. r_c) and the polytropic exponent n . This is done in three substeps.

Substep 1: The polytropic exponent n is assumed to be known and the clearance volume is estimated by rewriting (5.5). This yields a least squares problem which is linear in the parameters C_1 and V_c according to

$$V_d(\theta) = C_1 p(\theta)^{-1/n} - V_c(r_c) \quad (5.6)$$

where $C_1 = C^{1/n}$ and V_c are the parameters to be estimated.

Substep 2: The polytropic exponent n is then estimated using the estimate of V_c from substep 1. Applying logarithms on (5.5) yields

$$\ln p(\theta) = C_2 - n \ln(V_d(\theta) + V_c(r_c)) \quad (5.7)$$

which is linear in the parameters n and $C_2 = \ln C$. The linear parameters are estimated and we continue to substep 3.

Substep 3: Convergence test. If the estimate has not converged, return to substep 1.

Using this approach directly will cause diverging estimates [Klein and Eriksson, 2002]. If the stopping criteria is based upon the convergence of the estimated parameter values, the situation from figure 5.2 can occur, where the estimated parameters move away from the true parameter values. On the other hand, if the stopping criteria is based upon the value of the loss function, defined as the sum of squared residuals, the algorithm will stop in time, but the estimate will

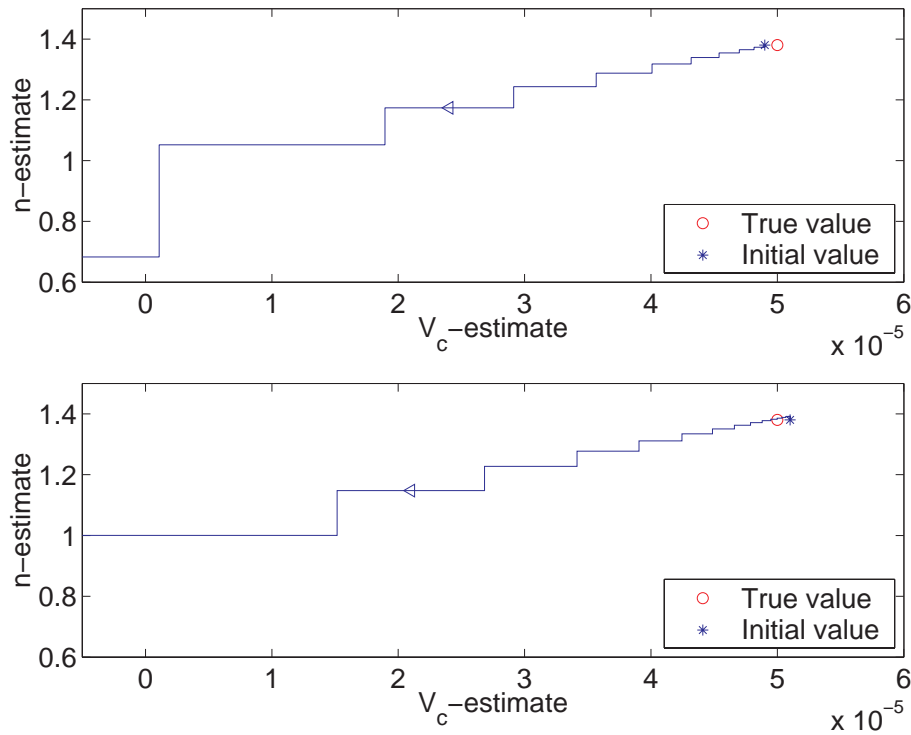


Figure 5.2: Diverging estimates for method 1 when applying (5.6) and (5.7) directly. The upper and lower plot have different initial values for the estimates.

depend upon the initial value. Using the loss function as the stopping criteria, the method stops in one iteration, i.e. two substeps.

The divergence is due to that the predictor function is rewritten from (5.6) to (5.7) or vice versa in every substep. If the problem would be bilinear in the parameters, the same predictor function could be used at every substep and the estimate would then converge linearly [Björck, 1996].

Rewriting the estimation problem:

In the case above the residuals resulting from the predictor functions (5.6) and (5.7) are unequal in size. A Taylor expansion shows that the residuals become equal in size if (5.7) is multiplied by $(V_c(r_c) + V_d(\theta))$ according to

$$(V_c + V_d(\theta)) \ln p(\theta) = (V_c + V_d(\theta))(C_2 - n \ln(V_d(\theta) + V_c)) \quad (5.8)$$

and (5.6) is multiplied by n according to

$$nV_d(\theta) = n(C_1 p(\theta)^{-1/n} - V_c(r_c)) \quad (5.9)$$

see appendix B.1 for details. Since n is constant, it does not have to be included in (5.9).

Stopping criteria: These modifications (5.8) and (5.9) stabilize the method in the sense that the parameter estimates after a few iterations jumps back and forth between two parameter sets. The jumping is due to that the norm of the two predictor functions are not exactly the same given the same parameters. However, at this stage the components of the two sets differ less than 0.1 % and can therefore be considered to be the same. By setting the stopping criteria to a parameter change less than 0.1 %, the method stops within ten iterations. This limit is not universally valid, and must be adapted for a specific engine and measurement setup. Also note that if this stopping criteria is not set, convergence can not be guaranteed for this method.

Since it can not be guaranteed that the loss function will monotonically decrease for method 1, a norm test of the loss function is added to the convergence test in substep 3. The method returns to substep 1 if the loss function has decreased with more than $1 \cdot 10^{-6}$ since the previous test. Otherwise it stops and returns the estimates. This will unfortunately slow down the method.

Pressure bias estimation

If the clearance volume V_c can be considered to be known, the same method can be used to estimate an additive pressure bias instead by reforming the weighting function in a straight-forward manner. This is also shown in appendix B.1.

5.4.3 Method 2 – Variable projection

The second method also uses the polytropic compression model (5.1), together with a variable projection algorithm. A nonlinear least squares problem $\min_x \|r(x)\|^2$ is *separable* if the parameter vector x can be partitioned such that $x = (y \ z)^T$:

$$\min_y \|r(y, z)\|_2 \quad (5.10)$$

is easy to solve. If $r(y, z)$ is linear in y , $r(y, z)$ can be rewritten as:

$$r(y, z) = F(z)y - g(z) \quad (5.11)$$

For a given z , this is minimized by:

$$y(z) = [F^T(z)F(z)]^{-1}F(z)^T g(z) = F^\dagger(z)g(z) \quad (5.12)$$

i.e by using linear regression where $F^\dagger(z)$ is the pseudo-inverse of $F(z)$. The original problem $\min_x \|r(x)\|^2$ can then be rewritten as:

$$\min_z \|r(y, z)\|_2 = \min_z \|g(z) - F(z)y(z)\|_2 \quad (5.13)$$

and

$$\begin{aligned} r(y, z) &= g(z) - F(z)y(z) = g(z) - F(z)F^\dagger(z)g(z) \\ &= (I - P_{F(z)})g(z) \end{aligned} \quad (5.14)$$

where $P_{F(z)}$ is the orthogonal *projection* onto the range of $F(z)$, thus the name variable projection method.

The polytropic model in (5.5) is rewritten as:

$$\ln p(\theta) = C_2 - n \ln(V_d(\theta') + V_c) \quad (5.15)$$

which is the same equation as (5.7). This equation is linear in the parameters $C_2 = \ln C$ and n and nonlinear in V_c and applies to the form given in (5.11). A computationally efficient algorithm [Björck, 1996, p.352] is summarized for our application in appendix B.2.

Stopping criteria: As for method 1, the convergence criteria for the loss function is set to $1 \cdot 10^{-6}$. For this application the method converges within four iterations.

Pressure bias estimation

If the clearance volume V_c can be considered to be known, the same method can be used to instead estimate an additive pressure bias. Details of this are shown in appendix B.1.

5.4.4 Method 3 – Levenberg-Marquardt

The third method uses the polytropic compression equation (5.1) as methods 1 and 2 did, but a pressure sensor model is added according to

$$p(\theta) = p_m(\theta) + \Delta p \quad (5.16)$$

in order to make the pressure referencing better. The crank angle phasing $\Delta\theta$ of the volume and pressure traces is also included in the polytropic model, which then can be written as

$$p(\theta) = p_m(\theta' + \Delta\theta) + \Delta p = C \cdot (V_d(\theta' + \Delta\theta) + V_c)^{-n} \quad (5.17)$$

Based on (5.17) the following nonlinear least squares problem is formulated

$$\min_x \sum_{i=1}^N (p_m(\theta_i) + \Delta p - C \cdot (V_d(\theta_i + \Delta\theta) + V_c)^{-n})^2 \quad (5.18)$$

A Levenberg–Marquardt method [Gill et al., 1981] is used to solve this nonlinear least squares problem. The Levenberg–Marquardt method is more fully

described in appendix B.3.

Stopping criteria: As for methods 1 and 2, the convergence criteria for the loss function is set to $1 \cdot 10^{-6}$. The problem has good numerical properties, the Levenberg–Marquardt method has second order local convergence and for this application the method converges within ten iterations.

5.4.5 Method 4 – Levenberg-Marquardt and standard model

The fourth method uses the single zone model (5.2) from Gatowski et al. [1984] which includes heat transfer and crevice effects, and serves as the reference method. It is therefore expected that it will improve the estimation accuracy. The free parameters are summarized in table 3.2. Due to the complexity of this model, the sublinear approach and variable projection approach are not applicable, and therefore only the Levenberg–Marquardt method is used. The Levenberg–Marquardt method is more fully described in appendix B.3. The increased complexity of the model also causes identifiability problems for some of the parameters, since there are many dependencies among the parameters. A systematic approach [Eriksson, 1998] of setting the most spurious parameter constant, and re-estimate with one parameter less is used. This should be done until a sufficient number of parameters are used. The most spurious parameter is found as the parameter that yields the highest variance, and is found by computing the eigenvector of the Hessian H_N (B.25) using singular value decomposition (SVD). At the moment, this method requires decision making from the user of how many parameters that should be set constant, i.e. how many spurious parameters there are. The remaining parameters are considered to be efficient and are free in the parameter estimation. This approach has earlier been successfully applied in Eriksson [1998] for motoring cycles, but here a heat-release model (5.3b) is included to cope with firing cycles.

Stopping criteria: As for methods 1, 2 and 3, the convergence criteria for the loss function is set to $1 \cdot 10^{-6}$. For this application the method converges within thirty iterations.

5.4.6 Summary of methods

The following table shows the relation between the different methods.

	Polytropic Model	Standard Model
Sublinear approach	Method 1	
Variable projection	Method 2	
Levenberg-Marquardt	Method 3	Method 4

For firing cycles, methods 1, 2 and 3 use cylinder pressure data between IVC and SOC only, in contrast to method 4 which uses data from the entire closed part of the engine cycle. For motoring cycles, all data during the closed part of the cycle is utilized by all methods.

5.5 Simulation results

Since the true values of the compression ratios of the engine are unknown, simulations of the cylinder pressure trace are necessary to perform and use for evaluating the four proposed methods. Only then can it be determined whether the estimates are accurate (unbiased) or not.

5.5.1 Engine data

Cylinder pressure simulations were made using the standard model (5.2) with representative single-zone parameters [Klein and Eriksson, 2002], for integer compression ratios between 8 and 13. The single-zone parameters are given in table 3.2. Sixty realizations of Gaussian noise with zero mean and standard

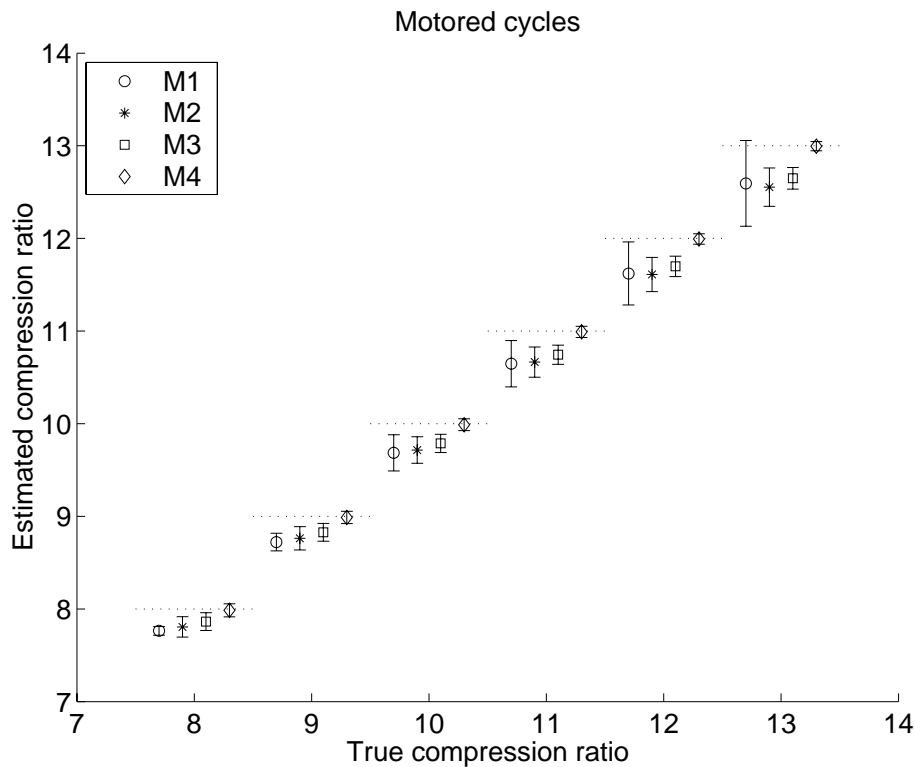


Figure 5.3: Mean and 95% confidence interval of the estimated compression ratio for motored cycles using the four methods, compared to the true compression ratio. The estimate should be as close to the horizontal line as possible.

deviation 2 kPa were added to the simulated cylinder pressures.

Figures 5.3 and 5.4 show a summary of all estimates for motored and fired cycles respectively. In the two figures the true compression ratios are the integer values 8 to 13 and for convenience, method 1 is moved to the left, method 2 is moved a little to the left (and to the right of method 1), method 3 is moved a little to the right and method 4 is to the right of method 3. The estimates should be as close to the dotted horizontal lines as possible. For convenience, magnifications of figure 5.3 for the two extremes $r_c = 8$ and $r_c = 13$ are given in figures B.7 and B.8 respectively, and magnifications of figure 5.4 for $r_c = 8$ and $r_c = 13$ are given in figures B.9 and B.10 respectively.

The following sections show the typical behavior of the estimation methods for a representative cycle at a high compression ratio $r_c = 13$ displayed in figure 5.5, where the effects of heat transfer are more likely to influence the measurements due to the higher pressure and temperature in the cylinder.

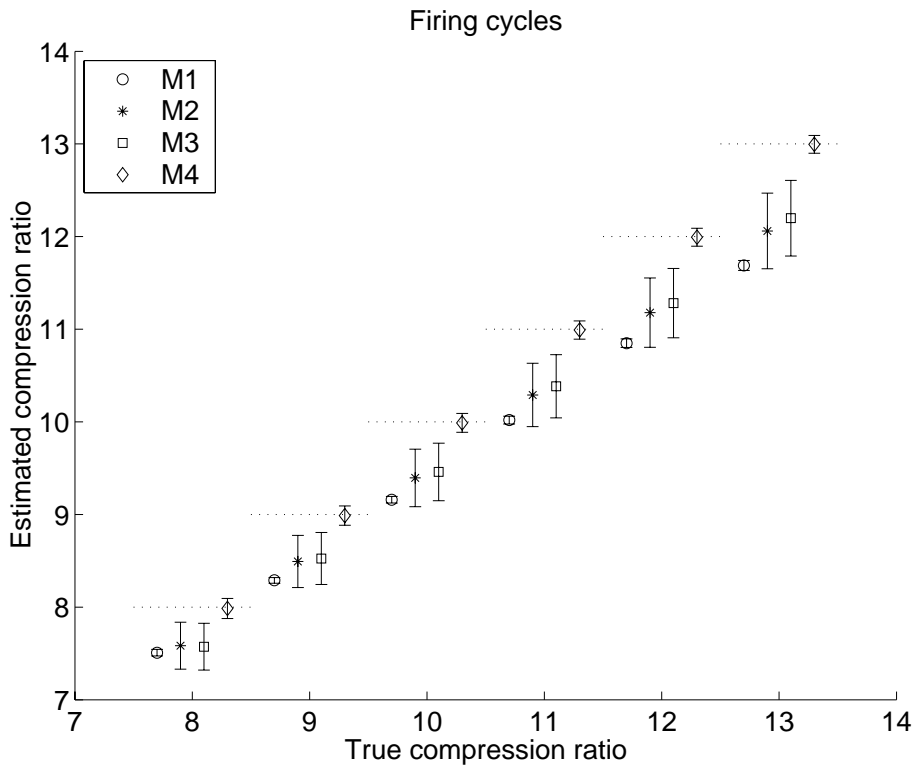


Figure 5.4: Mean and 95% confidence interval of the estimated compression ratio for fired cycles using the four methods, compared to the true compression ratio.

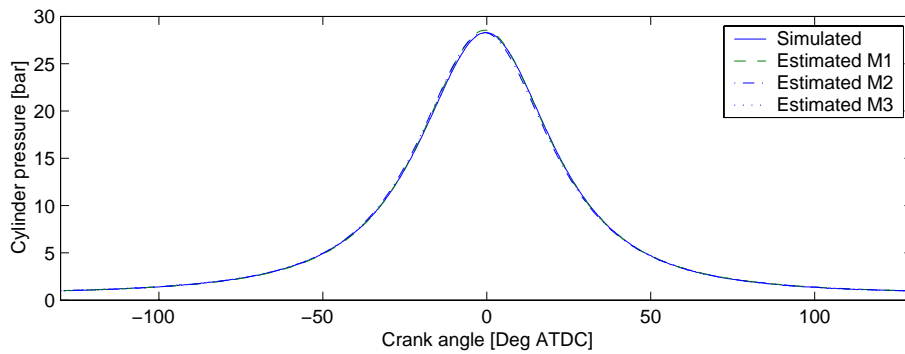


Figure 5.5: Simulated cylinder pressure for a motored cycle at $r_c = 13$.

Residuals for all methods are found in figures 5.6 to 5.9. In the summary section 5.5.5, statistics of the performance for the four methods are summarized for both firing and motoring cycles.

5.5.2 Method 1

Using the simulated cylinder pressure an estimation of the parameters is made, and from these a residual from the simulated and estimated cylinder pressure can be formed. In figure 5.6, the residual corresponding to the cylinder pressure in figure 5.5 for method 1 is shown. At the beginning of the compression phase and at the end of the expansion, the model and estimation method works satisfactory, but not in between where most of the heat transfer occurs. This model inaccuracy is partly covered by allowing the polytropic exponent to be small. The compression ratio estimate becomes biased and method 1 underestimates r_c for all compression ratios, as displayed in figures 5.3 and 5.4. The effect is larger the higher the compression ratio is. Method 1 converges within ten iterations for almost all simulated cylinder pressures, both firing and motored cycles.

5.5.3 Methods 2 and 3

Methods 2 and 3 show the same lack of model accuracy as method 1, although the residuals for $r_c = 13$ (figure 5.6) do not look exactly the same and again the estimated r_c is biased. Method 3 yields a smaller residual than methods 1 and 2, due to the higher flexibility of using five parameters instead of three. But when lowering the compression ratio the model becomes more accurate, and the residual in figure 5.7 does not show the same systematic deviation as the corresponding residual in figure 5.6 did. This is due to that the heat transfer and crevice effects are smaller, due to the lower pressure and temperature rendering from the lower compression ratio. The systematic deviation for the residuals are

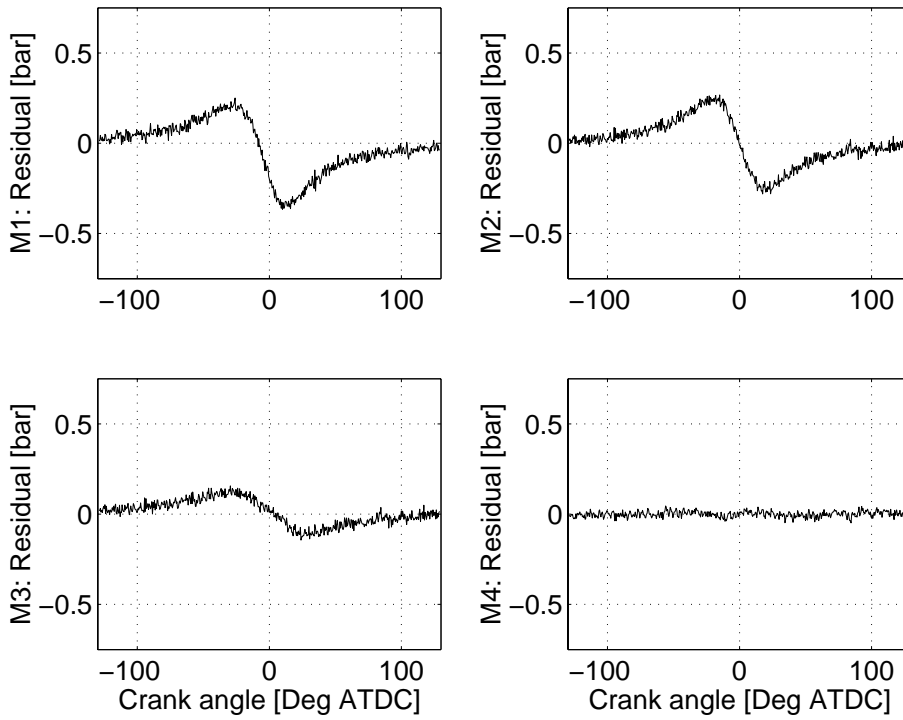


Figure 5.6: Difference between estimated and simulated cylinder pressure for all methods, given the motored cycle in figure 5.5.

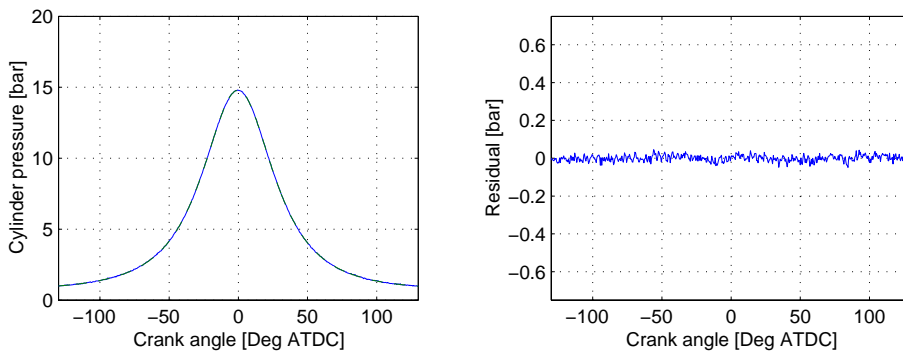


Figure 5.7: Difference between estimated and simulated cylinder pressure using method 3, for a motored cycle at $r_c = 8$.

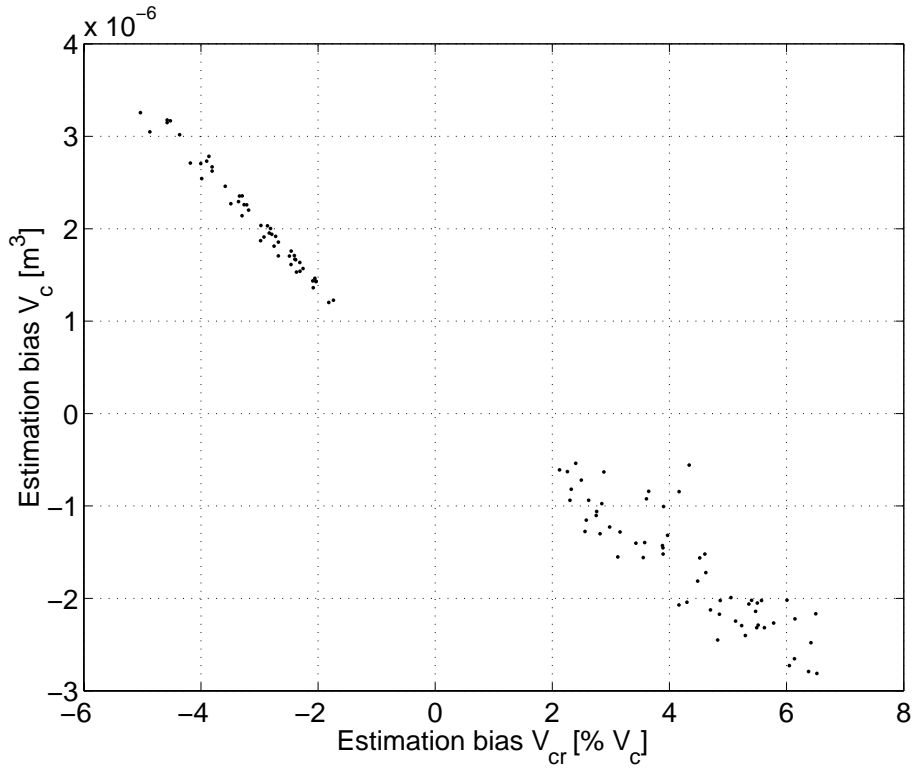


Figure 5.8: Dependence of estimation bias in clearance volume V_c and crevice volume V_{cr} .

expected since the crevice flow and heat transfer are not considered explicitly in the polytropic model (5.1) and it stresses that these phenomena must be taken into account when a better estimate is desired for higher compression ratios. Therefore method 4 uses the standard model (5.2).

5.5.4 Method 4

As mentioned in section 5.4, there exists correlations and dependencies among the estimated parameters, which makes the estimates biased. This is displayed in figure 5.8, where the dependence of estimation bias in clearance volume V_c and the estimation bias in crevice volume V_{cr} is given. Thus if a too small crevice volume is estimated, this will result in a too large clearance volume and thus a too small compression ratio. Therefore for simulated data, the crevice volume is set to its true value.

The residual for method 4 in figure 5.6 is white noise, suggesting that the

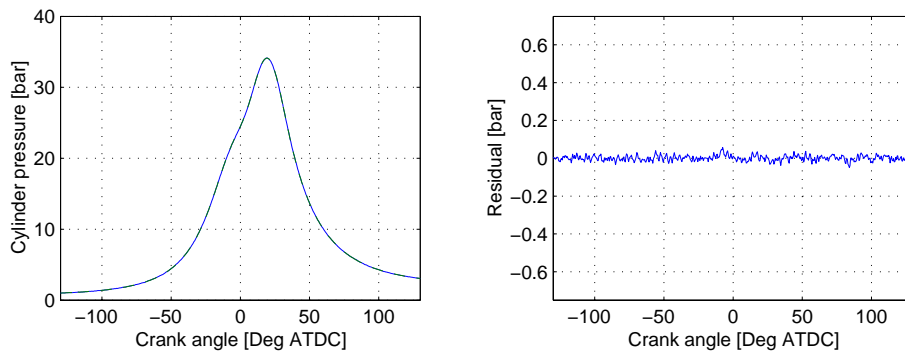


Figure 5.9: Difference between estimated and simulated cylinder pressure using method 4, for a fired cycle at $r_c = 13$.

estimation method can explain the data fully. This is also the case for firing cycles, see figure 5.9 where the simulated and estimated cylinder pressure for a single cycle at $r_c = 13$ is shown together with the residual. Therefore, the more complex method 4 shows the best ability to adjust to the simulated cylinder pressure and explain the physical phenomena taking place in the cylinder.

5.5.5 Summary of parameter estimations

Comparing the residuals from all methods, it is obvious that method 4 can explain the data most accurately. This suggests that the estimation of the compression ratio becomes best for method 4, which is also shown in figure 5.3 for motored cycles, where the mean and 95% confidence interval of the estimated compression ratio is shown for all four methods. The 95% confidence interval (B.35) is computed by assuming that the model is correct and that the estimation error asymptotically converges to a Gaussian distribution.

Methods 1, 2 and 3 underestimate the compression ratio, and this effect increases with the compression ratio. The methods give approximately the same estimates and 95 % confidence intervals, except for method 1 at $r_c = 13$, suggesting that the more time efficient one should be used. Table 5.8 shows e.g. the mean computational time for each method, from which it can be concluded that method 2 is the quickest alternative. Method 4 is able to estimate the compression ratio correctly, due to the higher flexibility of the model, and that it has the correct model structure. This suggests that method 2 or 4 should be used. Method 4 if accuracy is critical and method 2 if computational time is more important.

For firing cycles the same effect as for the motoring cycles appears and is even more pronounced as shown in figure 5.4. Method 1 shows poorer behavior than methods 2 and 3 concerning accuracy of the compression ratio estimate since it underestimates r_c even more, although it has a lower confidence interval.

Method	Type	CI [-]	RCI [%]	std [-]	RE_{max} [%]	RE_{mean} [%]
1	Fired	0.06	0.5	0.15	14.0	9.4
	Motored	0.23	2.0	0.041	3.9	3.1
2	Fired	0.33	3.1	0.12	4.0	6.2
	Motored	0.15	1.5	0.024	2.0	2.9
3	Fired	0.29	2.8	0.13	2.5	5.6
	Motored	0.10	1.0	0.011	1.4	2.2
4	Fired	0.10	1.0	0.032	0.5	0.2
	Motored	0.06	0.6	0.016	0.3	0.1

Table 5.1: Table showing the mean 95 % confidence interval (CI), mean relative confidence interval (RCI), standard deviation, maximum and mean relative error of the estimated compression ratio r_c .

Again, this suggests that method 2 or 4 should be used.

Table 5.1 summarizes the mean confidence intervals, standard deviation and the maximum relative error of the estimated compression ratio for 60 cycles respectively. The mean and maximum error is smallest for method 4 both for firing and motoring cycles.

The standard deviation is small for all methods, and the relative 95 % confidence interval are approximately less than 3 per cent for all methods. In table 5.2, the cylinder pressure RMSE is given for each method at compression ratios 8 til 13, as a mean of the ten simulated cycles at every operating condition. As expected, the RMSE is smaller for firing cycles than for motored, due to that the methods use fewer data for firing cycles. This makes it easier to find a good fit when the used model is not the true one, as for methods 1,

Method	Type	RMSE [kPa]: @ r_c					
		8	9	10	11	12	13
1	M	17	20	24	27	31	35
	F	6.4	6.6	6.8	7	7.2	7.5
2	M	13	15	18	20	23	25
	F	9.2	10	11	11	11	12
3	M	11	13	15	17	19	21
	F	6.6	6.9	7.1	7.3	7.2	7.3
4	M	1.4	1.5	1.5	1.5	1.6	1.6
	F	1.4	1.5	1.4	1.4	1.4	1.5

Table 5.2: Cylinder pressure RMSE for both firing (F) and motored (M) cycles for $r_c = 8, \dots, 13$ given in kPa. The RMSE for the simulated measurement noise is 2.0 kPa.

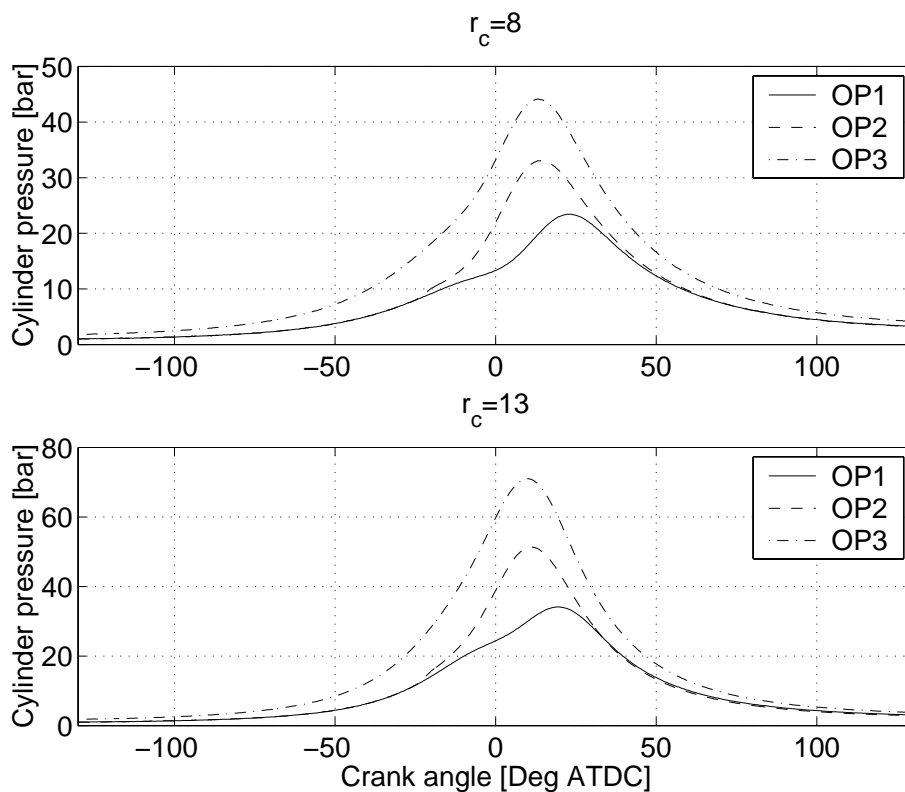


Figure 5.10: Simulated cylinder pressure for firing cycles for three operating points at $r_c = 8$ and $r_c = 13$ respectively.

2 and 3. The lower RMSE of firing cycles for method 4 comes from the model flexibility of the many parameters used. Method 1 has the worst RMSE, when considering motored cycles. For firing cycles, the RMSE is in the same order as method 3. In general, method 4 has the lowest RMSE, and method 3 is more flexible than method 2, thereby the lower RMSE for method 3.

5.5.6 A study of varying operating conditions

To investigate how the proposed methods behave for various operating conditions, a study is performed using the firing cycles in figure 5.10 and the motored cycles in figure 5.11. The cylinder pressures are simulated using the standard model (5.2) and the parameter values given in table 3.2, where the parameters; cylinder pressure at inlet valve closing p_{IVC} and ignition timing θ_{ig} , are altered to form different operating conditions according to Table 5.3. Note that for motored cycles OP1 and OP2 coincide, since they have the same p_{IVC} .

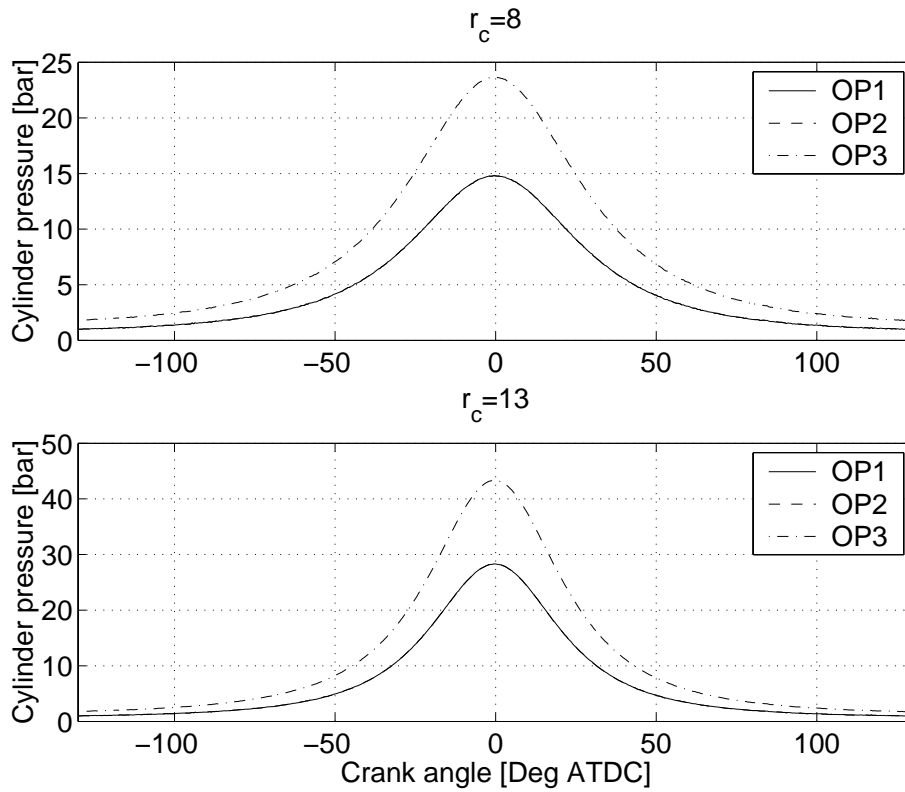


Figure 5.11: Simulated cylinder pressure for motored cycles for three operating points at $r_c = 8$ and $r_c = 13$ respectively.

Oper point	p_{IVC} [kPa]	θ_{ig} [deg ATDC]	Engine load case
OP1	100	-15	Low load
OP2	100	-25	Medium load
OP3	180	-25	High load

Table 5.3: The parameters that are altered compared to the parameter values given in table 3.2, for the different operating points. The engine load cases are given for firing cycles.

Oper point	M1		M2		M3		M4	
	@8	@13	@8	@13	@8	@13	@8	@13
OP1	6.2	10.1	5.2	7.2	5.3	6.2	0.2	0.5
OP2	6.4	11.2	9.1	12.4	9.3	10.6	0.2	0.4
OP3	6.2	10.4	8.1	11.3	8.3	9.6	0.3	0.7

Table 5.4: Relative mean estimation error [%] in r_c using methods 1, 2, 3 and 4 for firing cycles.

Table 5.4 summarizes the results for firing cycles in terms of relative mean estimation error, which is given by

$$RMEE = \frac{r_c^* - \frac{1}{M} \sum_{j=1}^M r_c^j}{r_c^*} \quad (5.19)$$

where r_c^j , $j = 1, \dots, M$ is the j :th estimate of r_c and r_c^* is the true compression ratio r_c . Methods 1, 2 and 3 has poorer performance, since the estimation error becomes larger for higher engine load operating conditions. This, as mentioned before, renders from the higher heat transfer due to the pressure and temperature in the cylinder. For method 3, the estimate is within 10% for a high engine load level (OP3). Method 4 has the best performance, and yields basically unbiased estimates, which are within 0.7 % for all operating points.

The relative mean estimation error (5.19) for the motored cycles are given in Table 5.5. Comparing estimation errors for motored and firing cycles, all methods are better for motored cycles. This is expected, since methods 1, 2 and 3 use a larger number of samples for the motored cycles. Comparing the methods themselves, method 4 is again the primary choice, producing a much smaller estimation error than methods 1, 2 and 3. Typically, the estimation errors become larger the higher the compression ratio or the engine load case are, a trend valid for all methods. Therefore, in this study the estimation error is largest for OP3 and $r_c = 13$.

Although this set of operating conditions is not extensive in any way by engine calibration standards, they still serve as a demonstration of the characteristics and properties of the proposed methods. It is also important to verify

Oper point	M1		M2		M3		M4	
	@8	@13	@8	@13	@8	@13	@8	@13
OP1	3.0	3.1	2.4	3.4	1.7	2.7	0.2	0.2
OP3	3.3	4.2	3.5	5.0	2.0	3.4	0.1	0.4

Table 5.5: Relative mean estimation error [%] in r_c using methods 1, 2, 3 and 4 for motored cycles.

Parameter	Deviation	M1		M2		M3	
		@8	@13	@8	@13	@8	@13
	$\pm 0 \%$	0	0	0	0	0	0
C_1	+50%	0.2	2.3	1.5	1.8	0.7	0.2
θ_0	$\pm 0.4^\circ$	0.2	1.1	1.6	1.4	0.07	0.1
Δp	± 20 kPa	9.5	30.2	28.4	37.3	3.3	4.1

Table 5.6: Relative mean estimation error for r_c compared to the case for no parameter deviation given in per cent, using methods 1, 2 and 3 for firing cycles.

the heat release and heat transfer models used in the standard model with experimental data. In the next section, a parameter sensitivity study is made to illustrate the problem of uncertainties in the models.

5.5.7 Parameter sensitivity analysis

How well do the proposed methods behave when subject to either a higher heat transfer, an inaccurate TDC determination or a badly referenced cylinder pressure? Using the standard model (5.2) and the parameter values given in table 3.2 which gave rise to the cylinder pressure in figure 5.5, the Woschni heat transfer coefficient C_1 , a crank angle phasing θ_0 and a pressure bias Δp are altered one at a time, according to Table 5.6. Method 4 is not included in the table, since the relative change in the estimate is less than 0.02 % for all parameter deviations. Methods 1 and 2 are not as robust to parameter deviations as method 3. This is exemplified by a badly referenced pressure, i.e. $\Delta p \neq 0$, which introduces large estimation errors from methods 1 and 2. Method 3 is therefore recommended if the referencing is uncertain. Methods 1 and 2 are not able to give correct r_c -estimates for $r_c = 13$ when subject to the deviations in Table 5.6. However, they perform better for lower r_c :s.

Table 5.7 displays the relative mean estimation error for r_c using motored cycles. Compared to the firing cycles given in Table 5.6, the errors are typically smaller. However, when the methods are subject to a pressure bias, they yield estimation errors in the same order for firing and motoring cycles. Methods 3 and 4 are able to cope with the pressure bias, since a parameter is included for both methods to estimate the pressure bias.

5.5.8 Conclusions from simulations

The first three methods rely upon the assumption of a polytropic compression and expansion, and it is shown that this is sufficient to get a rough estimate of the compression ratio, especially for low compression ratios and by letting the polytropic exponent to become small. This result is valid for a number of operating conditions, as shown in section 5.5.6. Methods 1, 2 and 3 perform

Parameter	Deviation	M1		M2		M3	
		@8	@13	@8	@13	@8	@13
	$\pm 0\%$	0	0	0	0	0	0
C_1	+50%	0.3	1.2	0.1	0.2	0.03	0.1
θ_0	$\pm 0.4^\circ$	0.3	0.8	0.1	0.2	0.01	0.02
Δp	± 20 kPa	14.8	28.4	17.0	17.6	0.1	0.4

Table 5.7: Relative mean estimation error for r_c compared to the case for no parameter deviation given in per cent, using methods 1, 2 and 3 for motored cycles.

equally well, when not considering model uncertainties such as cylinder pressure referencing. If this referencing is done unsatisfactorily, the estimate from methods 1 and 2 becomes poorer than the one from the more robust method 3. For higher r_c :s it is important to take the heat transfer into account, especially for high engine loads, and then only method 4 is accurate enough. Method 4 is also more robust to varying operating conditions and parameter deviations, than the other methods. It is interesting to note that for diagnostic purposes, all four methods will be able to detect when the compression ratio gets stuck at a too high or too low level.

Method	Time	# Iter	# Parameters
1	103 ms	8	3
2	23 ms	3	3
3	145 ms	5	5
4	$2 * 10^6$ ms	9	10

Table 5.8: Table showing the mean time and mean number of iterations in completing one cycle, together with the number of parameters for all methods.

The computational time for the four methods is quite diverse, and is summarized in table 5.8. The flexible method 4 takes 208 s, method 3 takes 0.145 s, method 2 is active for 23 ms and method 1 needs 103 ms in the mean to finish one cycle. Method 2 is the fastest choice. The estimations were made using Matlab 6.1 on a SunBlade 100, which has a 64-bit 500 Mhz processor.

Two methods are therefore recommended; If computational time is the most important feature, method 2 is recommended. If estimation accuracy has the highest priority, method 4 should be used.

5.6 Experimental results

The four proposed methods described in section 5.4 will be now used to estimate the compression ratio from experimental engine data. First the data collection is described, and the operating points are defined. In the following subsections, the engine cylinder pressure data is referenced both concerning pressure bias and crank angle offset. Thereafter, the performance of each of the methods is described and the section ends up in a summary part and a conclusion part for the experimental results.

5.6.1 Engine data

Data is collected on the SVC engine during stationary operation at engine speed $\{1500, 3000\}$ rpm, intake manifold pressure $\{0.6, 0.9\}$ bar and for a scan in compression ratio for integer values 8 to 13. For each compression ratio value, there are four operating points defined by table 5.9. Both firing and motored cylinder pressure data is acquired for one cylinder, where ten firing cycles are measured first and directly after these measurement the fuel is cut off and ten motored cycles are measured. The measurements are crank-angle resolved with a resolution of 1 CAD. Altogether there are data from 240 firing and 240 motored cycles to be analyzed. A representative motored cycle at compression ratio $r_c = 13$ for OP2 is given in figure 5.12. In the following, only results for OP2 will be shown. This operating point is chosen since the effects of heat transfer are larger due to the higher pressure and temperature in the cylinder.

Variable	OP1	OP2	OP3	OP4
p_{man} [bar]	0.6	0.9	0.6	0.9
N [rpm]	1500	1500	3000	3000
r_c [-]	8:13	8:13	8:13	8:13

Table 5.9: The operating points for the collected experimental SVC engine data.

5.6.2 TDC-referencing

As pointed out in subsection 3.1.1, the cylinder pressure trace needs to be referenced to the crank angle revolution, i.e. the cylinder volume function. An additive constant crank angle offset θ_0 is assumed and is modeled by (3.2). The easiest way to find θ_0 is to consider motored cycles only. The approach here will be to simulate the motored cylinder pressure for the operating points in table 5.9, and find the peak pressure position, $\theta_{ppp}^{sim}(OP)$. The simulations are performed using the Gatowski et al.-model with single-zone parameters given by table 3.2 with one exception; The parameters γ_{300} and b in the linear γ_{lin}^u model (4.2) are set to the values found in table 4.2, which are valid for an unburned frozen mixture of air and iso-octane. The peak pressure position for

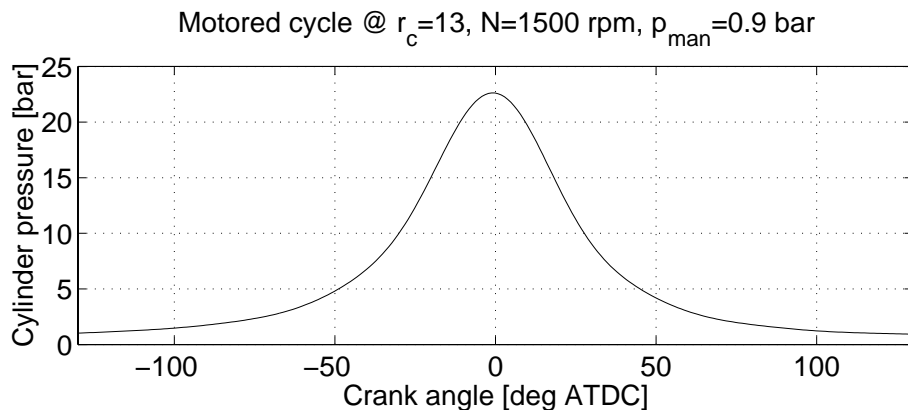


Figure 5.12: Measured cylinder pressure for a motored cycle at $r_c = 13$.

the experimental cycles are then computed and averaged for every operating point and compression ratio, to form $\theta_{ppp}^{exp}(OP)$. The crank angle offset θ_0 is then found as:

$$\theta_0 = \theta_{i,\text{true}} - \theta_i = \mathbf{mean}(\theta_{ppp}^{sim}(OP) - \theta_{ppp}^{exp}(OP)) \quad (5.20)$$

where $\theta_{i,\text{true}}$ is assumed to be given by the simulated values and θ_i is given by the experimental cycles. The mean is taken over all operating points for all compression ratios.

The peak pressure position for simulated and experimental cycles, corrected with θ_0 found from (5.20), are given in figure 5.13 for operating points 1 and 2. The simulated pressure maximum position, θ_{ppp}^{sim} , bends of for higher compression ratios. This is due to a higher heat transfer, and thereby the thermodynamic loss angle [Hohenberg, 1979] becomes larger, resulting in an earlier peak pressure position in the crank angle domain. Figure 5.14 displays the deviation in θ_{ppp} for simulated and corrected experimental cycles, for operating points 1-4 given by table 5.9. The deviation is within 0.2 degrees, and not within the 0.1 degrees that Morishita and Kushiyama [1997]; Staś [2000] state is needed to get accurate enough results. The underlying number of cycles from which θ_0 is determined is however very small, and it would require more data and a higher crank angle resolution to get more accurate results. This will not be pursued here, instead it is assumed that θ_0 is correct, but bear in mind that the TDC-determination could be a source of error.

5.6.3 Cylinder pressure referencing

The measured cylinder pressure is relative and needs to be referenced, in order to find the absolute pressure. This has previously been described in section 3.1 and subsection 5.4.1. The pressure gain K_p in (3.1) is calibrated beforehand,

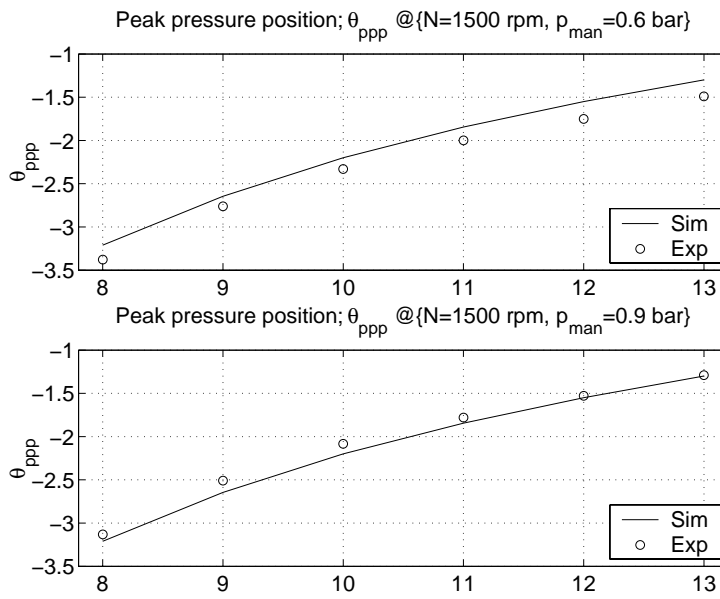


Figure 5.13: Position for pressure maximum θ_{ppp} for simulated and experimental cycles for operating points 1 (upper) and 2 (lower).

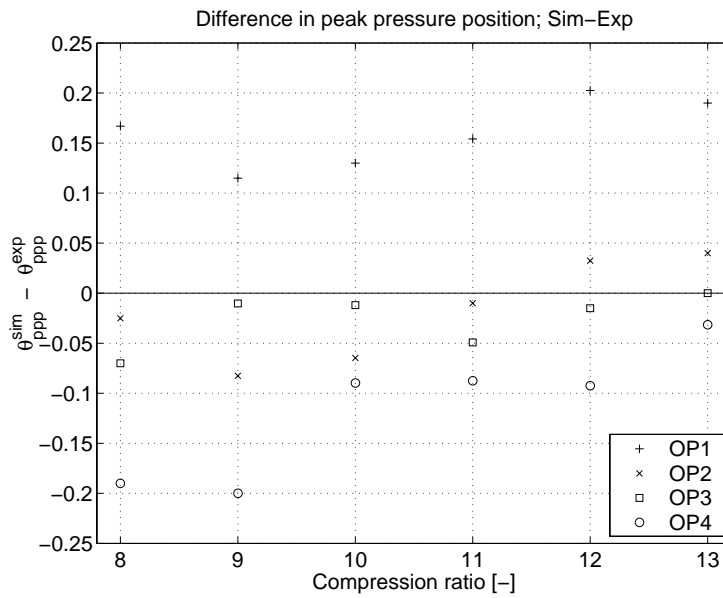


Figure 5.14: Deviation in θ_{ppp} for simulated and corrected experimental cycles.

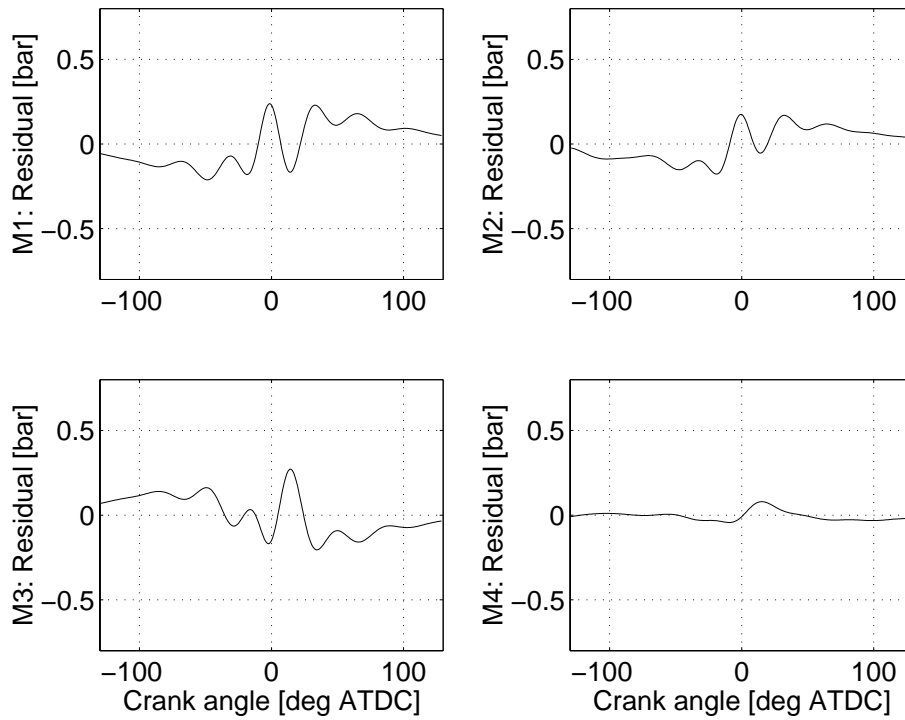


Figure 5.15: Difference between estimated and measured cylinder pressure for all methods, given the motored cycle in figure 5.12.

and the cycle-to-cycle pressure bias Δp is assumed constant and computed by referencing the cylinder pressure to the intake manifold pressure in the interval $\theta \in [-167, -162]$ [deg ATDC], as shown in figure 3.2.

5.6.4 Methods 1, 2 and 3

Figure 5.15 displays the residuals for all four methods, given the cylinder pressure in figure 5.12. For methods 1, 2 and 3, the polytropic model does not capture the experimental pressure fully. This is the case especially during the late compression and early expansion phase, where most of the heat transfer occurs.

The compression ratio estimate becomes biased and methods 1, 2 and 3 all underestimate r_c for all compression ratios, as displayed in figures 5.16 and 5.17. The effect is larger the higher the compression ratio is.

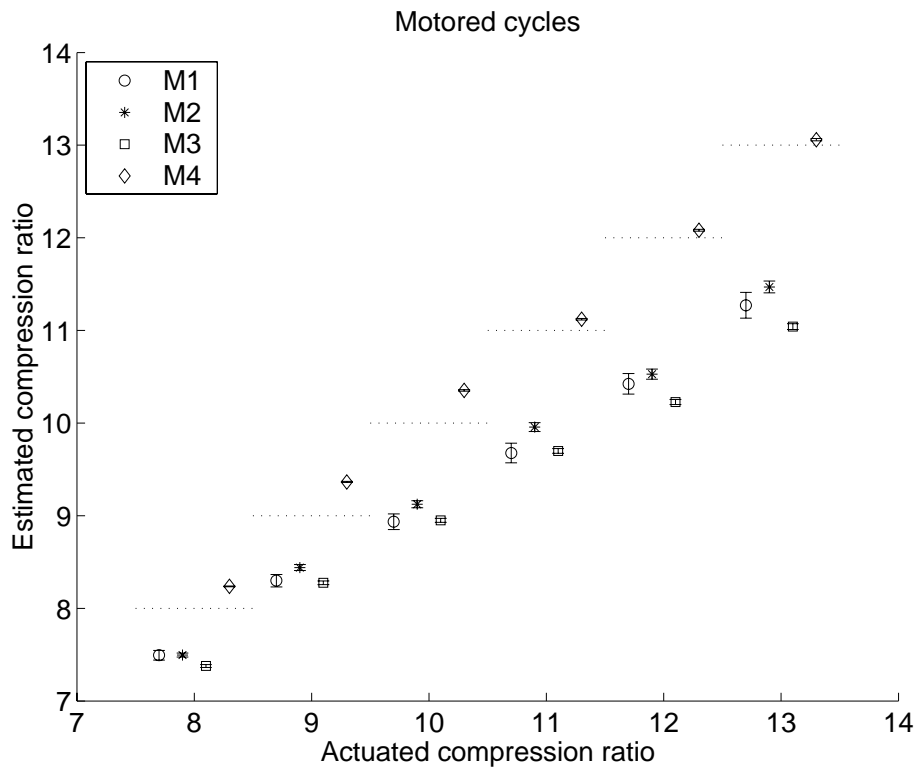


Figure 5.16: Mean and 95% confidence interval of the estimated compression ratio for motored cycles using the four methods, compared to the actuated compression ratio. The estimate should be as close to the horizontal line as possible.

5.6.5 Method 4

The simulations for method 4 showed that there was a coupling between the clearance volume V_c and the crevice volume V_{cr} , which was displayed in figure 5.8. For experimental data the crevice volume will however be unknown, and setting it to a fix value will introduce a bias in the compression ratio estimate. One way of partly avoiding this problem, is to estimate the crevice volume with a fix clearance volume at a given mid-range compression ratio, here chosen as $r_c = 11$. This will form the reference or nominal value of the crevice volume. This nominal value found from the estimations of the crevice volume will then be fixed, and used for estimating the clearance volume for all the other operating points. For motored cycles the crevice volume is set to $9.4 \cdot 10^{-7} m^3$, which is 2.9 % of the clearance volume at $r_c = 11$. A value larger than the 1-2 % Heywood [1988] suggests, but not unrealistic since the

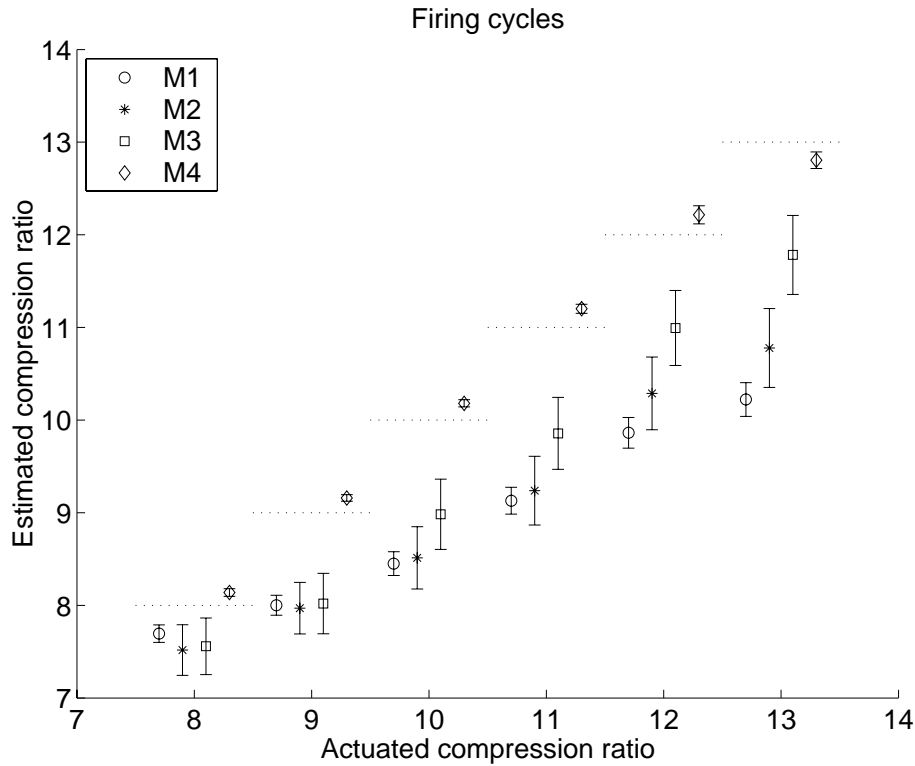


Figure 5.17: Mean and 95% confidence interval of the estimated compression ratio for fired cycles using the four methods, compared to the actuated compression ratio.

SVC engine is a prototype engine and therefore perhaps not optimized in every sense. For firing cycles, the crevice volume is set to $1.2 \cdot 10^{-6} \text{ m}^3$.

The systematic approach in Eriksson [1998] is used to decide upon which and how many parameters that are to be considered as free (efficient), and which are to be considered as constant (spurious). For motored cycles, it is found that five parameters should be considered as efficient. These are: pressure bias Δp , crank angle phasing θ_0 , cylinder mean wall temperature T_w , the constant γ_{300} in the linear model for the specific heat ratio and the clearance volume V_c . For firing cycles, eight parameters are considered to be efficient. The five used for motored cycles, except T_w exchanged for the mean charge temperature at IVC T_{IVC} , and the three heat release parameters θ_d , θ_b and Q_{in} . The other parameters are considered to be spurious and are set by their respective initial value by the models developed in chapter 3.

Method	Type	8	9	10	11	12	13
1	M	23	21	38	35	30	37
	F	20	18	29	26	23	31
2	M	4.8	5.9	7.4	9.2	11	13
	F	2.9	2.2	2.8	3.3	3.6	4.8
3	M	4.6	5.7	7.3	8.6	9.7	12
	F	2.7	1.9	2.7	2.3	2.4	2.8
4	M	2.7	3.7	4.7	4.6	5.3	6
	F	15	16	19	24	21	22

Table 5.10: Experimental cylinder pressure RMSE for both firing (F) and motored (M) cycles for $r_c = 8, \dots, 13$ given in kPa. The operating point is OP2.

5.6.6 Summary of parameter estimations

Comparing the residuals from all methods, it is obvious that method 4 can explain the data most accurately. This is confirmed by table 5.10, which shows the cylinder pressure RMSE for all methods at every integer compression ratio.

This suggests that the estimation of the compression ratio becomes best for method 4, which is also shown in figure 5.16 for motored cycles, where the mean and 95% confidence interval of the estimated compression ratio is shown for all four methods for motored cycles. The 95% confidence interval (B.35) is computed by assuming that the model is correct and that the estimation error asymptotically converges to a Gaussian distribution. In figure 5.16 the actuated compression ratios are the integer values 8 to 13 and for convenience, method 1 is moved to the left, method 2 is moved a little to the left (and to the right of method 1), method 3 is moved a little to the right and method 4 is to the right of method 3. The estimates should be as close to the dotted horizontal lines as possible. Magnifications of figure 5.16 for the two extremes $r_c = 8$ and $r_c = 13$ are given in figures B.11 and B.12 respectively, see appendix B.8.

For firing cycles the same effect as for the motoring cycles appears and is even more pronounced as shown in figure 5.17. Magnifications of figure 5.17 for $r_c = 8$ and $r_c = 13$ are given in figures B.13 and B.14 respectively.

Table 5.11 summarizes the mean 95 % confidence intervals, standard deviation and the mean relative error of the estimated compression ratio for 60 cycles respectively. The mean and maximum error is smallest for method 4 both for firing and motoring cycles. Of the methods that use the polytropic cylinder pressure model, method 2 yields the smallest mean estimation error and a relatively small 95 % confidence interval for motored cycles. For firing cycles, both method 1 and 2 suffer from poorer estimates. Method 3 on the other hand produce relatively accurate estimates, compared to methods 1 and 2, although the confidence interval is relatively large. In section 5.5.7, the influence of a poorly phased crank angle θ and a poorly referenced pressure bias Δp

Method	Type	CI [-]	RCI [%]	std [-]	RE_{max} [%]	RE_{mean} [%]
1	M	0.09	1.0	0.1	12	11
	F	0.14	1.5	0.39	20	14
2	M	0.04	0.4	0.055	10	9.1
	F	0.35	3.8	0.4	19	13
3	M	0.02	0.3	0.033	12	11
	F	0.37	3.9	0.41	15	9.2
4	M	0.01	0.1	0.044	2.9	2.1
	F	0.06	0.5	0.0072	1.8	1.7

Table 5.11: Table showing the mean 95 % confidence interval (CI), mean relative confidence interval (RCI), standard deviation, maximum and mean relative error (RE) of the estimated compression ratio r_c . The operating point is OP2.

Method	Time	# Iter	# Parameters
1	142 ms	12	3
2	30 ms	5	3
3	167 ms	6	5
4	$2 * 10^6$ ms	9	10

Table 5.12: Table showing the mean time and mean number of iterations in completing one cycle, together with the number of parameters for all methods.

were investigated, and it was shown that the estimates from methods 1 and 2 suffered from this. This might be the cause for the poor estimates for methods 1 and 2.

The mean computational time for all four methods is given in table 5.12. They are similar to the ones found from the simulations in table 5.8, although a bit higher. The relative ordering of the methods concerning computational time is however the same.

5.6.7 Conclusions from experiments

To conclude, method 4 has the best performance for both motored and firing cycles. If computational time is a critical issue, method 3 should be used. However, if the crank angle phasing and cylinder pressure referencing are accurate, method 2 could be used instead of method 3.

5.7 Conclusions

The four estimation methods all give good estimates for low compression ratios on simulated data. But for high compression ratios, the heat transfer has to be accounted for and therefore the more complex method 4 gives better estimates than the simpler and computationally faster methods 1, 2 and 3. Of these three, method 2 has the fastest convergence. For experimental data, method 4 again has the best performance. Of the computationally more efficient methods 1, 2 and 3, method 3 is recommended due to its robustness to crank angle phasing and pressure bias. With a better crank angle phasing and cylinder pressure referencing, method 2 could be used instead of method 3.

Two methods are therefore recommended. If computational time is the most important feature, method 3 is recommended. If estimation accuracy has the highest priority, method 4 should be used.

For diagnostic purposes, all methods are able to detect if the compression ratio is stuck at a too high or at a too low level during driving, since the estimation is performed on a cycle-to-cycle basis. This is sufficient both for safety reasons, where the compression ratio can be too high which could lead to engine knock, and for fuel economic reasons, where a too low compression ratio will lead to higher fuel consumption.

CONCLUSIONS

A specific heat ratio model for single-zone heat release models

Based on assumptions of frozen mixture for the unburned mixture and chemical equilibrium for the burned mixture [Krieger and Borman, 1967], the specific heat ratio is calculated, using a full equilibrium program [Eriksson, 2004], for an unburned and a burned air-fuel mixture. The results are then compared to several previously proposed models of γ . It is shown that the specific heat ratio and the specific heats for the unburned mixture is captured within 0.25 % by a linear function in mean charge temperature T for $\lambda \in [0.8, 1.2]$, and the burned mixture is captured within 1 % by a higher-order polynomial in cylinder pressure p and T developed in Krieger and Borman [1967] for the major operating range of a spark ignited (SI) engine. If a linear model for computational reasons would be preferred for the burned mixture, the temperature region should be chosen with care which can reduce the modeling error in γ by 25 %.

With the knowledge of how to describe γ for the unburned and burned mixture respectively, the focus is turned to finding a γ -model during the combustion process, i.e. for a partially burned mixture. This is done by interpolating the specific heats for the unburned and burned mixture using the mass fraction burned x_b . The objective of the work was to find a model of γ , which results in a cylinder pressure error less than or in the order of the measurement noise. It is found that interpolating the linear specific heats for the unburned mixture and the higher-order polynomial specific heats for the burned mixture, and then

forming the specific heat ratio

$$\gamma(T, p, x_b) = \frac{c_p(T, p, x_b)}{c_v(T, p, x_b)} = \frac{x_b c_{p,b}^{KB} + (1 - x_b) c_{p,u}^{lin}}{x_b c_{v,b}^{KB} + (1 - x_b) c_{v,u}^{lin}} \quad (6.1)$$

results in a small enough modeling error in γ . This modeling error results in a cylinder pressure error less than 6 kPa in mean, which is in the same order as the cylinder pressure measurement noise.

It was also shown that it is important to evaluate the model error in γ to see what impact it has on the cylinder pressure, since a small error in γ can yield a large cylinder pressure error. This also stresses that the γ -model is an important part of the heat release model.

Applying the proposed model improvement, model \mathcal{D}_1 (6.1), of the specific heat ratio to the Gatowski et al. [1984] single-zone heat release model is simple, and only increases the computational burden slightly. Compared to the original model, the computational burden increases with 40 % and the modeling error introduced in the cylinder pressure is reduced by a factor 15 in mean.

Compression ratio estimation

The four estimation methods all give good estimates for low compression ratios on simulated data. But for high compression ratios, the heat transfer has to be accounted for and therefore the more complex method 4 gives better estimates than the simpler and computationally faster methods 1, 2 and 3. Of these three, method 2 has the fastest convergence. For experimental data, method 4 again has the best performance. Of the computationally more efficient methods 1, 2 and 3, method 3 is recommended due to its robustness to crank angle phasing and pressure bias. If the crank angle phasing and cylinder pressure referencing are accurate, method 2 could be used instead of method 3.

Two methods are therefore recommended. If computational time is the most important feature, method 3 is recommended. If estimation accuracy has the highest priority, method 4 should be used.

For diagnostic purposes, all methods are able to detect if the compression ratio is stuck at a too high or at a too low level during driving, since the estimation is performed on a cycle-to-cycle basis. This is sufficient both for safety reasons, where the compression ratio can be too high which could lead to engine knock, and for fuel economic reasons, where a too low compression ratio will lead to higher fuel consumption.

REFERENCES

- C.A. Amann. Cylinder pressure measurement and its use in engine research. 1985. SAE Technical Paper 852067.
- I. Andersson. Cylinder pressure and ionization current modeling for spark ignited engines. Technical report, Vehicular Systems, 2002. LiU-TEK-LIC-2002:35, Thesis No. 962.
- W. J. D. Annand. Heat transfer in the cylinders of reciprocating internal combustion engines. *Proc. Instn. Mechanical Engineers*, Vol. 177, 1963. 36.
- I. Arsie, G. Flauti, C. Pianese, and G. Rizzo. Cylinder thermal state detection from pressure cycle in si engine. 4th International Conference on Internal Combustion Engines: Experiments and Modeling, Capri, Italy, 1999.
- E. Bergstedt. A sliding mode observer for a nonlinear temperature estimation in a cylinderhead of a diesel engine. Master's thesis, Linköping University, SE-581 83 Linköping, 2002. LiTH-ISY-EX-3255-2002.
- Å. Björck. *Numerical Methods for Least Squares Problems*. Siam, 1996.
- M.F.J. Brunt and A.L. Emtage. Evaluation of imep routines and analysis errors. In *Spark-Ignition Engine Combustion and Emissions (SP-1157)*, 1996. SAE Technical Paper 960609.
- M.F.J. Brunt and A.L. Emtage. Evaluation of burn rate routines and analysis errors. In *Spark-Ignition Engine Combustion and Emissions (SP-1267)*, 1997. SAE Technical Paper 970037.

- M.F.J. Brunt and C.R. Pond. Evaluation of techniques for absolute cylinder pressure correction. In *Spark-Ignition Engine Combustion and Emissions (SP-1267)*, 1997. SAE Technical Paper 970036.
- M.F.J. Brunt, A. Rai, and A.L. Emtage. The calculation of heat release energy from engine cylinder pressure data. In *SI Engine Combustion*, 1998. SAE Technical Paper 981052.
- H.M. Cheung and J.B. Heywood. Evaluation of a one-zone burn-rate analysis procedure using production si engine pressure data. 1993. SAE Technical Paper 932749.
- K. M. Chun and J. B. Heywood. Estimating heat-release and mass-of-mixture burned from spark-ignition engine pressure data. *Combustion Sci. and Tech.*, Vol. 54:133–143, 1987.
- L. Eriksson. Requirements for and a systematic method for identifying heat-release model parameters. *Modeling of SI and Diesel Engines*, SP-1330:19–30, 1998. SAE Technical Paper no.980626.
- L. Eriksson. *Spark Advance Modeling and Control*. PhD thesis, Linköping University, May 1999. ISBN 91-7219-479-0, ISSN 0345-7524.
- L. Eriksson. Chepp –a chemical equilibrium program package for matlab. volume SP-1830, 2004. SAE Technical Paper 2004-01-1460.
- J.W. Fox, W.K. Cheng, and J.B. Heywood. A model for predicting residual gas fraction in spark ignition engines. 1993. SAE Technical Paper 931025.
- J.A. Gatowski, E.N. Balles, K.M. Chun, F.E. Nelson, J.A. Ekchian, and J.B. Heywood. Heat release analysis of engine pressure data. 1984. SAE Technical Paper 841359.
- P.E. Gill, W. Murray, and M.H. Wright. *Practical Optimization*. Academic Press, 1981.
- Y.G. Guezennec and W. Hamama. Two-zone heat release analysis of combustion data and calibration of heat transfer correlation in an I.C. engine. 1999. SAE Technical paper 1999-01-0218.
- T.K. Hayes, R.A. White, and J.E. Peters. Combustion chamber temperature and instantaneous local heat flux measurements in a spark ignition engine. 1993. SAE Technical Paper 930217.
- J. B. Heywood. *Internal Combustion Engine Fundamentals*. McGraw-Hill series in mechanical engineering. McGraw-Hill, 1988. ISBN 0-07-100499-8.
- G.F. Hohenberg. Advanced approaches for heat transfer calculations. 1979. SAE Technical Paper 790825.

- B. Johansson. *On Cycle to Cycle Variations in Spark Ignition Engines*. PhD thesis, Lund Institute of Technology, 1995.
- M. Klein and L. Eriksson. Models, methods and performance when estimating the compression ratio based on the cylinder pressure. Fourth conference on Computer Science and Systems Engineering in Linköping (CCSSE), 2002.
- M. Klein and L. Eriksson. A specific heat ratio model for single-zone heat release models. *Modeling of SI Engines*, SP-1830, 2004. SAE Technical Paper 2004-01-1464.
- M. Klein, L. Eriksson, and Y. Nilsson. Compression estimation from simulated and measured cylinder pressure. *Electronic Engine Control*, SP-1330, 2002. SAE 2002 Transactions Journal of Engines, 111(3), September 2003. SAE Technical Paper 2002-01-0843.
- M. Klein, L. Eriksson, and J. Åslund. Compression ratio estimation based on cylinder pressure data. 2004. In proceedings of IFAC symposium on Advances in Automotive Control, Salerno, Italy.
- R.B. Krieger and G.L. Borman. The computation of apparent heat release for internal combustion engines. *ASME*, 1967.
- D. R. Lancaster, R. B. Krieger, and J. H. Lienesch. Measurement and analysis of engine pressure data. 1975. SAE Technical Paper 750026.
- L. Ljung. *System Identification Theory for the User*. Prentice Hall, 2nd edition, 1999.
- F.A. Matekunas. Modes and measures of cyclic combustion variability. 1983. SAE Technical Paper 830337.
- M. Mladek and C.H. Onder. A model for the estimation of inducted air mass and residual gas fraction using cylinder pressure measurements. 2000. SAE Technical Paper 2000-01-0958.
- M. Morishita and T. Kushiya. An improved method for determining the TDC position in a pv-diagram (first report). *SAE Technical Paper 970062*, 1997.
- Y. Nilsson and L. Eriksson. A new formulation of multi-zone combustion engine models. IFAC Workshop: Advances in Automotive Control, pages 629–634, Karlsruhe, Germany, 2001.
- Y. Nilsson and L. Eriksson. Determining tdc position using symmetry and other methods. *Modeling of SI Engines*, SP-1830, 2004. SAE Technical Paper 2004-01-1458.

- R. Pivec, T. Sams, and A. Wimmer. Wärmeübergang im ein- und auslasssystem. pages 658–663, 1998. MTZ Motortechnische Zeitschrift 59 (1998) Nr. 10.
- A.L. Randolph. Methods of processing cylinder-pressure transducer signals to maximize data accuracy. 1990. SAE Technical Paper 900170.
- G.M. Rassweiler and L. Withrow. Motion pictures of engine flames correlated with pressure cards. *SAE Technical Paper 800131*, 1938.
- S. Schagerberg and T. McKelvey. Instantaneous crankshaft torque measurements – modeling and validation. 2003. SAE Technical Paper No. 2003-01-0718.
- F. Schmidt, R. Henderson, and C. Wolgemuth. *Introduction to thermal sciences*. John Wiley & Sons, Inc., 2nd edition, 1993.
- P.J. Shayler, S.A. May, and T. Ma. The determination of heat transfer from the combustion chambers of si engines. 1993. SAE Technical Paper 931131.
- M.J. Staś. Thermodynamic determination of t.d.c. in piston combustion engines. 1996. SAE Technical Paper 960610.
- M.J. Staś. A universally applicable thermodynamic method for t.d.c. determination. 2000. SAE Technical Paper 2000-01-0561.
- R. Stone. *Introduction to Internal Combustion Engines*. SAE International, 3rd edition, 1999.
- R.A. Svehla and B.J. McBride. Fortran iv computer programs for calculation of thermodynamic and transport properties of complex chemical systems. Technical Report NASA Technical Note TND-7056, NASA Lewis Research Center, 1973.
- M.J. van Nieuwstadt, I.V. Kolmanovsky, D. Brehob, and M. Haghgoie. Heat release regressions for gdi engines. 2000. SAE Technical Paper 2000-01-0956.
- I.I. Vibe. *Brennverlauf und Kreisprozess von Verbrennungsmotoren*. VEB Verlag Technik Berlin, 1970. German translation of the russian original.
- N. Watson and M.S. Janota. *Turbocharging the Internal Combustion Engine*. The Macmillan Press Ltd, 1982. ISBN 0-333-24290-4.
- A. Wimmer, R. Pivec, and T. Sams. Heat transfer to the combustion chamber and port walls of ic engines – measurement and prediction. 2000. SAE Technical Paper 2000-01-0568.
- G. Woschni. A universally applicable equation for the instantaneous heat transfer coefficient in the internal combustion engine. 1967. SAE Technical Paper No. 670931.

Y.A. Çengel and M.A. Boles. *Thermodynamics: An Engineering Approach*. McGraw-Hill, 4th edition, 2002. <http://highered.mcgraw-hill.com>.

A SPECIFIC HEAT RATIO MODEL – FURTHER DETAILS

Further additional details and argumentation for the results found in chapter 4 are given in this chapter. Each section is referenced from various sections in chapter 4, and this chapter should therefore be seen as a complement.

A.1 Temperature models

Two models for the in-cylinder temperature will be described, the first is the mean charge single-zone temperature model. The second is a two-zone mean temperature model, used to compute the single-zone thermodynamic properties as mean values of the properties in a two-zone model.

A.1.1 Single-zone temperature model

The mean charge temperature T for the single-zone model is found from the state equation $pV = m_cRT$, assuming the total mass of charge m_c and the mass specific gas constant R to be constant. These assumptions are reasonable since the molecular weights of the reactants and the products are essentially the same [Gatowski et al., 1984]. If all thermodynamic states $(p_{ref}, T_{ref}, V_{ref})$ are known/evaluated at a given reference condition ref , such as IVC, the mean charge temperature T is computed as

$$T = \frac{T_{IVC}}{p_{IVC}V_{IVC}}pV \quad (\text{A.1})$$

A.1.2 Two-zone mean temperature model

A two-zone model is divided into two zones; one containing the unburned gases and the other containing the burned gases, separated by a infinitesimal thin divider representing the flame front. Each zone is homogeneous considering temperature and thermodynamic properties, and the pressure is the same throughout all zones [Nilsson and Eriksson, 2001]. Here a simple two-zone model will be used to find the burned zone temperature T_b and the unburned zone temperature T_u , in order to find a more accurate value of $\gamma(T)$ as an interpolation of $\gamma_u(T_u)$ and $\gamma_b(T_b)$. The model is called temperature mean value approach [Andersson, 2002], and is based on a single-zone combustion model and adiabatic compression of the unburned charge. The single-zone temperature can be seen as a mass-weighted mean value of the two zone temperatures.

Prior to start of combustion (SOC), the unburned zone temperature T_u equals the single-zone temperature T :

$$T_{u,SOC} = T_{SOC} \quad (\text{A.2})$$

The unburned zone temperature T_u after SOC is then computed assuming adiabatic compression of the unburned charge according to:

$$T_u = T_{u,SOC} \left(\frac{p}{p_{SOC}} \right)^{1-1/\gamma} = T_{SOC} \left(\frac{p}{p_{SOC}} \right)^{1-1/\gamma} \quad (\text{A.3})$$

The unburned zone temperature T_u is therefore given by:

$$T_u(\theta) = \begin{cases} T(\theta) & \theta \leq \theta_{ig} \\ T(\theta_{ig}) \left(\frac{p}{p(\theta_{ig})} \right)^{1-1/\gamma} & \theta > \theta_{ig} \end{cases} \quad (\text{A.4})$$

Energy balance between the single-zone and the two-zone models yields:

$$(m_b + m_u)c_v T = m_b c_{v,b} T_b + m_u c_{v,u} T_u \quad (\text{A.5})$$

Assuming $c_v = c_{v,b} = c_{v,u}$, i.e. a calorically perfect gas, ends up in

$$T = \frac{m_b T_b + m_u T_u}{m_b + m_u} = x_b T_b + (1 - x_b) T_u \quad (\text{A.6})$$

where the single-zone temperature can be seen as the mass-weighted mean temperature of the two zones. Including a model for c_v would increase the importance of T_b in (A.6), resulting in a lower value for T_b . From (A.6), T_b is found as

$$T_b = \frac{T - (1 - x_b) T_u}{x_b} \quad (\text{A.7})$$

The procedure is summarized as:

1. Compute the single-zone temperature T in (A.1)

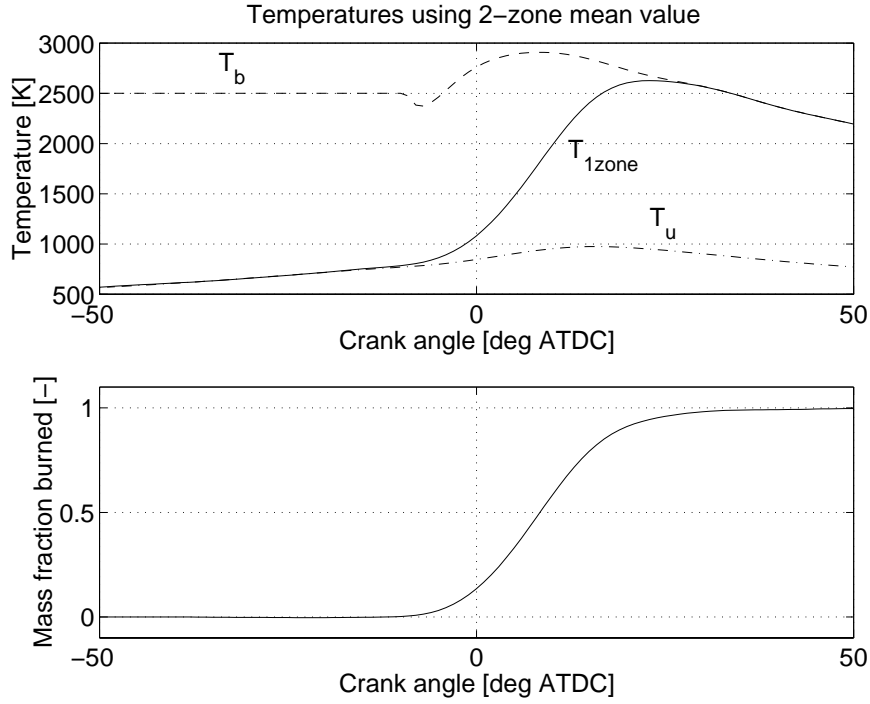


Figure A.1: *Upper:* Single-zone temperature T_{1z} , unburned T_u and burned T_b zone temperatures for the cylinder pressure given in figure 4.8. *Bottom:* Corresponding mass fraction burned trace calculated using Matekunas pressure ratio.

2. Compute the mass fraction burned x_b by using e.g. Matekunas pressure ratio management (A.10) and use the Vibe function in (A.12) to parameterize the solution
3. Compute the unburned zone temperature T_u using (A.4)
4. Compute the burned zone temperature T_b from (A.7)

The various zone temperatures for the cylinder pressure trace displayed in figure 4.8 are shown in figure A.1. The burned zone temperature is sensitive to low values of the mass fraction burned, x_b . Therefore, T_b is set to the adiabatic flame temperature for $x_b < 0.01$. The adiabatic flame temperature T_{ad} for a

constant pressure process is found from:

$$h_u(T_u) = h_b(T_{ad}, p) \quad (\text{A.8})$$

where h_u and h_b are the enthalpy for the unburned and burned mixture respectively.

A.2 Cylinder pressure model

The article [Gatowski et al., 1984] develops, tests and applies the cylinder pressure model used here. It maintains simplicity while still including the effects of heat transfer and crevice flows. The model has been widely used and the phenomena that it takes into account are well known [Heywood, 1988].

The pressure differential dp can be written as

$$dp = \frac{\dot{d}Q_{ch} - \frac{\gamma}{\gamma-1} p dV - \dot{d}Q_{ht}}{\frac{1}{\gamma-1} V + \frac{V_{cr}}{T_w} \left(\frac{T}{\gamma-1} - \frac{1}{b} \ln \left(\frac{\gamma-1}{\gamma'-1} \right) + T' \right)} \quad (\text{A.9})$$

This is an ordinary differential equation that easily can be solved numerically if a heat-release trace $\dot{d}Q_{ch}$ is provided. The heat release is modeled by the Vibe function described in section A.3.

A.3 Combustion model

The combustion of fuel and air is a very complex process, and would require extensive modeling to fully capture. Our approach here is to use the pressure ratio management [Matekunas, 1983] to produce a mass fraction burned trace and then use the Vibe function to parameterize the burn rate of the combusted charge. If the mass fraction burned trace is known, as for simulations, the pressure ratio management is not used.

A.3.1 Matekunas pressure ratio

The pressure ratio management was developed by Matekunas [1983] and was described earlier in section 2.4. It is defined as the ratio of the cylinder pressure from a firing cycle $p(\theta)$ and the corresponding motored cylinder pressure $p_m(\theta)$:

$$PR(\theta) = \frac{p(\theta)}{p_m(\theta)} - 1 \quad (\text{A.10})$$

The mass fraction burned trace x_b is then approximated by the normalized pressure ratio $PR_N(\theta)$

$$x_b(\theta) \approx PR_N(\theta) = \frac{PR(\theta)}{\mathbf{max}PR(\theta)} \quad (\text{A.11})$$

an approximation valid within 1-2 degrees [Eriksson, 1999].

A.3.2 Vibe function

The Vibe function [Vibe, 1970] is often used as a parameterization of the mass fraction burned x_b , and it has the following form

$$x_b(\theta) = 1 - e^{-a\left(\frac{\theta - \theta_{ig}}{\Delta\theta}\right)^{m+1}} \quad (\text{A.12})$$

The burn rate is given by its differentiated form

$$\frac{dx_b(\theta)}{d\theta} = \frac{a(m+1)}{\Delta\theta} \left(\frac{\theta - \theta_{ig}}{\Delta\theta}\right)^m e^{-a\left(\frac{\theta - \theta_{ig}}{\Delta\theta}\right)^{m+1}} \quad (\text{A.13})$$

where θ_{ig} is the start of the combustion, $\Delta\theta$ is the total combustion duration, and a and m are adjustable parameters. The Vibe function was described earlier in section 3.5, and there it is given how to relate the parameters a and m to the physical burn angle parameters θ_d and θ_b using (3.19).

The differentiated Vibe function (A.13) is used to produce a mass fraction burned trace, i.e. a normalized heat-release trace. The absolute value of the heat-release rate $\frac{dQ_{ch}}{d\theta}$ is given by the fuel mass m_f , the specific heating value of the fuel q_{HV} , and combustion efficiency η_f as

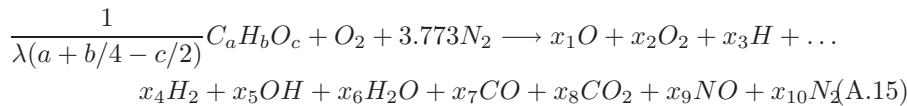
$$\frac{dQ_{ch}}{d\theta} = m_f q_{HV} \eta_f \frac{dx_b}{d\theta} = Q_{in} \frac{dx_b}{d\theta} \quad (\text{A.14})$$

where Q_{in} represents the total energy released from combustion.

Summing up, the combustion process is described by (A.14), parameterized by Q_{in} , θ_{ig} , θ_d , and θ_b .

A.4 Fuel composition sensitivity of γ

So far, the focus has only been on iso-octane C_8H_{18} as the fuel used. Since the actual fuel composition can differ quite extensively over both region and time of year, it is interesting to see what happens with the specific heat ratios when the fuel composition is changed. Consider the general fuel $C_aH_bO_c$, which is combusted according to



where a , b and c are positive integers.

First our attention is turned to the properties of hydrocarbons and then to a few alcohols, when considering burned mixtures. Then a similar investigation is made for unburned mixtures. Finally the properties of partially burned mixtures and their influence on the cylinder pressure are examined.

Fuel	C_aH_b	y	NRMSE @ p_1		NRMSE @ p_2	
			A	B	A	B
Methane	CH_4	4	0.19 %	0.17 %	0.16 %	0.15 %
Iso-octane	C_8H_{18}	2.25	0	0	0	0
Gasoline1	$C_{8.26}H_{15.5}$	1.88	0.06 %	0.05 %	0.05 %	0.04 %
Gasoline2	$C_{7.76}H_{13.1}$	1.69	0.09 %	0.07 %	0.07 %	0.07 %

Table A.1: Burned mixtures: Different fuels and their chemical composition. The NRMSE is formed as the difference compared to iso-octane, and evaluated at $\lambda = 1$ and temperature regions A and B , for $p_1 = 7.5$ and $p_2 = 35$ bar respectively.

A.4.1 Hydrocarbons

Considering hydrocarbons C_aH_b only ($c = 0$), the hydrocarbon ratio $y = b/a$ will determine the properties of the air-fuel mixture, since the a and b are only relative proportions on a molar basis [Heywood, 1988][p.69]. The specific heat ratio is computed using CHEPP for the fuels given in table A.1. Gasoline 1 and 2 are commercial fuels listed in Heywood [1988][p.133]. The fuels methane and gasoline2 will be extreme points in our study, considering the hydrocarbon ratio y , in a region which covers most hydrocarbon fuels. In the upper plot of figure A.2 the specific heat ratio for the fuels are displayed. The difference between the fuels is hardly visible. Therefore, the fuels are compared to iso-octane, and the difference in γ is plotted in the lower part of figure A.2.

The difference is small, and smallest for the commercial gasoline as expected, since the hydrocarbon ratio y does not differ as much. The NRMSE are found in table A.1, for $p_1 = 7.5$ and $p_2 = 35$ bar respectively. Compared to table 4.5, the fuel composition introduces a smaller error in γ than the Krieger-Borman polynomial. It is therefore possible that the iso-octane γ can be used as a good approximation for the other hydrocarbon fuels, described by C_aH_b .

A.4.2 Alcohols

Considering more general fuels such as alcohols, the specific heat ratio of methanol CH_3OH is computed and compared to the ones found for iso-octane and methane respectively. The comparison with methane shows what influence the extra oxygen atom brings about, and the comparison with iso-octane yields the difference to the fuel used here as a reference fuel. The results are displayed in figure A.3, the upper plot shows γ for the three fuels listed in table A.2. The lower plot shows the difference in γ for methanol when compared to iso-octane and methane respectively. Surprisingly, the difference is smaller for iso-octane, which is also concluded by comparing the NRMSE:s from table A.2. These NRMSE:s are in fact quite large, which is found by comparing to the ones found in table 4.5. This suggests that the fault introduced by using the iso-

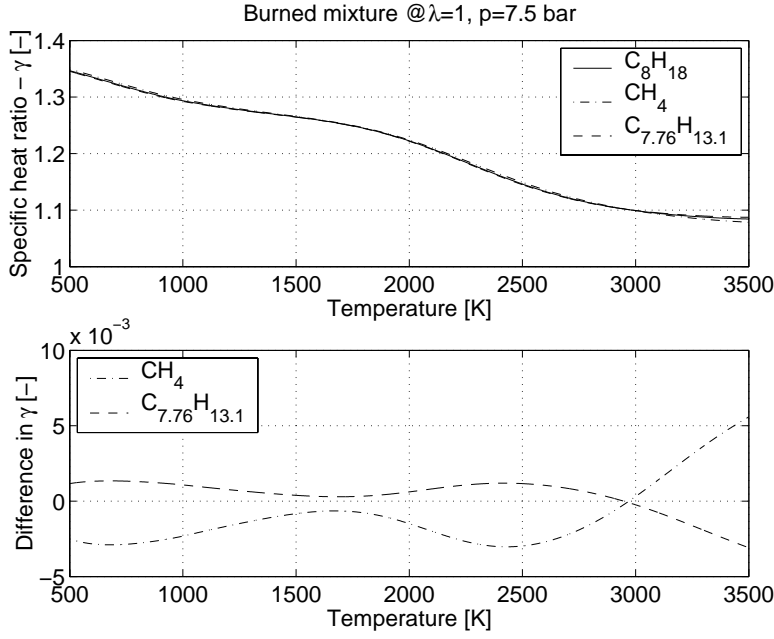


Figure A.2: *Upper*: Specific heat ratio for various fuels. *Lower*: Difference in γ for methane CH_4 and gasoline2 $C_{7.76}H_{13.1}$, compared to iso-octane C_8H_{18} .

Fuel	$C_aH_bO_c$	NRMSE @ p_1		NRMSE @ p_2	
		A	B	A	B
Methanol	CH_4O	0	0	0	0
Methane	CH_4	0.80 %	0.75 %	0.81 %	0.72 %
Iso-octane	C_8H_{18}	0.73 %	0.60 %	0.70 %	0.60 %

Table A.2: Burned mixtures: Different fuels and their chemical composition. The NRMSE is formed as the difference for methanol compared to methane and iso-octane respectively, and evaluated at $\lambda = 1$ and temperature regions A and B , for $p_1 = 7.5$ and $p_2 = 35$ bar respectively.

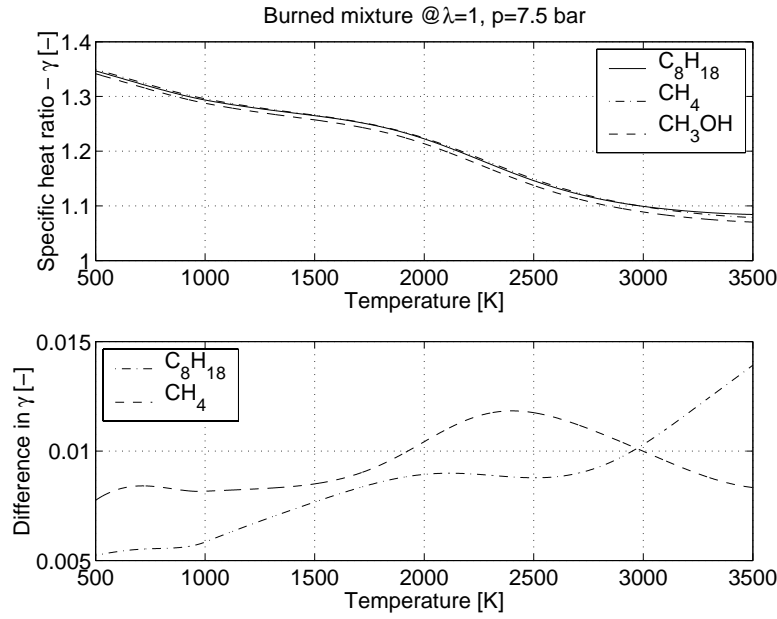


Figure A.3: *Upper:* Specific heat ratio for various fuels. *Lower:* Difference in γ for methanol CH_3OH compared to iso-octane C_8H_{18} and methane CH_4 .

octane γ to describe the methanol γ is too large. This means that the results are not valid for alcohols. Instead, new coefficient values in the polynomials have to be estimated.

A.4.3 Unburned mixtures

The specific heat ratios for both unburned hydrocarbons and alcohols are analyzed in a similar manner as for the burned mixtures presented earlier. The results are summarized in table A.3. All fuels but methane are captured fairly well by the reference fuel iso-octane. Comparing with the linear model of the unburned mixture given in table 4.2, gasoline1 introduces a NRMSE which is in the same order. A trend in the results shows that for hydrocarbons, the specific heat ratio is more accurately determined for burned mixtures than unburned. This conclusion can be drawn by comparing tables A.1 and A.3. For the alcohol methanol it is the other way around, compare tables A.2 and A.3.

Fuel	$C_aH_bO_c$	$y = b/a$	NRMSE
Methane	CH_4	4	2.57 %
Iso-octane	C_8H_{18}	2.25	0
Gasoline1	$C_{8.26}H_{15.5}$	1.88	0.18 %
Gasoline2	$C_{7.76}H_{13.1}$	1.69	0.39 %
Methanol	CH_3OH	4	0.50 %

Table A.3: Unburned mixtures: Different fuels and their chemical composition. The NRMSE is formed as the difference compared to iso-octane, and evaluated at $\lambda = 1$.

Fuel	NRMSE: γ [%]	RMSE: p [kPa]	MRE: γ [%]
Methane	2.0	36.6	2.8
Iso-octane	0.0	0.0	0.0
Gasoline1	0.12	2.2	0.20
Gasoline2	0.29	5.3	0.40
Methanol	0.63	5.1	0.85

Table A.4: Evaluation of the impact on cylinder pressure and specific heat ratio for various fuels using iso-octane as reference fuel, for the simulated cylinder pressure in figure 4.8.

A.4.4 Partially burned mixture – influence on cylinder pressure

The cylinder pressure given in figure 4.8 is used to exemplify the impact a certain fuel has on the cylinder pressure, given that all the other operating conditions are the same. The reference model (4.14) is used to model γ . The impact is displayed as the RMSE for the pressure in table A.4, as well as the NRMSE and MRE for γ . Iso-octane is used as the reference fuel. Compared to table 4.6, the cylinder pressure impact (RMSE(p)) of the fuels listed in table A.4 are larger than the impact of \mathcal{D}_1 , see the RMSE(p) column in table 4.6, for all fuels except gasoline1. The RMSE(p) introduced is increased with less than 75 % compared to iso-octane, which is acceptable. This suggests that the iso-octane γ can not be used as a good approximation for all the other hydrocarbon fuels, but fairly well for gasoline1. However, the closer the hydrocarbon ratio y is to the one for iso-octane, the better the approximation will be. Note that if only the accuracy of the γ -models were to be compared, both gasoline1 and 2 would be more accurate than \mathcal{D}_1 . Then a false conclusion would be drawn, since gasoline2 impose a larger fault in cylinder pressure than \mathcal{D}_1 does.

A.5 Altered crevice term

The energy term describing the energy lost when a mass element enters the crevice volume depends on which γ -model is used and therefore has to be restated for every γ -model except \mathcal{B}_1 , which was done in (2.30) for the original setting in the Gatowsk et.al. model. For model \mathcal{D}_1 , the energy term $u' - u$ in (2.30) is therefore rewritten as:

$$\begin{aligned} u' - u &= \int_T^{T'} c_v dT \\ &= x_b \int_T^{T'} c_{v,b}^{KB} dT + (1 - x_b) \int_T^{T'} c_{v,u}^{lin} dT \\ &= x_b (u^{KB}(T') - u^{KB}(T)) + (1 - x_b) \frac{R}{b^u} \ln \left(\frac{\gamma_{lin}^u(T') - 1}{\gamma_{lin}^u(T) - 1} \right) \end{aligned} \quad (\text{A.16})$$

where we have used that $c_v = x_b c_{v,b}^{KB} + (1 - x_b) c_{v,u}^{lin}$ in the second equality, and in the third equality that $c_v = \left(\frac{\partial u}{\partial T}\right)_V$ for the burned mixture and (2.28) for the linear unburned mixture. The first term in (A.16) is given directly by the Krieger-Borman polynomial in its original form. The second term is easily computed when knowing the coefficient values for the linear unburned mixture model, i.e.

$$\gamma_{lin}^u = \gamma_{300}^u + b^u (T - 300) \quad (\text{A.17})$$

Note that (A.16) is zero whenever $T' = T$, i.e. when the mass flow is out of the modeled crevice volume.

A.6 Thermodynamic properties for burned mixture

This section entails further details on thermodynamic properties for the burned mixture. The focus is on approximative models for the specific heats. As mentioned in section 4.6, there is a potential of improving the Krieger-Borman polynomial. Here it will be shown why. Figure A.4 displays the reference specific heat $c_{v,b}$ as well as the two approximations, i.e. the linear and the Krieger-Borman model respectively. The linear approximation has bad performance over the entire temperature region, and does not capture non-linear behavior of the reference model very well. The Krieger-Borman polynomial fits the reference model quite well for $T < 2800$ K, but for higher temperatures the fit is a lot worse. This is reflected in table A.5, which displays the maximum relative error (MRE) and normalized root mean square error (NRMSE) for a number of temperature regions.

For temperature regions B-E, the NRMSE for $c_{v,b}^{KB}$ is immensely lower than for region A, which verifies that the Krieger-Borman polynomial works well for temperatures below 3000 K. Actually the Krieger-Borman polynomial has poorer performance than the linear model for high temperatures, as seen by comparing the NRMSE:s for temperature region A. This shows that there is

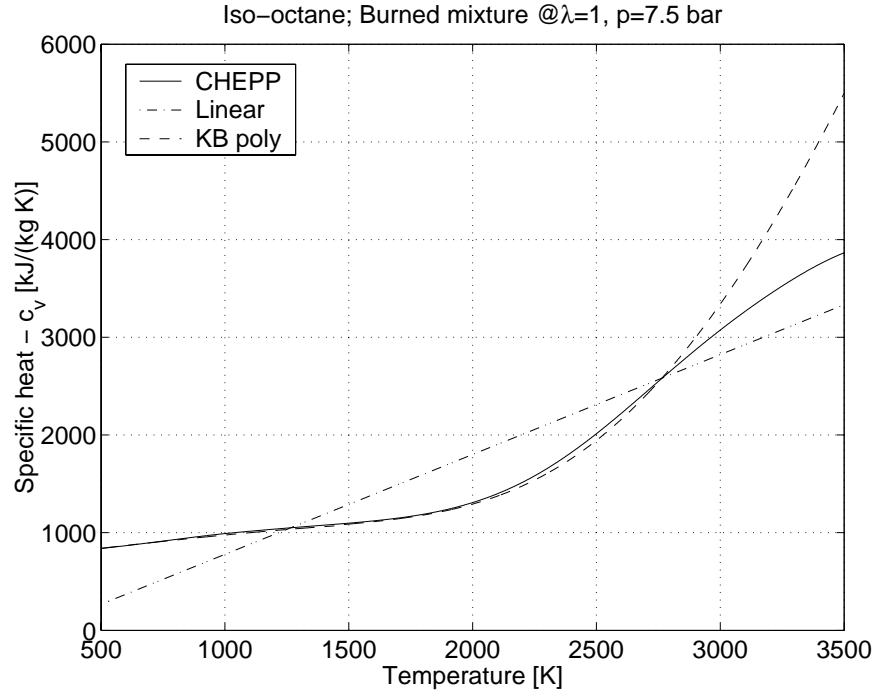


Figure A.4: Specific heat $c_{v,b}$ for burned stoichiometric mixture using CHEPP, the corresponding linear function $c_{v,b}^{lin}$ and $c_{v,b}^{KB}$ found using the Krieger-Borman polynomial.

Region	$T \in$	$c_{v,b}^{lin}$		$c_{v,b}^{KB}$	
		MRE	NRMSE	MRE	NRMSE
A	[500, 3500]	0.68 %	0.20 %	0.42 %	0.21 %
B	[500, 3000]	0.68 %	0.23 %	0.09 %	0.03 %
C	[500, 2700]	0.68 %	0.27 %	0.04 %	0.02 %
D	[500, 2500]	0.68 %	0.30 %	0.04 %	0.02 %
E	[1200, 3000]	0.38 %	0.20 %	0.09 %	0.04 %

Table A.5: Maximum relative error (MRE) and normalized root mean square error (NRMSE) of specific heat $c_{v,b}$ for different temperature regions at $\lambda = 1$ and $p = 7.5$ bar.

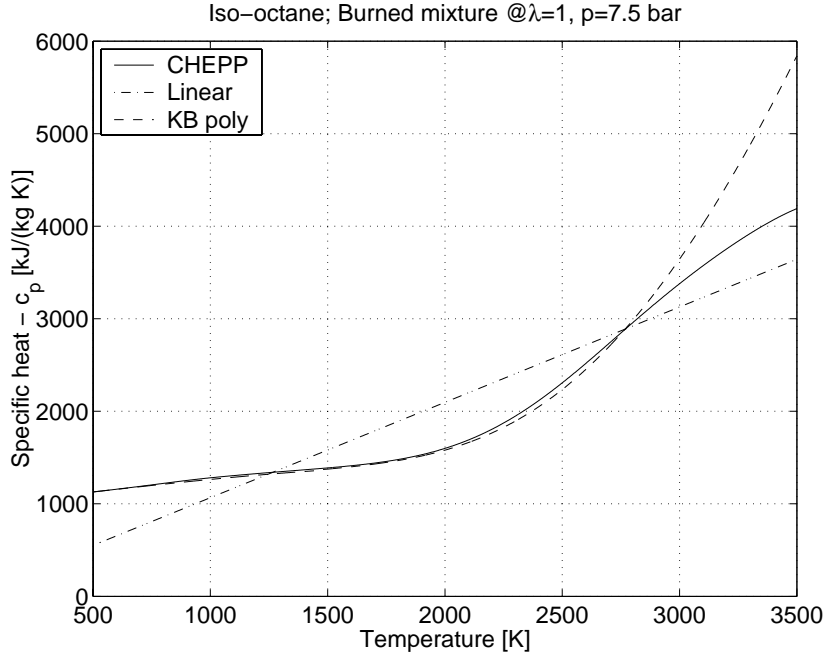


Figure A.5: Specific heat $c_{p,b}$ for burned stoichiometric mixture using CHEPP, the corresponding linear function $c_{p,b}^{lin}$ and $c_{p,b}^{KB}$ found using the Krieger-Borman polynomial.

a potential of enhancing the Krieger-Borman polynomial, at least for temperatures above 3000 K.

The corresponding results for specific heat $c_{p,b}$ are shown in figure A.5 and table A.6.

Region	$T \in$	$c_{v,b}^{lin}$		$c_{v,b}^{KB}$	
		MRE	NRMSE	MRE	NRMSE
A	[500, 3500]	0.51 %	0.17 %	0.39 %	0.19 %
B	[500, 3000]	0.51 %	0.19 %	0.08 %	0.03 %
C	[500, 2700]	0.51 %	0.23 %	0.03 %	0.02 %
D	[500, 2500]	0.51 %	0.25 %	0.03 %	0.02 %
E	[1200, 3000]	0.31 %	0.17 %	0.08 %	0.03 %

Table A.6: Maximum relative error (MRE) and normalized root mean square error (NRMSE) of specific heat $c_{p,b}$ for different temperature regions at $\lambda = 1$ and $p = 7.5$ bar.

OP	p_{IVC} [kPa]	T_{IVC} [K]	Q_{in} [J]
1	25	372	330
2	50	341	760
3	100	327	1620
4	150	326	2440
5	200	325	3260
1	25	372	330
6	50	372	700
7	100	372	1420
8	150	372	2140
9	200	372	2850

Table A.7: Operating points (OP) for the simulated cylinder pressure.

A.7 Thermodynamic properties for partially burned mixture

In this section the operating points (OP) for the simulated cylinder pressure traces used to evaluate the proposed γ -models are given in table A.7. In operating points 1-9 the mean charge temperature at IVC, T_{IVC} , is computed as a function of exhaust pressure p_{exh} (3.14). The released energy Q_{in} is computed as in (3.22), where the residual gas ratio x_r is found from (3.13). The cylinder pressure at IVC, p_{IVC} , here ranges from 25 kPa up to 200 kPa, i.e. from low intake pressure to a highly supercharged pressure. The values of the parameters in the single-zone heat release model are given in table 3.2. The corresponding cylinder pressures during the closed part of the cycle are shown in figure A.6, where the upper figure shows the cylinder pressure for operating points 1-5, and the lower plot displays operating point 1 and 6-9.

The results from applying operating points 1-9 to the approximative γ -models are summarized in the following tables and figures; Tables A.8 and A.10 summarizes the normalized root mean square error and maximum relative error in specific heat ratio γ , table A.9 summarizes the root mean square error for the cylinder pressure p . Figures A.7 to A.10 displays the approximative γ -models and the reference γ -model as function of crank angle degree and single zone temperature respectively, for the cylinder pressure trace given in figure 4.8. Figures A.11 and A.12 illustrates the corresponding cylinder pressure errors introduced by the model error each γ -model brings along.

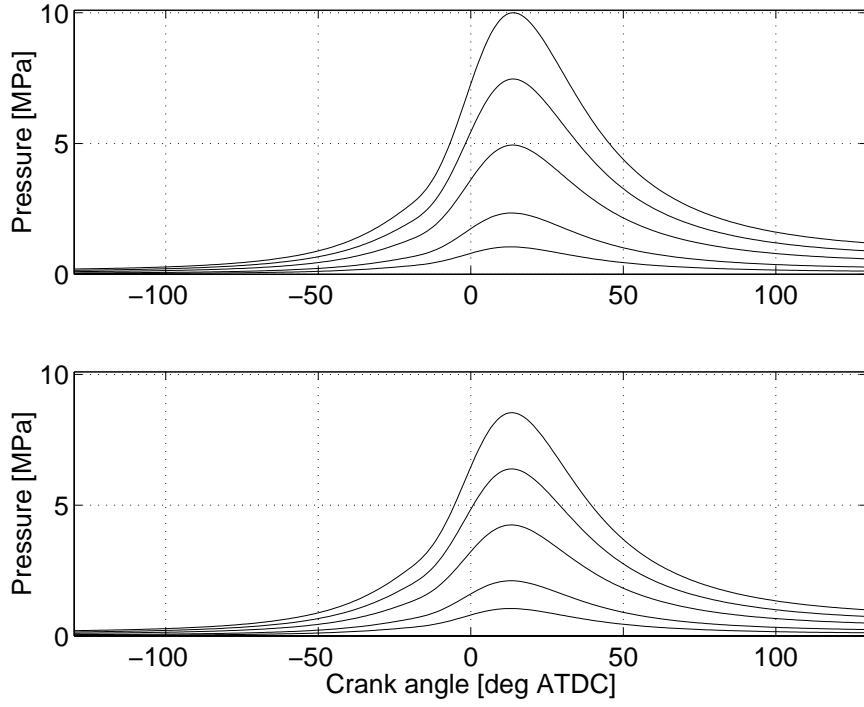


Figure A.6: *Upper*: Simulated cylinder pressure for operating points 1-5. *Lower*: Simulated cylinder pressure for operating points 1 and 6-9.

OP	\mathcal{B}_1	\mathcal{B}_2	\mathcal{B}_3	\mathcal{B}_4	\mathcal{C}_1	\mathcal{C}_2	\mathcal{C}_3	\mathcal{C}_4	\mathcal{C}_5	\mathcal{D}_1	\mathcal{D}_2	\mathcal{D}_3
1	1.4	2.6	1.8	4.2	0.62	4.1	0.59	0.52	1.5	0.11	0.1	0.016
2	1.3	2.7	1.8	4.5	0.69	4.1	0.65	0.58	1.5	0.098	0.094	0.014
3	1.2	2.6	1.7	4.6	0.82	4	0.62	0.55	1.6	0.095	0.091	0.014
4	1.2	2.4	1.6	4.5	0.93	3.9	0.58	0.5	1.7	0.096	0.091	0.014
5	1.1	2.4	1.6	4.4	1	3.8	0.56	0.47	1.7	0.097	0.092	0.014
1	1.4	2.6	1.8	4.2	0.62	4.1	0.59	0.52	1.5	0.11	0.1	0.016
6	1.2	2.4	1.7	4.1	0.57	4	0.51	0.44	1.6	0.098	0.092	0.017
7	1.1	2.3	1.6	4	0.69	3.8	0.44	0.38	1.6	0.094	0.088	0.017
8	1.1	2.2	1.5	3.9	0.81	3.8	0.4	0.34	1.7	0.092	0.086	0.017
9	1	2.1	1.5	3.9	0.91	3.7	0.38	0.32	1.8	0.092	0.086	0.017
Mean	1.2	2.4	1.7	4.2	0.77	3.9	0.53	0.46	1.6	0.097	0.092	0.016

Table A.8: Normalized root mean square error (NRMSE) [%] for γ -models.

OP	\mathcal{B}_1	\mathcal{B}_2	\mathcal{B}_3	\mathcal{B}_4	\mathcal{C}_1	\mathcal{C}_2	\mathcal{C}_3	\mathcal{C}_4	\mathcal{C}_5	\mathcal{D}_1	\mathcal{D}_2	\mathcal{D}_3
1	26.1	37.3	33.3	29.5	17.2	61.6	9.7	8.6	34.2	1.3	1.2	0.1
2	52.3	85.8	76.0	62.8	39.8	140.7	25.4	22.8	82.9	2.8	2.6	0.3
3	98.4	172.5	152.9	125.7	74.1	289.4	53.3	47.3	192.3	5.9	5.3	0.7
4	135.1	248.8	221.0	180.3	98.4	427.0	76.7	67.3	305.4	9.2	8.2	1.0
5	168.1	321.7	286.3	232.3	118.9	561.7	99.0	86.0	422.8	12.5	11.2	1.4
1	28.7	37.3	33.3	29.5	17.2	61.6	9.7	8.6	34.2	1.3	1.2	0.1
6	42.0	70.0	62.7	49.6	28.5	120.0	17.5	15.2	75.2	2.5	2.2	0.3
7	73.1	130.9	117.7	91.5	45.3	233.2	31.4	26.9	163.5	4.9	4.3	0.7
8	100.3	188.4	169.8	130.7	58.0	343.9	44.3	37.5	256.4	7.4	6.4	1.1
9	125.1	243.7	220.2	168.4	68.2	453.0	56.6	47.4	352.2	9.9	8.5	1.5
Mean	84.9	153.6	137.3	110.0	56.6	269.2	42.4	36.7	191.9	5.8	5.1	0.7

Table A.9: Root mean square error (RMSE) [kPa] for cylinder pressure.

OP	\mathcal{B}_1	\mathcal{B}_2	\mathcal{B}_3	\mathcal{B}_4	\mathcal{C}_1	\mathcal{C}_2	\mathcal{C}_3	\mathcal{C}_4	\mathcal{C}_5	\mathcal{D}_1	\mathcal{D}_2	\mathcal{D}_3
1	4.1	5.9	5.2	7.7	2.3	7.3	2.2	2.1	8.1	0.29	0.28	0.049
2	4.1	5.9	5.2	7.8	2.3	7.3	2.4	2.3	8.4	0.27	0.26	0.039
3	3.6	5.5	4.7	7.4	1.9	6.9	2.3	2.1	8.6	0.26	0.25	0.036
4	3.3	5.1	4.4	7.2	1.8	6.5	2.1	1.9	8.6	0.26	0.25	0.036
5	3.1	4.9	4.1	7	2.1	6.3	2	1.8	8.7	0.26	0.25	0.036
1	4.1	5.9	5.2	7.7	2.3	7.3	2.2	2.1	8.1	0.29	0.28	0.049
6	3.5	5.3	4.6	7.2	1.7	6.7	1.8	1.7	8.1	0.26	0.25	0.049
7	3	4.8	4.1	6.7	1.4	6.2	1.5	1.5	8.1	0.24	0.24	0.05
8	2.7	4.5	3.8	6.4	1.7	5.9	1.4	1.3	8.1	0.24	0.23	0.05
9	2.5	4.2	3.6	6.2	2	5.7	1.3	1.2	8.1	0.23	0.22	0.05
Mean	3.4	5.2	4.5	7.1	1.9	6.6	1.9	1.8	8.3	0.26	0.25	0.044

Table A.10: Maximum relative error (MRE) [%] for γ .

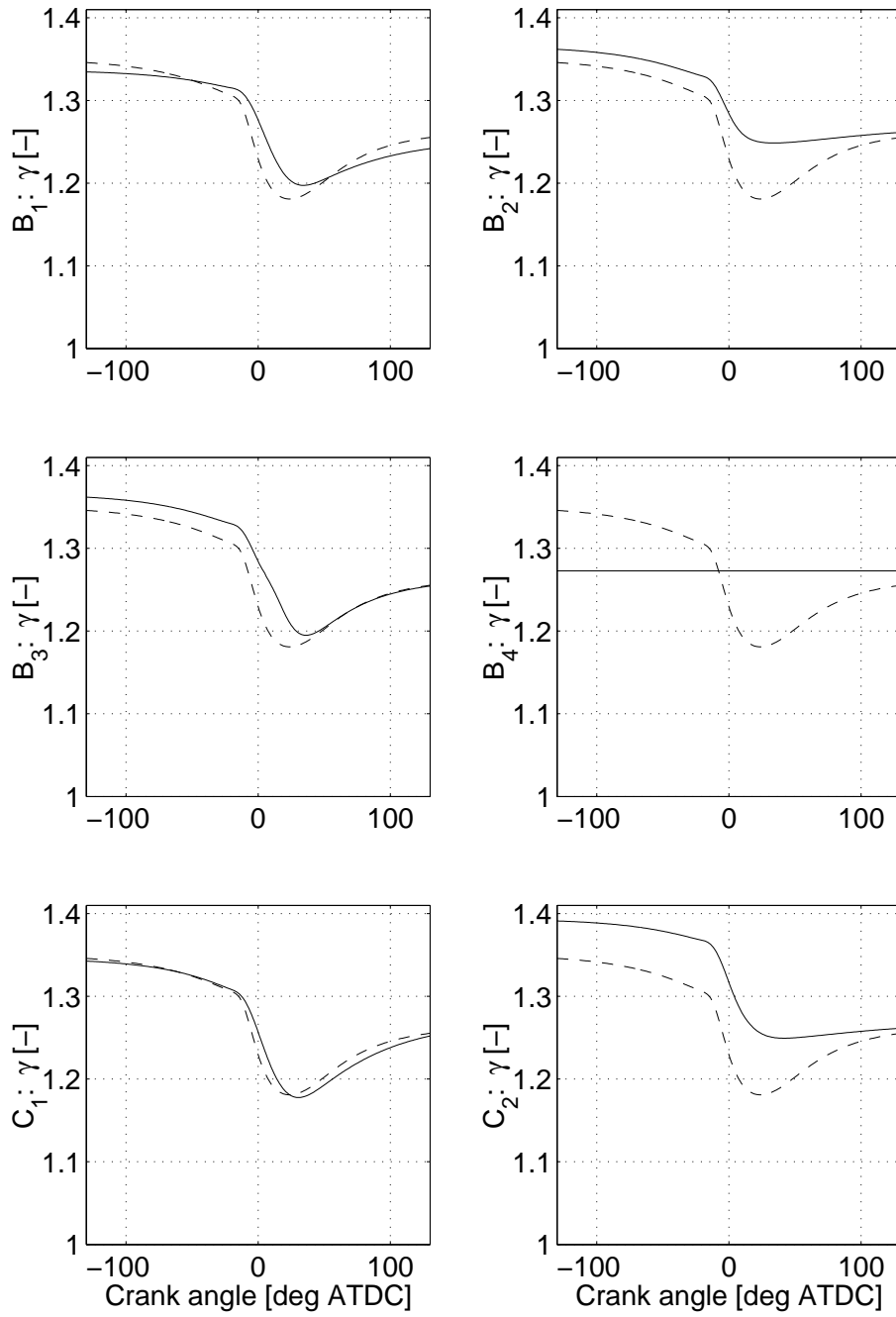


Figure A.7: Specific heat ratio γ for models B_1 to C_2 (solid line) at operating point 2 given in table A.7. The dashed line corresponds to the reference model D_4 found by CHEPP.

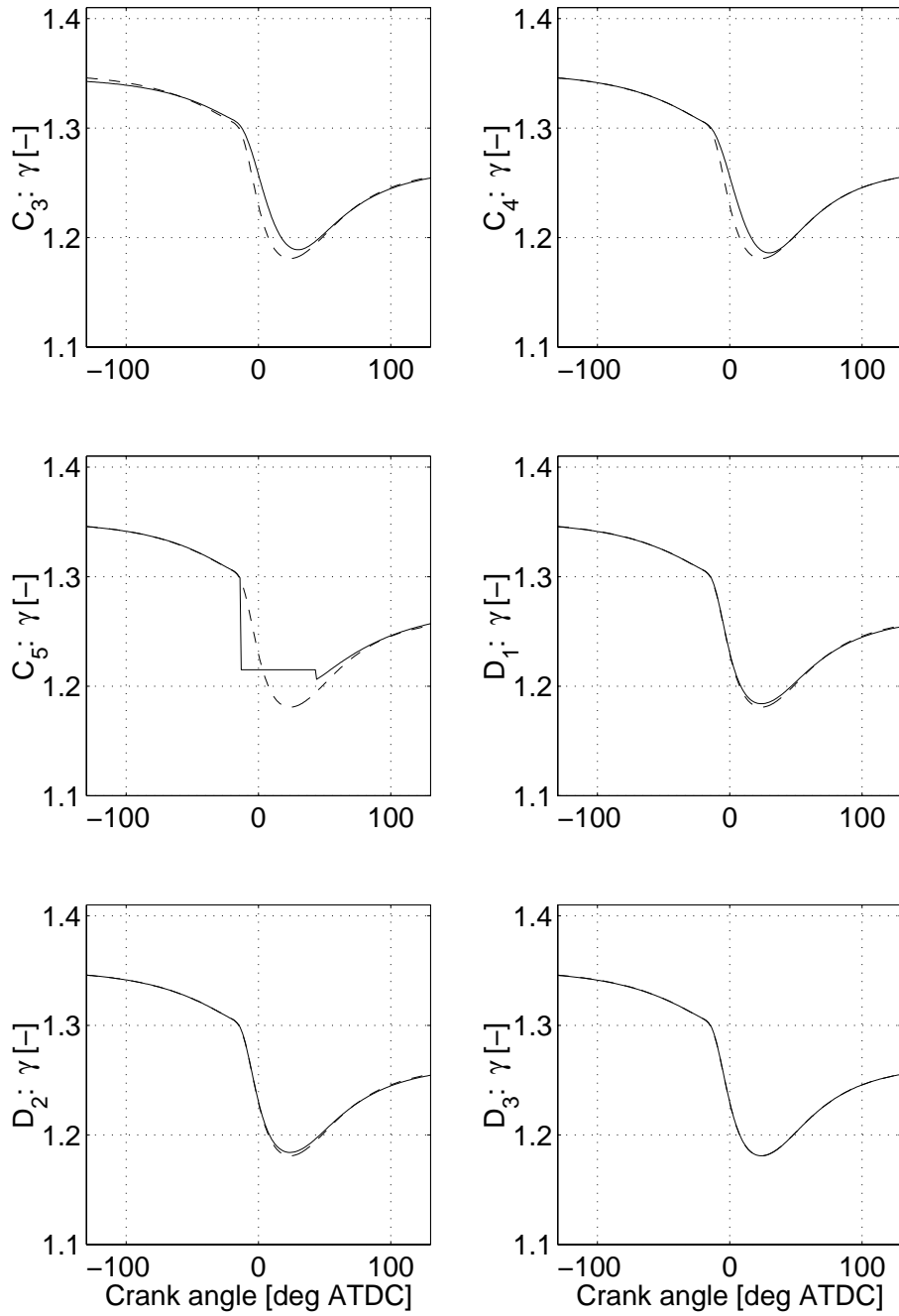


Figure A.8: Specific heat ratio γ for models C_3 to D_3 (solid line) at operating point 2 given in table A.7. The dashed line corresponds to the reference model D_4 found by CHEPP.

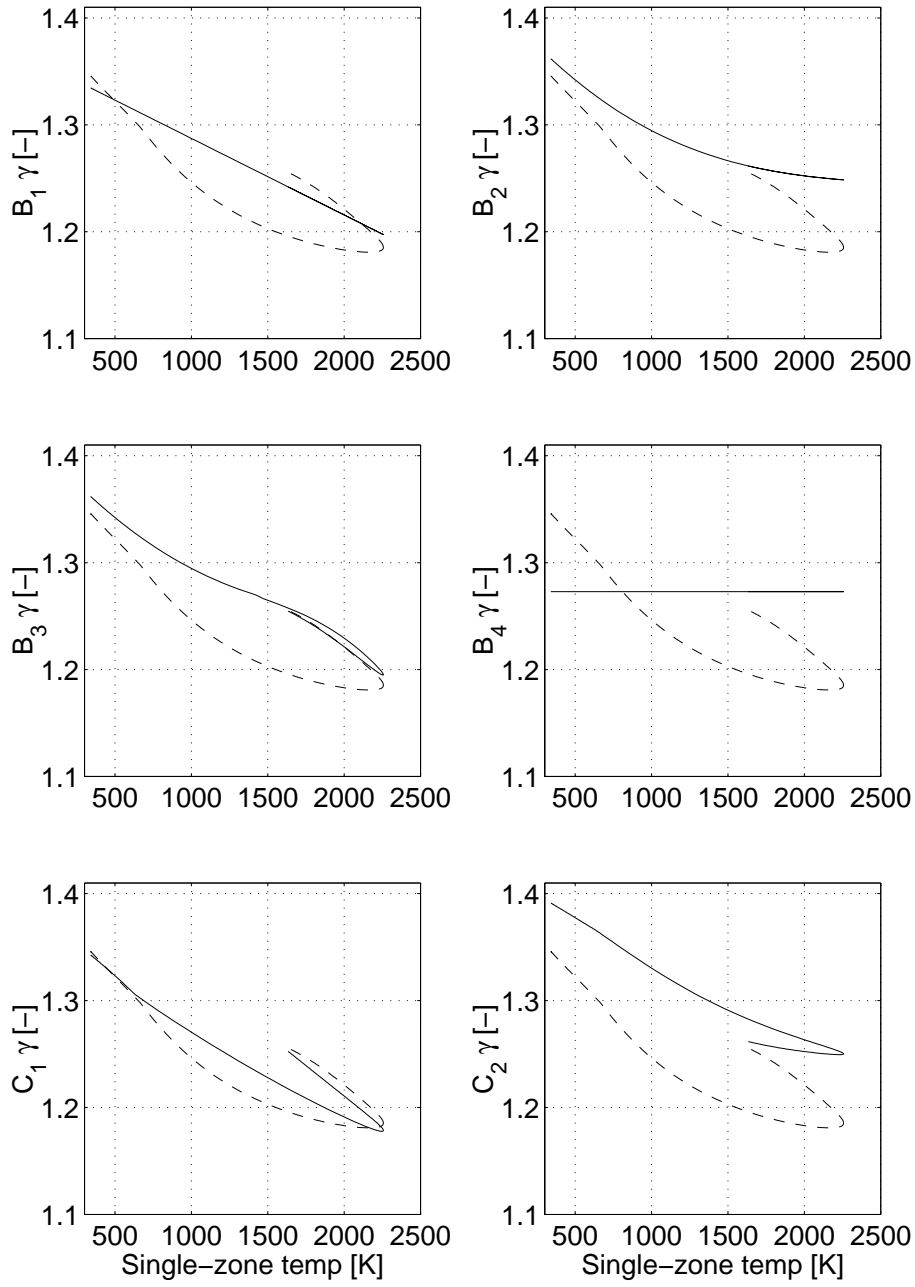


Figure A.9: Specific heat ratio γ for models B_1 to C_2 (solid line) at operating point 2 given in table A.7. The dashed line corresponds to the reference model D_4 found by CHEPP.

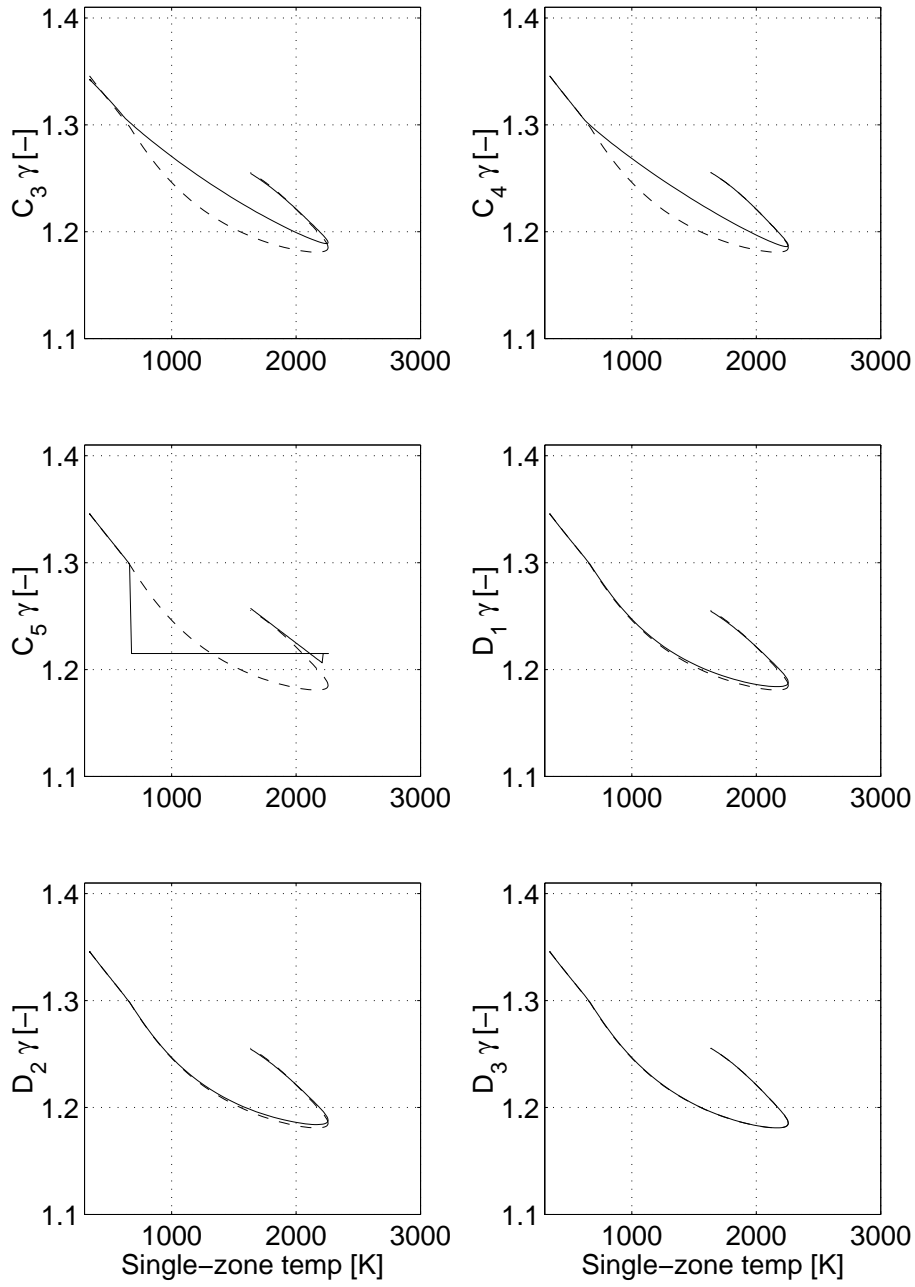


Figure A.10: Specific heat ratio γ for models C_3 to D_3 (solid line) at operating point 2 given in table A.7. The dashed line corresponds to the reference model D_4 found by CHEPP.

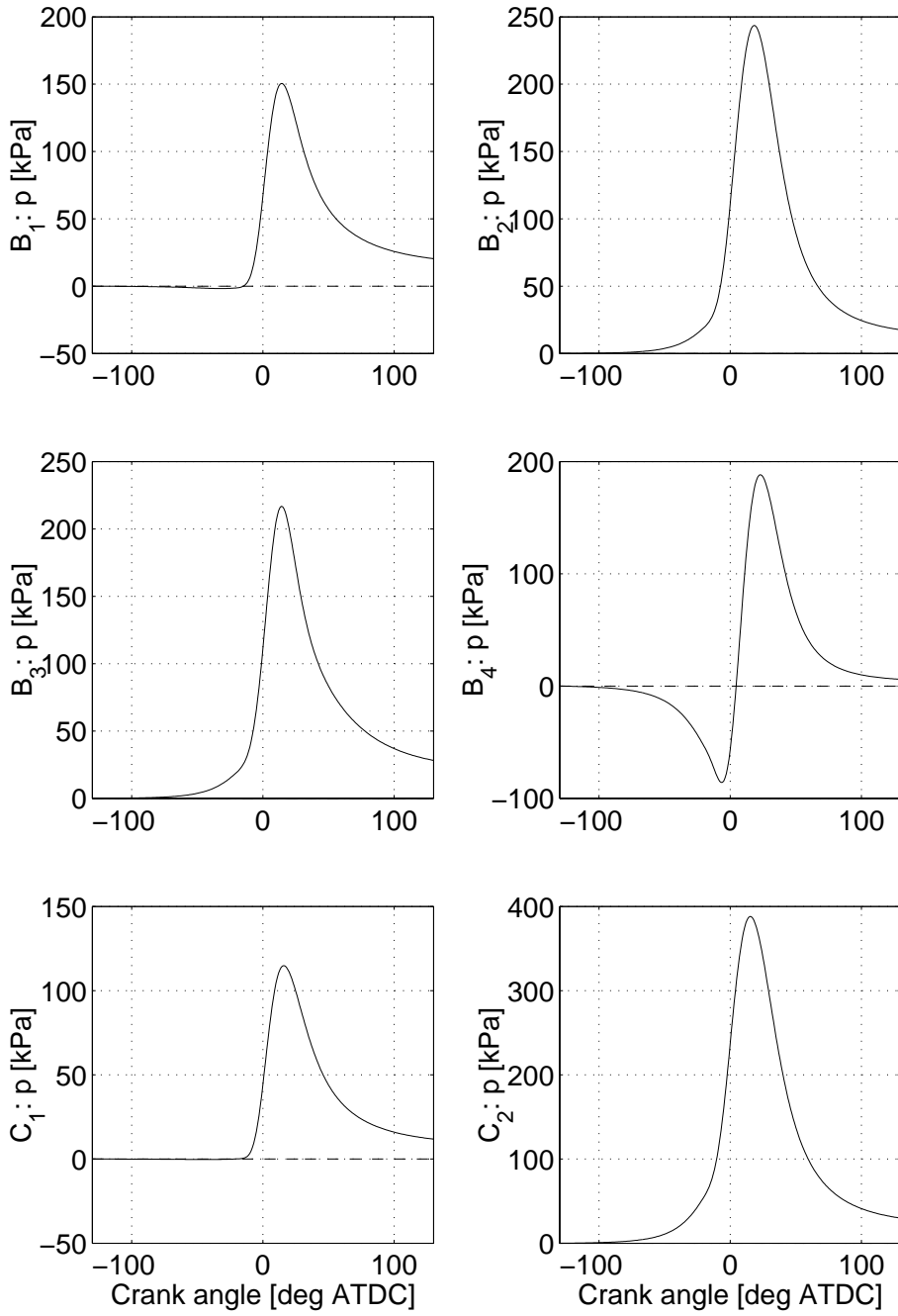


Figure A.11: Cylinder pressure error for models B_1 to C_2 (solid line) at operating point 2 given in table A.7, as compared to the reference model. The reference cylinder pressure is given in figure 4.8.

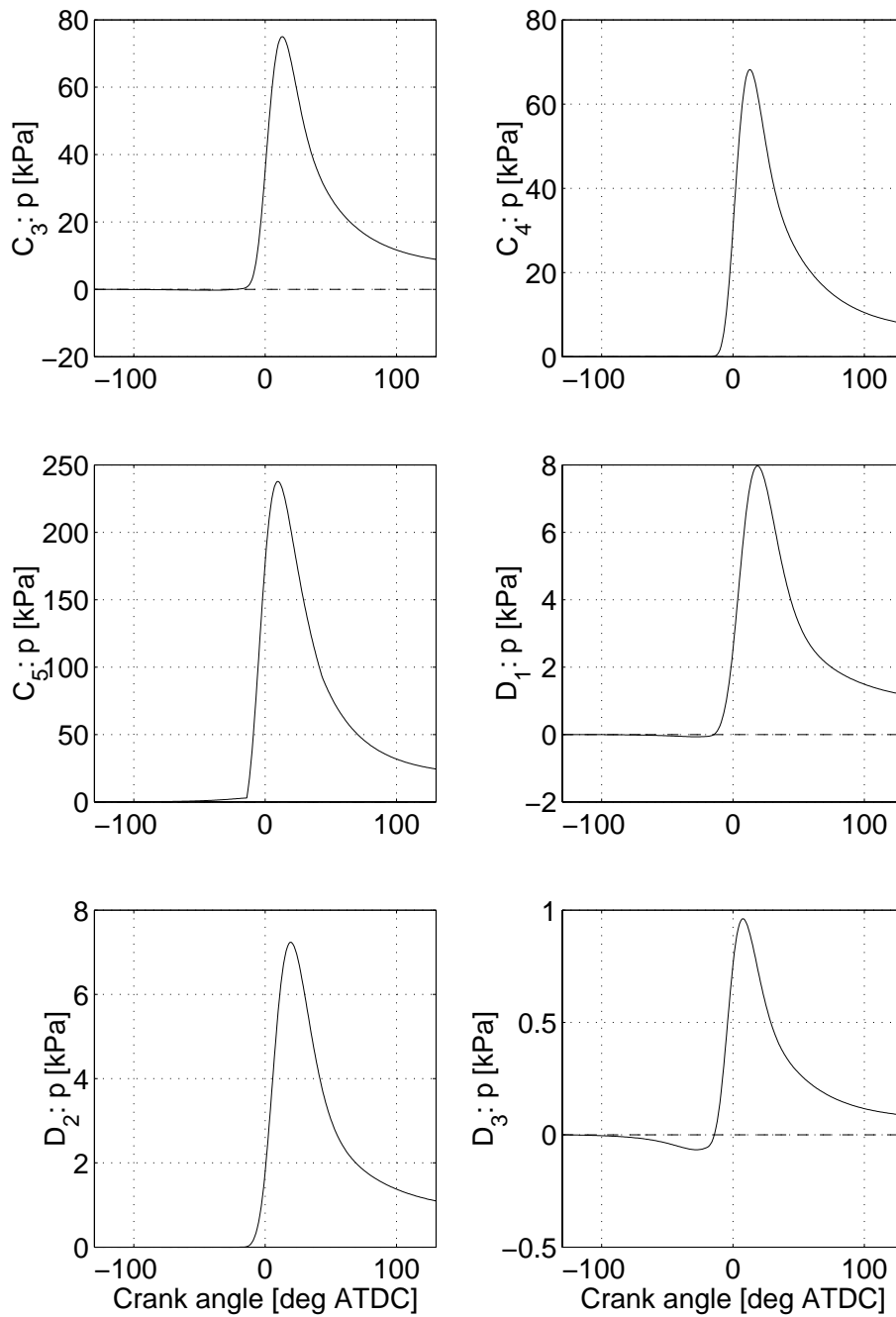


Figure A.12: Cylinder pressure error for models C_3 to D_3 (solid line) at operating point 2 given in table A.7, as compared to the reference model. For convenience, the sign of the pressure error for model C_5 is changed.

COMPRESSION RATIO ESTIMATION – FURTHER DETAILS

Further additional details and argumentation for the results found in chapter 5 are given in this chapter. Each section is referenced from various sections in chapter 5, and this chapter should therefore be seen as a complement.

B.1 Taylor expansions for sublinear approach

As mentioned in section 5.4, the predictor functions used in each of the two substeps of method 1 are unequal in size. This is the section where this statement will be justified and clarified. In substep 1 (5.6), $V_d(\theta, x)$ is a model and $p(\theta)$ is the signal or regressor, where x are the parameters and θ is the crank angle. On the other hand, in substep 2 (5.7) $p(\theta, x)$ is now the model and $V_d(\theta)$ is the signal. Note that for notational convenience, the model for $V_d(\theta)$ is named $\hat{V}_d(\theta, x)$, and is thereby distinguished from the signal $V_{d,s}(\theta)$, and the model $\hat{p}(\theta, x)$ is separated from $p_s(\theta)$ in a likewise manner. The predictor functions for each substep will now be investigated, where the compression ratio estimation and pressure bias estimation are treated as two different cases.

B.1.1 Compression ratio estimation

The predictor functions used for compression estimation using the sublinear approach, also called method 1, are given by (5.6) and (5.7) respectively, and these are rewritten as

$$\hat{V}_d(\theta, x) = C^{1/n} p_s(\theta)^{-1/n} - V_c(r_c) \quad (\text{B.1})$$

and

$$\ln \hat{p}(\theta, x) = \ln C - n \ln(V_{d,s}(\theta) + V_c(r_c)) \quad (\text{B.2})$$

to clarify what is a signal, e.g. p_s , and what is a model, e.g. \hat{p} . The residuals for each substep will now be formed, and these are compared in size. The fact that they are equal in size is a necessity for the method to be successful.

In substep 1, the residual $\varepsilon_1(\theta, x)$ is formed as

$$\varepsilon_1(\theta, x) = \hat{V}_d(\theta, x) - V_{d,s}(\theta) = C^{1/n} p_s(\theta)^{-1/n} - V_c(r_c) - V_{d,s}(\theta) \quad (\text{B.3})$$

using (B.1). The residual for substep 2 is

$$\varepsilon_2(\theta, x) = \ln \hat{p}(\theta, x) - \ln p_s(\theta) \quad (\text{B.4})$$

which is reformulated using (B.2) as

$$\begin{aligned} \varepsilon_2(\theta, x) &= \ln C - n \ln(V_{d,s}(\theta) + V_c(r_c)) - \ln p_s(\theta) \\ &= n \ln \frac{C^{1/n} p_s(\theta)^{-1/n}}{V_{d,s}(\theta) + V_c(r_c)} \\ &= n \ln \frac{C^{1/n} p_s(\theta)^{-1/n} - V_{d,s}(\theta) - V_c(r_c) + V_{d,s}(\theta) + V_c(r_c)}{V_{d,s}(\theta) + V_c(r_c)} \\ &= n \ln \left(1 + \frac{\varepsilon_1(\theta, x)}{V_{d,s}(\theta) + V_c(r_c)} \right) \end{aligned} \quad (\text{B.5})$$

where the last equality is formed using (B.3). Now assuming that $\varepsilon_1 \ll V_c \leq V_{d,s}(\theta) + V_c$ is a valid approximation, a Taylor expansion of (B.5) yields the following approximation of $\varepsilon_2(\theta, x)$:

$$\varepsilon_2(\theta, x) \approx n \frac{\varepsilon_1(\theta, x)}{V_{d,s}(\theta) + V_c(r_c)} \quad (\text{B.6})$$

which relate the two residuals in size. Therefore, if the predictor function for substep 1 is multiplied by n and the predictor function for substep 2 is multiplied by $V_{d,s}(\theta) + V_c(r_c)$, the resulting residuals become equal in size. Note that this works well since n is constant in substep 1 and $V_c(r_c)$ is constant during substep 2.

B.1.2 Pressure bias estimation

The predictor functions used for estimation of an additive pressure sensor bias are given by

$$\hat{p}(\theta, x) = C(V_{d,s}(\theta) + V_c(r_c))^{-n} - \Delta p \quad (\text{B.7})$$

and

$$\ln(\hat{p}(\theta, x) + \Delta p) = \ln C - n \ln(V_{d,s}(\theta) + V_c(r_c)) \quad (\text{B.8})$$

The residuals for each substep will now be formed, and these are compared in size. In substep 1, the residual $\varepsilon_1(\theta, x)$ is formed as

$$\varepsilon_1(\theta, x) = \hat{p}(\theta, x) - p_s(\theta) \quad (\text{B.9})$$

The residual for substep 2 is

$$\begin{aligned} \varepsilon_2(\theta, x) &= \ln(\hat{p}(\theta, x) + \Delta p) - \ln(p_s(\theta) + \Delta p) \\ &= \ln \frac{\hat{p}(\theta, x) + \Delta p}{p_s(\theta) + \Delta p} \\ &= \ln\left(1 + \frac{\hat{p}(\theta, x) - p_s(\theta)}{p_s(\theta) + \Delta p}\right) \\ &= \ln\left(1 + \frac{\varepsilon_1(\theta, x)}{p_s(\theta) + \Delta p}\right) \end{aligned} \quad (\text{B.10})$$

where the last equality is formed using (B.9). Now assuming that $\varepsilon_1 \ll p_s(\theta) + \Delta p$ is a valid approximation, a Taylor expansion of (B.10) yields the following approximation of $\varepsilon_2(\theta, x)$:

$$\varepsilon_2(\theta, x) \approx \frac{\varepsilon_1(\theta, x)}{p_s(\theta) + \Delta p} \quad (\text{B.11})$$

which relate the two residuals in size. Then, if the predictor function for substep 2 is multiplied by $p_s(\theta) + \Delta p$, the resulting residuals become equal in size. Note that this works well since Δp is constant during substep 2.

B.2 Variable Projection Algorithm

A computationally efficient algorithm is described in Björck [1996] and is summarized here. Partition the parameter vector x such that $x = (y \ z)^T$, where $r(y, z)$ is linear in y . Rewrite $r(y, z)$ as

$$r(y, z) = F(z)y - g(z) \quad (\text{B.12})$$

Let $x_k = (y_k, z_k)$ be the current approximation.

1. Solve the linear subproblem

$$\min_{\delta y_k} \|F(z_k)\delta y_k - (g(z_k) - F(z_k)y_k)\|_2 \quad (\text{B.13})$$

and set $x_{k+1/2} = (y_k + \delta y_k, z_k)$.

2. Compute the Gauss-Newton direction p_k at $x_{k+1/2}$, i.e. solve

$$\min_{p_k} \|C(x_{k+1/2})p_k + r(y_{k+1/2}, z_k)\|_2 \quad (\text{B.14})$$

where $C(x_{k+1/2}) = (F(z_k), r_z(y_{k+1/2}, z_k))$ is the Jacobian matrix.

3. Set $x_{k+1} = x_{k+1/2} + \alpha_k p_k$, do a convergence test and return to step 1 if the estimate has not converged. Otherwise return x_{k+1} .

B.2.1 Compression ratio estimation

The polytropic model in (5.5) is rewritten as

$$\ln p(\theta) = C_2 - n \ln(V_d(\theta') + V_c) \quad (\text{B.15})$$

This equation is linear in the parameters $C_2 = \ln C$ and n and nonlinear in V_c and applies to the form given in (B.12). With the notation from the algorithm above, the parameters are $x = (C_2 \ n \ V_c)^T$, where $y = (C_2 \ n)^T$ and $z = V_c$. The measurement vector is formed as $g = -\ln p$ and the regression vector as $F = [-I \ \ln(V_c + V_d(\theta'))]$. The polytropic model in (5.5) could also be rewritten as

$$V_d(\theta) = C_1 p(\theta)^{-1/n} - V_c(r_c) \quad (\text{B.16})$$

This approach is however not as appropriate as the one in (B.15), due to that the parameters $C_1 = C^{1/n}$ and n are coupled.

B.2.2 Pressure bias estimation

The polytropic model in (5.5) is reformulated as

$$p(\theta) = C(V_d(\theta) + V_c)^n - \Delta p \quad (\text{B.17})$$

This equation is linear in the parameters C and Δp and nonlinear in n and applies to the form given in (B.12). The clearance volume V_c is considered to be known. With the notation from the algorithm above, the parameters are $x = (C \ \Delta p \ n)^T$, where $y = (C \ \Delta p)^T$ and $z = n$. The measurement vector is formed as $g = -p$ and the regression vector as $F = [(V_d(\theta) + V_c) \ -I]$.

B.3 Levenberg-Marquardt method

The unknown parameters, here on denoted by $x \in \mathbf{R}^{d \times 1}$, in the models described in chapters 2 and 3, summarized in section 3.9, have to be determined in some way.

The parameters x are estimated by minimizing the difference between the measured cylinder pressure and the modeled cylinder pressure, i.e. by minimizing the prediction error. A Gauss-Newton method called the Levenberg-Marquardt procedure is used to find the parameter estimate \hat{x}_N in methods 3 and 4 for any given number of parameters.

A thorough presentation of the world of system identification is given in Ljung [1999], from which most of the material presented in the subsequent subsections are from. The first subsection states the equations used when minimizing the prediction error when the parameters appear in a nonlinear fashion. The Levenberg-Marquardt procedure is then presented as a special case. The next subsection concerns issues such as stopping criteria, local minimas, scaling of the parameters and asymptotic variance of the estimate.

B.3.1 Minimizing prediction errors using a local optimizer

When the parameters appear in a nonlinear fashion, typically the minimum of the loss function can not be computed analytically as in the linear case. Instead, numerical search routines must be used [Björck, 1996]. Given an observed data set $Z^N = [y(1), u(1), y(2), u(2), \dots, y(N), u(N)]$ of inputs $u(t)$ and outputs $y(t)$, a good model $\mathcal{M}(x)$ describing the data set Z^N is found by minimizing the prediction error

$$\varepsilon(t, x) = y(t) - \hat{y}(t|x), \quad t = 1, 2, \dots, N \quad (\text{B.18})$$

where $y(t)$ is the output of the system and $\hat{y}(t|x)$ is the predicted output of the model $\mathcal{M}(x)$. The prediction error can also be termed residual. The prediction error is minimized by using a norm on $\varepsilon(t, x)$ and minimize the size of it. A quadratic norm is our choice here and it can be written as

$$V_N(x, Z^N) = \frac{1}{N} \sum_{t=1}^N \frac{1}{2} \varepsilon^2(t, x) \quad (\text{B.19})$$

The term V_N is a measure of the validity of $\mathcal{M}(x)$ and is often called loss function or criterion function. A problem on this form is known as “the nonlinear least-squares problem” in numerical analysis [Ljung, 1999, pp.327] and can be solved by an iterative search for minimum, a number of methods are described in e.g. [Björck, 1996]. The estimate \hat{x}_N is defined as the minimizing argument of (B.19):

$$\hat{x}_N(Z^N) = \arg \min_x V_N(x, Z^N) \quad (\text{B.20})$$

The gradient of (B.19) is

$$V'_N(x, Z^N) = \frac{1}{N} \sum_{t=1}^N \psi(t, x) \varepsilon(t, x) \quad (\text{B.21})$$

where $\psi(t, x)$ is the Jacobian vector given by

$$\psi(t, x) = \frac{d}{dx} \varepsilon(t, x) = -\frac{d}{dx} \hat{y}(t|x) = \left[-\frac{\partial \hat{y}(t|x)}{\partial x_1} \quad \dots \quad -\frac{\partial \hat{y}(t|x)}{\partial x_d} \right]^T \quad (\text{B.22})$$

where d are the number of parameters. For our problem, the Jacobian $\psi(t, x)$ is computed numerically with a forward difference approximation, as

$$\frac{\partial \varepsilon(t, x)}{\partial x_j} = \frac{\varepsilon(t, x + \Delta x_j) - \varepsilon(t, x)}{\Delta x_j} \quad (\text{B.23})$$

Computing the central difference approximation instead of the forward one, would cause double the amount of computations. Differentiating the gradient with respect to the parameters yields the Hessian of (B.19) as

$$V''_N(x, Z^N) = \frac{1}{N} \sum_{t=1}^N \psi(t, x) \psi^T(t, x) + \frac{1}{N} \sum_{t=1}^N \psi'(t, x) \varepsilon^T(t, x) \quad (\text{B.24})$$

where $\psi'(t, x) = -\frac{d^2}{dx^2}\hat{y}(t|x)$. It is however quite a computational burden to compute all d^2 terms in $\psi'(t, x)$. An approximation is therefore desirable and it is made reasonable by the following assumption. Assume that at the global minimum x^* , the prediction errors are independent. Thus close to x^* the second sum in (B.24) will be close to zero, thus the following approximation can be made close to optimum [Ljung, 1999, p.328]:

$$V_N''(x, Z^N) \approx \frac{1}{N} \sum_{t=1}^N \psi(t, x)\psi^T(t, x) = H_N(x, Z^N) \quad (\text{B.25})$$

By omitting the second sum in (B.24), the estimate $H_N(x, Z^N)$ is assured to be positive semidefinite, which guarantees convergence to a stationary point. If this stationary point does not give independent prediction errors $\varepsilon(t, x)$, it can not be ascertained that the second term in (B.24) is negligible and therefore (B.25) might be a bad approximation of the Hessian. This can be tested by a whiteness test [Ljung, 1999, p.512] of the prediction errors.

The estimate \hat{x}_N can be found numerically by updating the estimate of the minimizing point \hat{x}_N^i iteratively as

$$\begin{aligned} \hat{x}_N^{i+1}(Z^N) &= \hat{x}_N^i(Z^N) - \mu_N^i [R_N^i(\hat{x}_N^i, Z^N)]^{-1} V_N'(\hat{x}_N^i, Z^N) \\ &= \hat{x}_N^i(Z^N) + d^i(\hat{x}_N^i, Z^N) \end{aligned} \quad (\text{B.26})$$

where i is the i th iterate, d^i is the search direction and R_N^i is the approximate Hessian H_N in (B.25). Finding the estimate \hat{x}_N in this manner is known as a Gauss-Newton method.

Regularization – Levenberg-Marquardt procedure

If the model $\mathcal{M}(x)$ is over-parameterized or the data Z^N not informative enough, this causes an ill-conditioned Jacobian which results in that the approximative Hessian $H_N(x, Z^N)$ may be singular or close to singular. This causes numerical problems when computing the iterative estimates in (B.26), when inverting H_N . One way to avoid this is the Levenberg-Marquardt procedure, which uses

$$R_N^i(\hat{x}_N^i, Z^N, \nu) = H_N^i(\hat{x}_N^i, Z^N) + \nu I \quad (\text{B.27})$$

to regularize the approximation of the Hessian. The iterative parameter estimate \hat{x}_N^i then becomes

$$\begin{aligned} \hat{x}_N^{i+1}(Z^N, \nu) &= \hat{x}_N^i(Z^N) - \mu_N^i [R_N^i(\hat{x}_N^i, Z^N, \nu)]^{-1} V_N'(\hat{x}_N^i, Z^N) \\ &= \hat{x}_N^i(Z^N) + d^i(\hat{x}_N^i, Z^N, \nu) \end{aligned} \quad (\text{B.28})$$

For $\nu > 0$, the Hessian approximation $R_N^i(\hat{x}_N^i, Z^N, \nu)$ is guaranteed to be positive definite. With $\nu = 0$ this is the Gauss-Newton method and by increasing ν the step size is reduced and the search direction d^i is turned towards the gradient, resulting in the steepest descent direction as $\nu \rightarrow \infty$.

Generally it can not be guaranteed that $d^i(\hat{x}_N^i, Z^N, \nu)$ in (B.28) is a descent direction. This can happen if the problem is very non-linear or if the prediction errors are large [Eriksson, 1998]. Our approach here is to start up with a $\nu > 0$, and if $V_N(\hat{x}_N^{i+1}, Z^N) > V_N(\hat{x}_N^i, Z^N)$ occurs, ν is increased and new values of d^{i+1} and \hat{x}_N^{i+1} are computed until d^{i+1} is a descent direction.

Stopping criteria

A stopping criteria must be stated in order for the optimization procedure to terminate. In theory this should be done when the gradient V'_N is zero, so an obvious practical test is to terminate once $\|V'_N\|$ is small enough. Another useful test is to compute the relative difference in loss function V_N between two iterations, and terminate if this difference is less than a given tolerance level. The same approach can be used for the individual parameters. However, it is not so good since parameters can drift with no reduction in loss function. For a problem with two dependent parameters, the minimization can follow a valley in which the loss function stays the same, but the two parameters change. The loss function approach would terminate when the valley is just entered, while the parameter approach will not terminate until the parameters have converged. The algorithm can also terminate after a given maximum number of iterations. Note that all safeguarded algorithms should return estimates that are at least as good as the initial values.

Local minima and initial parameter values

Generally, the optimization procedure converges to a local minima of $V_N(x, Z^N)$, not a global one which of course would be mostly desirable. To find the global minimum, there is usually no other way than to start the iterative optimization routine at different feasible initial values x^{init} and compare the results [Ljung, 1999, p.338]. Therefore, the initial values should be chosen with care. For a physically parameterized model, as the ones in chapter 3, physical insight and some preliminary estimations are required. Good initial values usually lead to fewer iterations and a faster convergence of the optimization procedure, since for instance the Newton-type methods have good local convergence rates, but not necessarily far from optimum. Note that, although the stated optimization problem only has one local minima, i.e. the global one, the function $V_N(x, Z^N)$ can have several local minima due to the noise in the data Z^N .

Scaling of parameters

The optimization method works most properly when the size of the unknown parameters are all in the same order [Gill et al., 1981, p.346]. From table 3.2, where the unknown parameters are summarized, it can be concluded that the expected parameter values range over 10 decades. Therefore a scaling in terms

of a linear transformation of the parameters is introduced,

$$x^s = Dx \quad (\text{B.29})$$

where D is a diagonal matrix with $D_{i,i} = 1/x_i$, $x_i \neq 0$. The gradient of $V_N(x^s, Z^N)$ in the scaled parameters is given by

$$V'_N(x^s, Z^N) = D^{-T} \psi(x) \varepsilon^T(x) = D^{-T} V'_N(x, Z^N) \quad (\text{B.30})$$

since $\psi(t, x^s) = D^{-T} \psi(t, x)$. The linear transformation matrix D is diagonal and invertible, and therefore $D^{-T} = D^{-1}$. The Hessian of $V_N(x^s, Z^N)$ is given by

$$V''_N(x^s, Z^N) = D^{-T} V''_N(x, Z^N) D^{-1} \quad (\text{B.31})$$

since $\psi'(t, x^s) = D^{-T} x D^{-1}$. If the scaling (B.29) is done just at the initialization for x^{init} , this will produce a poor scaling if the Hessian at optimum x^* differs significantly from that at x^{init} [Gill et al., 1981, p.347]. Thus the scaling is done at every iteration to assure that all scaled parameters x^s are equal to one at the beginning of each iteration.

Asymptotic variance and parameter confidence interval

Consider the case when our model $\mathcal{M}(x)$ has the correct model structure and is provided with data Z^N , such that the measured output can be predicted correctly by the model. This would mean that there is no bias in the parameter estimate \hat{x}_N , and thus $\hat{x}_N \rightarrow \hat{x}^*$ asymptotically as the number of data N goes to infinity. It can then be shown [Ljung, 1999, pp.282] that the probability distribution of the random variable $\sqrt{N}(\hat{x}_N - \hat{x}^*)$ converges asymptotically to a Gaussian distribution with zero mean and covariance matrix P . This can be rewritten as

$$(\hat{x}_N - \hat{x}^*) \in AsN\left(0, \frac{P}{N}\right) \quad (\text{B.32})$$

For a quadratic prediction-error criterion the covariance matrix P is estimated by

$$\hat{P}_N = \hat{\lambda}_N \left(\frac{1}{N} \sum_{t=1}^N \psi(t, \hat{x}_N) \psi^T(t, \hat{x}_N) \right)^{-1} = \hat{\lambda}_N (H_N(\hat{x}_N, Z^N))^{-1} \quad (\text{B.33a})$$

$$\hat{\lambda}_N = \frac{1}{N} \sum_{t=1}^N \varepsilon^2(t, \hat{x}_N) \quad (\text{B.33b})$$

for the parameter estimate \hat{x}_N and N data points, where $\hat{\lambda}_N$ is the estimated noise variance and $H_N(\hat{x}_N, Z^N)$ is the approximated Hessian in (B.25). When using scaled parameters according to (B.29), one has to re-scale the Hessian using (B.31) in a straight forward manner.

The result in (B.33) has a natural interpretation. The more data or the less noisier measured output, the more accurate the estimate. Also, since ψ is the gradient of \hat{y} , the asymptotic accuracy of a certain parameter is related to how sensitive the prediction is with respect to this parameter. Therefore, the more or less a parameter affects the prediction, the easier or harder respectively it will be to determine its value [Ljung, 1999, p.284].

The asymptotic covariance in (B.33) can be used to compute confidence intervals for the parameter estimates \hat{x}_N , and thereby give a reliability measure of a particular parameter \hat{x}_N^k . When (B.32) is valid, the $(1 - \alpha)$ -confidence interval for the true parameter \hat{x}^{*k} is formed as [Ljung, 1999, p.302]

$$P(|\hat{x}_N^k - \hat{x}^{*k}| > \alpha) \approx \frac{\sqrt{N}}{\sqrt{2\pi\hat{P}_N^{kk}}} \int_{|y|>\alpha} \exp(-y^2 N/2\hat{P}_N^{kk}) dy \quad (\text{B.34})$$

where \hat{P}_N^{kk} is the k -th diagonal element of \hat{P}_N . From this, it can be stated that the true parameter value \hat{x}^{*k} lies in the interval around the parameter estimate \hat{x}_N^k with a certain significance $1 - \alpha$. The size of the interval is of course determined by α , and for a 95 % confidence interval the limits for parameter \hat{x}_N^k are

$$\hat{x}_N^k \pm 1.96 \sqrt{\frac{\hat{P}_N^{kk}}{N}} \quad (\text{B.35})$$

available from standard statistical tables.

B.4 SVC – Geometric data

Geometric data for the crank and piston movement are given in the following table.

Property	Abbrev.	Value	Unit
Bore	B	68	[mm]
Stroke	S	88	[mm]
Crank radius	$a = \frac{S}{2}$	44	[mm]
Connecting rod	l	158	[mm]
No. of cylinders		5	[-]
Displacement volume	V_d	1598	[cm ³]

B.5 Standard volume function: Effect of pin-off

The pin-off for an engine has an effect on the appearance of the displaced cylinder volume (3.4), the position of TDC and BDC (3.5), and the piston stroke (3.6) as shown in section 3.2. The intention is to investigate what effect the pin-off has for a specific engine, namely the SVC engine where the pin-off

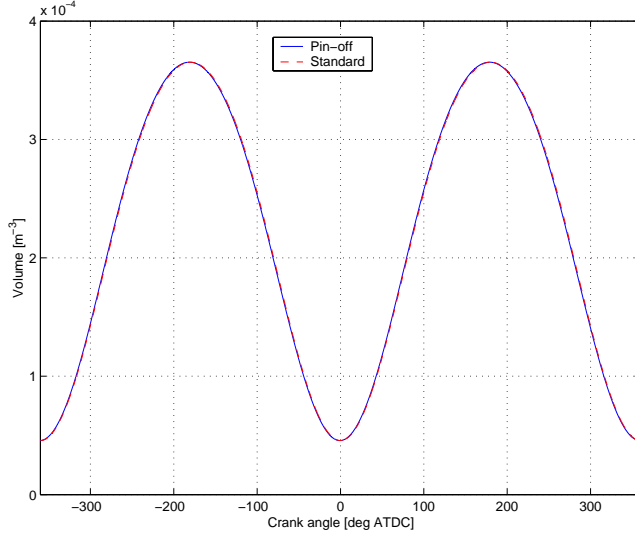


Figure B.1: Cylinder volume with (B.36) and without (B.37) pin-off.

is 2.2 mm. The geometrical data for the SVC engine is given in section B.4. The instantaneous displacement volume function (3.4) is restated here:

$$V_{id}(\theta, x_{off}) = \frac{\pi B^2}{4} \left(\sqrt{(l+a)^2 - x_{off}^2} - a \cos \theta - \sqrt{l^2 - (x_{off} + a \sin \theta)^2} \right) \quad (\text{B.36})$$

Without the pin-off, equation (B.36) can be rewritten as

$$V_{id}^{std}(\theta) = \frac{\pi B^2 a}{4} \left(\frac{l}{a} + 1 - \cos \theta - \sqrt{\left(\frac{l}{a}\right)^2 - \sin^2 \theta} \right) \quad (\text{B.37})$$

referred to as the standard instantaneous displacement volume function. In figure B.1 the cylinder volumes with and without pin-off are plotted. There is no spotable difference between the two volume traces, but according to the lower plot in figure B.2, the relative error can be as large as 1.6 %, which is not negligible. The upper plot shows the absolute error.

The relative error for the piston stroke is approximately 0.01 %, so therefore the pin-off has a small and negligible effect on the total displaced volume for the SVC engine. For the SVC engine, the crank positions for TDC and BDC are -0.62 and 181.11 CAD respectively when considering the pin-off. Not considering the pin-off will therefore result in a false positioning of TDC, i.e. the difference in crank angle position of TDC due to pin-off could be interpreted as a constant crank angle offset θ_0 , as in (3.2). Doing so, the relative difference for the volume

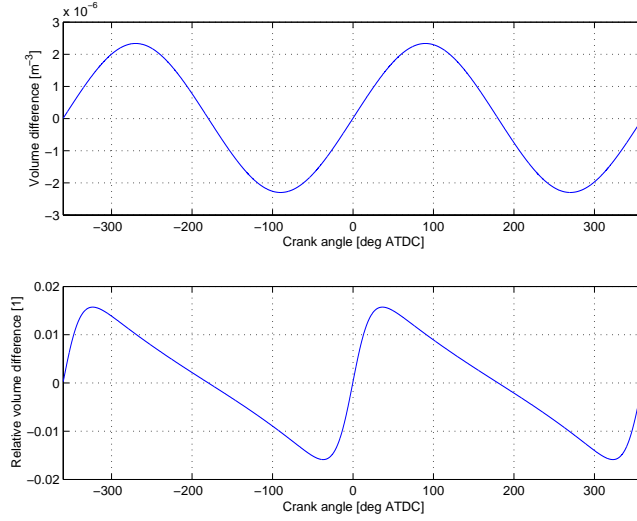


Figure B.2: *Upper*: Absolute error for cylinder volume with and without pin-off corresponding to figure B.1. *Lower*: Corresponding relative error.

functions becomes less than 0.3 %, according to figure B.3, i.e. a factor five in enhancement. Not accounting for pin-off therefore contributes to the problem of TDC determination.

B.6 Cylinder volume for SVC

The principle of the SVC (Saab Variable Compression) engine is shown in figure 5.1. By tilting the mono-head at an angle $v \in [0, 4^\circ]$, the compression ratio can be continuously varied between 14 and 8. The geometric data for the SVC engine are given in appendix B.4. The cylinder volume sweep for the SVC is different in appearance compared to the instantaneous standard volume function (B.37), since the geometry of the crank in relation to the cylinder changes when the cylinder head is tilted. If the cylinder is tilted at an angle v relative to an ex-center (the center of the tilting), this results in a tilting of v_2 for the piston trace relative to the upright piston trace corresponding to $v = 0$. The relation between v_2 and v are given by

$$v_2 = \arctan \left(\frac{b(1 - \cos v) + d \sin v}{d \cos v + b \sin v + c} \right) \quad (\text{B.38})$$

for $v_2 \in] -\pi/2, \pi/2[$. A schematic of the geometry is given in figure B.4. The effective height in the y-direction (d) is given by $d = \sqrt{(l+a)^2 - x_{off}^2} + y_{off} - c$. A new coordinate system (\hat{x}, \hat{y}) is defined at an angle v_2 to the fix coordinate

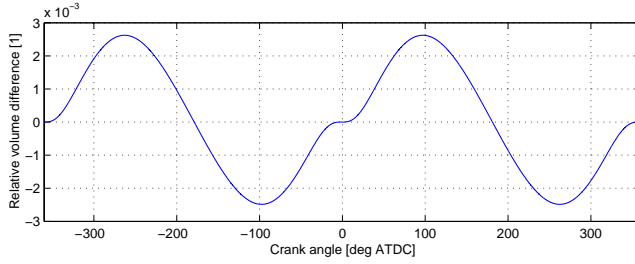


Figure B.3: Relative error for cylinder volume with and without pin-off, when correcting for crank angle offset due to pin-off. This figure should be compared to the lower plot of figure B.2, where the crank angle offset has not been accounted for.

system (x, y) . Consequently the pin-off is transformed into the new coordinate system and the crank angle is redefined as

$$\acute{\theta} = \theta + v_2 \quad (\text{B.39})$$

The new pin-off is $\acute{x}_{off} = x_{off} \cos v_2 + y_{off} \sin v_2$. These relations are put into (B.36), and results in a different volume sweep than with the standard volume function. According to figure B.5 the difference in volume traces is hardly spotable even for $v = 4^\circ$, but according to the lower plot in figure B.6, the relative error can be as large as 6.9 %, which is not negligible.

B.7 Complementary figures for simulation results

For convenience, magnifications of the results for simulated motored cycles given in figure 5.3, for the two extremes $r_c = 8$ and $r_c = 13$ are given in figures B.7 and B.8 respectively. For the simulated firing cycles, the corresponding plots are given in figures B.9 and B.10 respectively.

B.8 Complementary figures for experimental results

For convenience, magnifications of of the results for experimental motored cycles given in figure 5.16 for the two extremes $r_c = 8$ and $r_c = 13$ are given in figures B.11 and B.12 respectively. For firing cycles, the corresponding plots are given in figures B.13 and B.14 respectively.

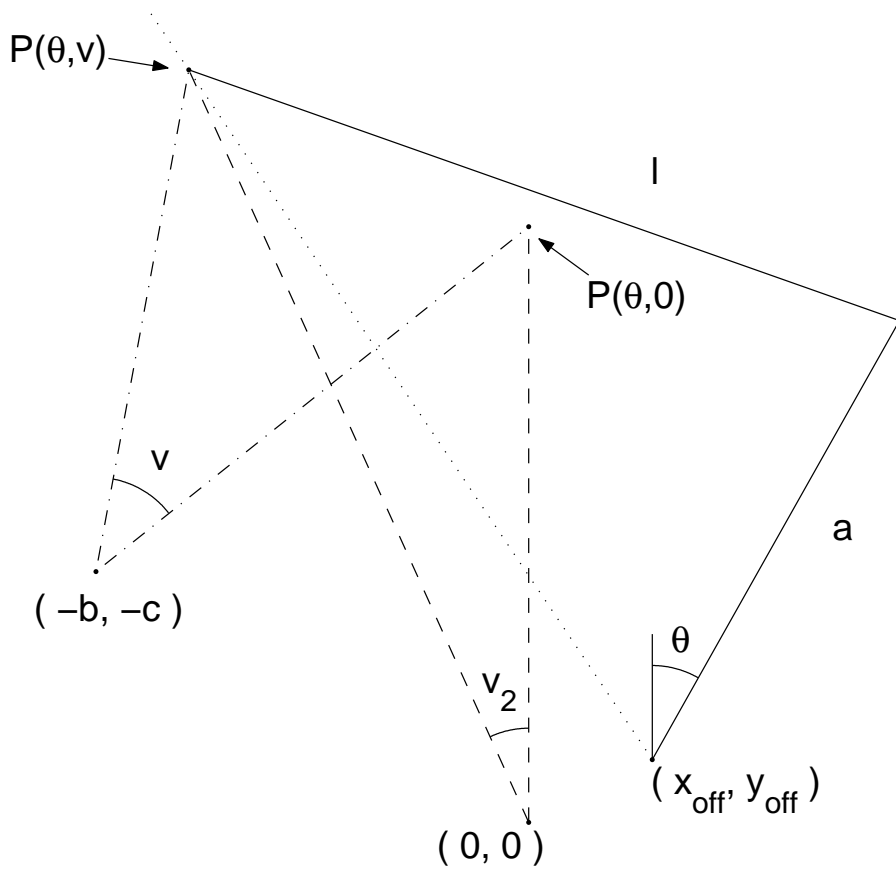


Figure B.4: Schematic of SVC engine geometry. The position of the piston at tilt angle v and crank angle θ is given by $P(\theta, v)$, and the piston follows the dotted line. Note that the schematic is not made to scale.

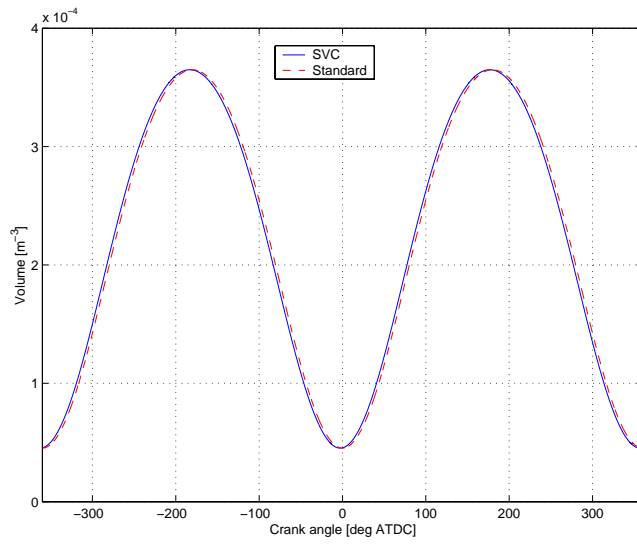


Figure B.5: Cylinder volume for SVC engine and standard volume when the cylinder is tilted $v = 4^\circ$.

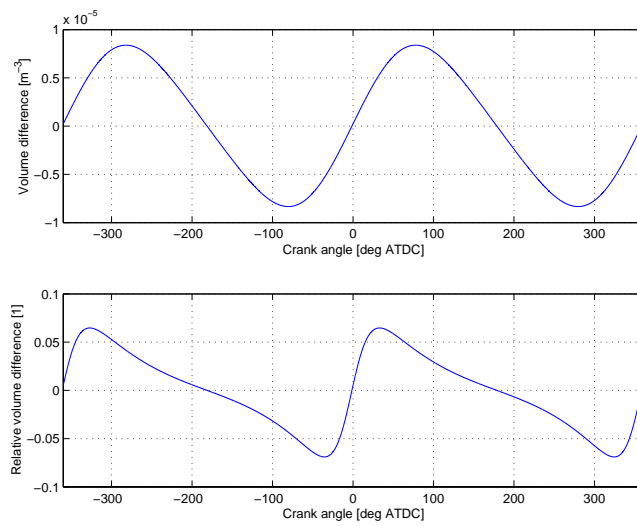


Figure B.6: *Upper*: Absolute error for SVC and standard cylinder volume corresponding to figure B.5. *Lower*: Corresponding relative error.

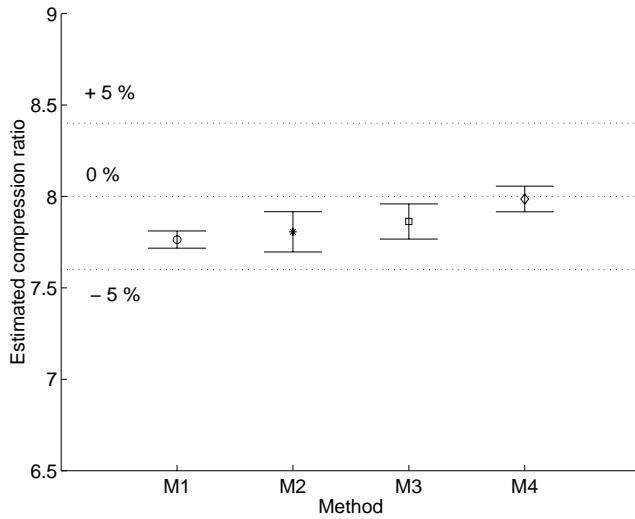


Figure B.7: Mean estimate and 95 % confidence interval for methods 1 to 4 for simulated motored cycles at $r_c = 8$. Shown is also the ± 5 % relative error.

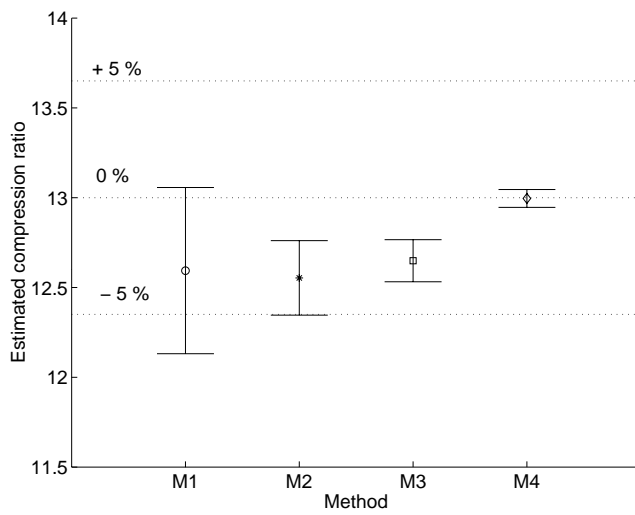


Figure B.8: Mean estimate and 95 % confidence interval for methods 1 to 4 for simulated motored cycles at $r_c = 13$. Shown is also the ± 5 % relative error.

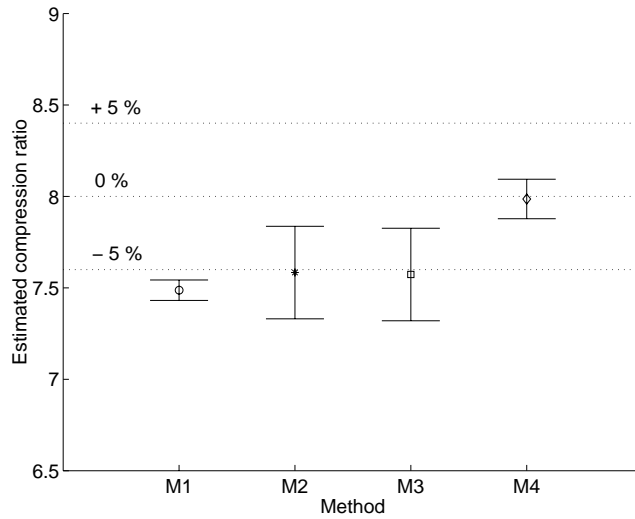


Figure B.9: Mean estimate and 95 % confidence interval for methods 1 to 4 for simulated firing cycles at $r_c = 8$. Shown is also the ± 5 % relative error.

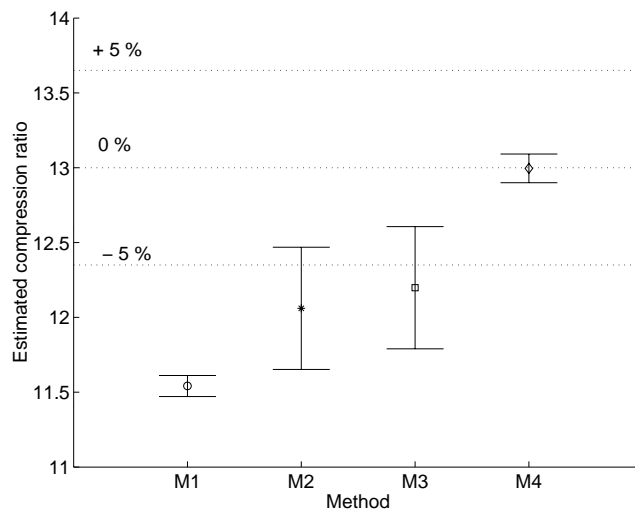


Figure B.10: Mean estimate and 95 % confidence interval for methods 1 to 4 for simulated firing cycles at $r_c = 13$. Shown is also the ± 5 % relative error.

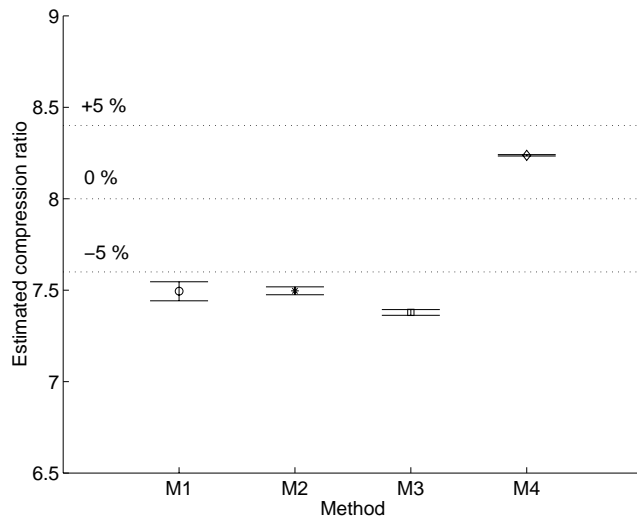


Figure B.11: Mean estimate and 95 % confidence interval for methods 1 to 4 for experimental motored cycles at $r_c = 8$. Shown is also the ± 5 % relative error.

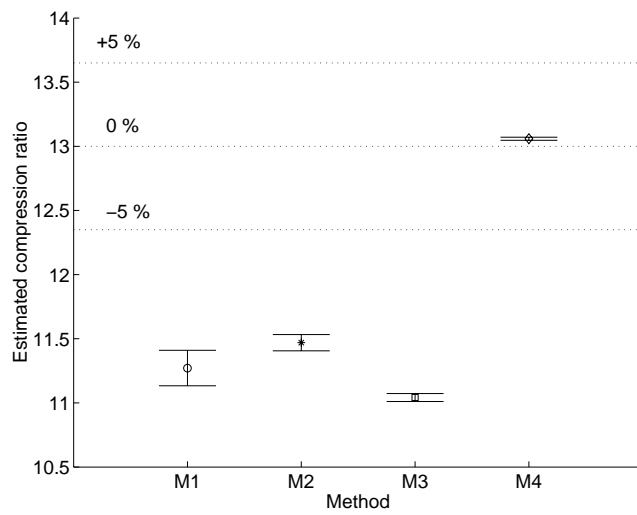


Figure B.12: Mean estimate and 95 % confidence interval for methods 1 to 4 for experimental motored cycles at $r_c = 13$. Shown is also the ± 5 % relative error.

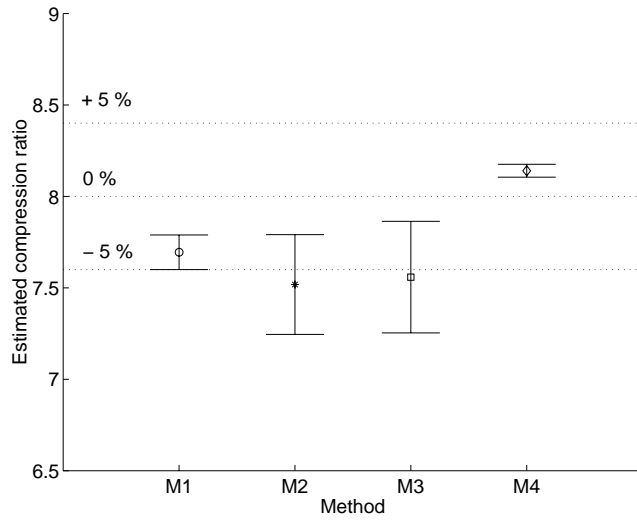


Figure B.13: Mean estimate and 95 % confidence interval for methods 1 to 4 for experimental firing cycles at $r_c = 8$. Shown is also the ± 5 % relative error.

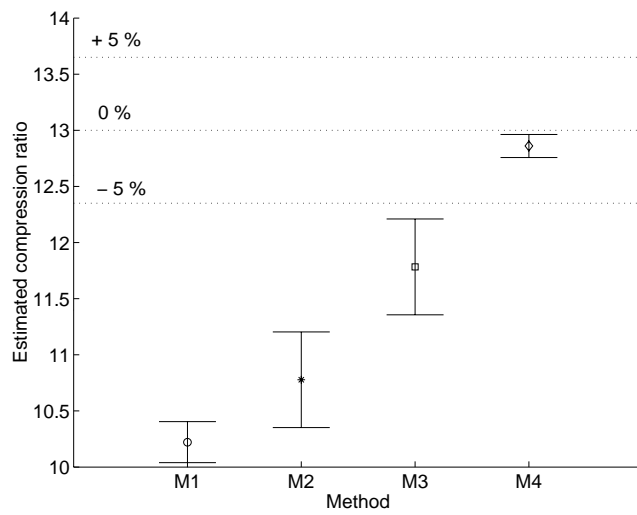


Figure B.14: Mean estimate and 95 % confidence interval for methods 1 to 4 for experimental firing cycles at $r_c = 13$. Shown is also the ± 5 % relative error.

 NOTATION

C.1 Nomenclature

C.1.1 Heat transfer

ρ	gas density	$[kg/m^3]$
v	characteristic velocity	$[m / s]$
L	characteristic length	$[m]$
μ	gas dynamic viscosity	$[kg / (ms)]$
h_c	convection heat transfer coefficient	$[W / (m^2 K)]$
k	gas thermal conductivity	$[W/(m K)]$
p	cylinder pressure for firing cycle	$[Pa]$
p_0	cylinder pressure for motored cycle	$[Pa]$
T	mean gas temperature	$[K]$
T_0	mean gas temperature for motored cycle	$[K]$
T_w	wall temperature	$[K]$
u_p	mean piston speed	$[m/s]$
V_s	swept/displaced volume	$[m^3]$
C_1	constant	$[-]$
C_2	constant	$[m/(s K)]$
$(p_{ref}, V_{ref}, T_{ref})$	evaluated at any reference condition <i>ref</i>	

C.1.2 Engine geometry

V	instantaneous cylinder volume	[m^3]
V_c	clearance volume	[m^3]
V_d	displacement volume	[m^3]
V_{id}	instantaneous displacement volume	[m^3]
r_c	compression ratio index	[-]
V_{cr}	aggregate crevice volume	[m^3]
A	instantaneous surface area	[m^2]
A_{ch}	cylinder head surface area	[m^2]
A_{pc}	piston crown surface area	[m^2]
A_{lat}	instantaneous lateral surface area	[m^2]
θ	crank angle	[rad]
B	cylinder bore	[m]
a	crank radius	[m]
l	connecting rod length	[m]
S	piston stroke	[m]
x_{off}	pin-off	[m]

C.1.3 Engine cycle

p	cylinder pressure	[Pa]
p_m	measured cylinder pressure	[Pa]
Δp	pressure bias	[Pa]
K_p	pressure measurement gain	[-]
p_{man}	intake manifold pressure	[Pa]
T_{man}	intake manifold temperature	[K]
p_{exh}	exhaust manifold pressure	[Pa]
N	engine speed	[rpm]
θ	crank angle	[rad]
θ_{ig}	ignition angle	[rad]
θ_{ppp}	peak pressure position	[rad]

C.1.4 Thermodynamics and combustion

λ	(gravimetric) air-fuel ratio	[-]
$\frac{A}{F_s}$	stoichiometric air-fuel ratio	[-]
$\phi = \lambda^{-1}$	(gravimetric) fuel-air ratio	[-]
x_b	mass fraction burned	[-]
$\Delta\theta$	total combustion duration	[rad]
a	Vibe parameter	[-]
m	Vibe parameter	[-]
θ_d	flame development angle	[rad]
θ_b	rapid burn angle	[rad]
Q_{in}	released energy from combustion	[J]
m_f	fuel mass	[kg]
m_{af}	air-fuel mass	[kg]
m_c	total mass of charge	[kg]
m_b	burned charge mass	[kg]
m_r	residual gas mass	[kg]
x_r	residual gas fraction $x_r = m_r/m_c$	[-]
V_r	residual gas volume	[m ³]
T_r	residual gas temperature	[K]
q_{HV}	specific heating value of fuel	$\frac{J}{kg}$
R	specific gas constant	$\frac{J}{kgK}$
c_v	mass specific heat at constant volume	$\frac{J}{kgK}$
c_p	mass specific heat at constant pressure	$\frac{J}{kgK}$
γ	specific heat ratio	[-]
γ_u	γ for unburned mixture	[-]
γ_b	γ for burned mixture	[-]
γ_{300}	Constant value in linear model of γ (2.27)	[-]
b	Slope in linear model of γ (2.27)	[1/K]
n	polytropic exponent	[-]
T_u	temperature in unburned zone	[K]
T_b	temperature in burned zone	[K]
U	internal energy	[J]
Q	transported heat	[J]
Q_{ch}	chemical energy released as heat	[J]
Q_{ht}	heat transfer to the cylinder walls	[J]
W	mechanical work	[J=Nm]
dm_i	mass flow into zone i	$\frac{kg}{s}$
dm_{cr}	mass flow into crevice region	$\frac{kg}{s}$
h_i	mass specific enthalpy	$\frac{J}{kg}$

C.1.5 Parameter estimation

x	vector used to parameterize model
x^k	parameter k
\hat{x}_N	parameter estimate
\hat{x}_N^k	estimate of parameter k
\hat{x}^*	parameter estimate at optimum
x^{init}	initial values of parameters
x^s	scaled parameters $x^s = Dx$
$x^\#$	nominal value of parameters
$x^{\#,s}$	scaled nominal value of parameters
P	covariance matrix
\hat{P}_N	estimate of covariance at \hat{x}_N
λ_0	noise variance
$\hat{\lambda}_N$	estimated noise variance
H_N	approximative Hessian in (B.25)
Z^N	data set $[y(1), u(1), y(2), u(2), \dots, y(N), u(N)]$
$\mathcal{M}(x)$	model for x
$y(t)$	measured output
$\hat{y}(t x)$	predicted model output
ε	prediction error $y(t) - \hat{y}(t x)$
V_N	loss (criterion) function
ψ	Jacobian vector, defined in (B.22)
$D_{\mathcal{M}(x)}$	parameter domain for $\mathcal{M}(x)$
$\partial D_{\mathcal{M}(x)}$	boundary of $D_{\mathcal{M}(x)}$
d^k	descent direction for iteration k
μ	step size for optimization algorithm
ν	Regularization parameter for Levenberg-Marquardt procedure

C.1.6 Statistics

α	confidence level
σ	standard deviation

C.2 Abbreviations

AFR	Air-Fuel Ratio
ATDC	After TDC
CAD	Crank Angle Degree
CHEPP	CHemical Equilibrium Program Package [Eriksson, 2004]
CI	Compression Ignited
EVO	Exhaust Valve Opening
FAR	Fuel-Air Ratio
FPE	Final Prediction Error
GDI	Gasoline Direct Injected
IVC	Inlet Valve Closing
MRE	Maximum Relative Error
NRMSE	Normalized Root Mean Square Error
RCI	Relative (95 %) Confidence Interval
RE	Relative estimation Error
RMEE	Relative Mean Estimation Error
RMSE	Root Mean Square Error
SI	Spark Ignited
SOC	Start Of Combustion
SVC	Saab Variable Compression
SVD	Singular Value Decomposition
TDC	Top Dead Center, engine crank position at 0 CAD
TWC	Three-Way Catalyst